

**2. GLOBAL CLIMATE**—R. J. H. Dunn, D. M. Stanitski, N. Gobron, and K. M. Willett, Eds.

**a. Overview**—R. J. H. Dunn, D. M. Stanitski, N. Gobron, and K. M. Willett

The global land and ocean surface temperature was remarkably high in 2017. Depending on the dataset considered, the past year ranked as the second or third highest since records began in the mid-to-late 1800s at 0.38°–0.48°C above the 1981–2010 average. Notably, as ENSO conditions were neutral throughout much of 2017, it was the warmest year not influenced by El Niño in the instrumental record, as well as being warmer than any year before 2015.

Unsurprisingly, lake surface temperatures, frequencies of land surface temperature extremes, and tropospheric temperatures also had high, but not record-breaking, global anomalies in 2017. Many other essential climate variables (ECVs; Bojinski et al. 2014) and other measures of the climate system responded to the predominantly above-average temperatures (see also Plate 1.1). Exceptionally high temperatures were observed in the permafrost across the American and European Arctic, with record values observed in large parts of Alaska and northwestern Canada. Preliminary data indicate that glaciers across the world continued to lose mass for the 38th consecutive year on record; the declines are remarkably consistent from region to region. Cumulatively since 1980, this loss is the equivalent of slicing 22 meters off the top of the average glacier.

The continued warmth resulted in a humid year over both land and oceans in terms of specific humidity, but more arid in terms of relative humidity over land. Total column water vapor corroborated the surface specific humidity record, dropping slightly compared to the previous year over both land and ocean, but still remaining above average in most locations. A similar drop from 2016 was observed over the land surface area affected by drought. Global land evaporation was much lower than 2016 and below the long-term average for the year. However, precipitation over global land areas was above the long-term average (by 15–80 mm depending on the dataset used).

This year we include a sidebar (2.1) on precipitation extremes. Extreme precipitation is multifaceted, depending on the timescales over which it is assessed and the average conditions experienced by a given region. A particular focus is on Hurricane Harvey, where 5-day total rainfall amounts broke previous station records in some locations in Texas by over a factor of three.

Anomalously high upper-level divergence along with strong tropical easterly wave disturbances may have contributed to the high levels of storm activity during the Atlantic hurricane season. More generally, upper-air winds from radiosonde measurements continued to show no strong trend, with reanalyses indicating a slight increase in average wind speed (see Dee et al. 2011b about the use of reanalyses for climate monitoring). Surface winds over land continued a slow increase from the multidecadal decrease in globally averaged wind speeds observed since the ~1960s, most clearly seen in central and eastern Asia. Over the oceans, there is disagreement between satellite and reanalysis estimates as to whether wind speeds were above or below average.

The emissions and atmospheric abundance of most ozone-depleting substances continued to decline due to the positive effects of the Montreal Protocol and its Amendments; however, the atmospheric abundance of CFC-11 declined more slowly than expected from mid-2015 to mid-2017, potentially leading to a delay in the recovery of stratospheric ozone.

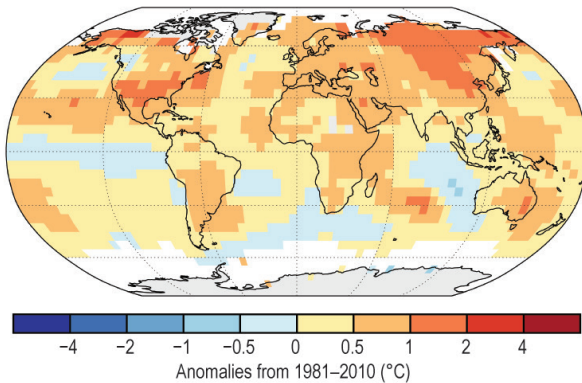
Annual mean total stratospheric ozone levels in 2017 were above average over almost the entire Southern Hemisphere, with Antarctic values more than 10 Dobson units above the 1998–2008 average. This is due to a weakened polar vortex when the quasi-biennial oscillation (QBO) was in the east phase in late 2017, an enhanced Brewer–Dobson circulation transporting ozone into the middle to high latitudes, and the small size and depth of the ozone hole. The long-term upward trend of hemispheric and global average tropospheric ozone continued into 2017.

There were lower concentrations of aerosols in 2017 over highly populated areas in Europe, North America, and China. Trends of total aerosol optical depth (AOD) since 2003 have been negative over Amazonia, the eastern U.S., southern Europe, northern Africa, China, and Japan, possibly from declining deforestation and anthropogenic aerosol emissions as well as reduced dust episodes in desert regions; but trends were positive over the Indian subcontinent.

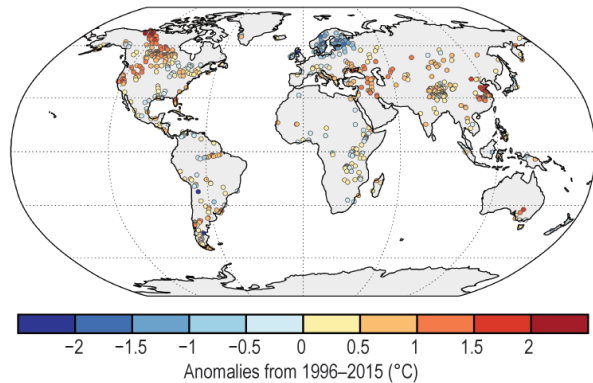
Near-record high stratospheric water vapor anomalies occurred by the middle of 2017 after a record low in December 2016, as confirmed by both the *Aura* Microwave Limb Sounder satellite measurement and balloon-borne frost point hygrometer soundings. This was possibly caused by tropical upwelling linked to the QBO.

A sidebar (2.2) describes the first Tropospheric Ozone Assessment Report (TOAR), completed in October 2017, highlighting a wide range of tropospheric ozone metrics produced using data from thousands

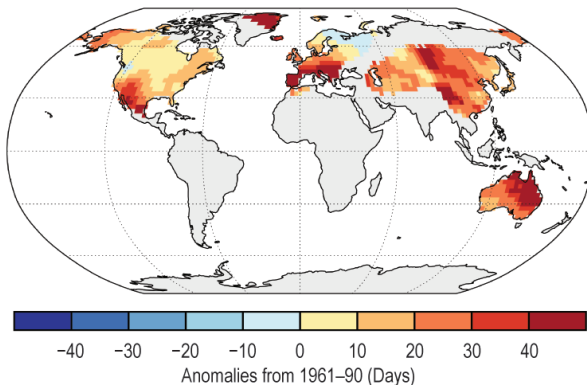
(a) Surface Temperature



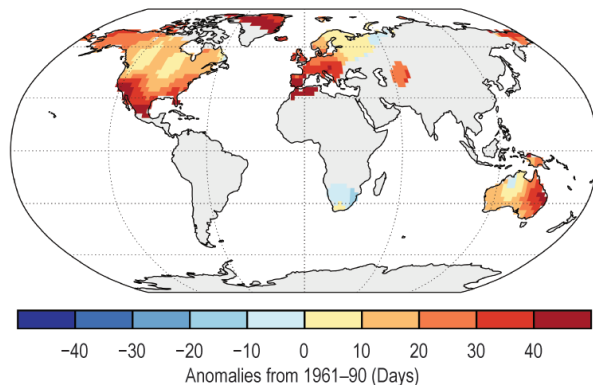
(b) Lake Temperatures



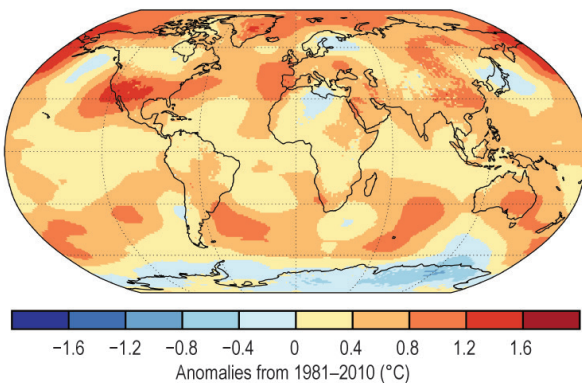
(c) Warm Days (TX90p)



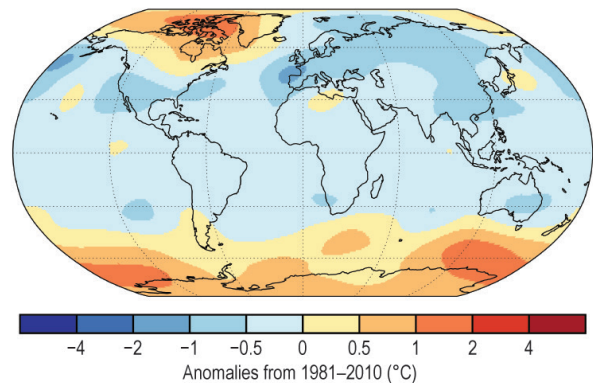
(d) Warm Nights (TN90p)



(e) Lower Tropospheric Temperature



(f) Lower Stratospheric Temperature



(g) Soil Moisture

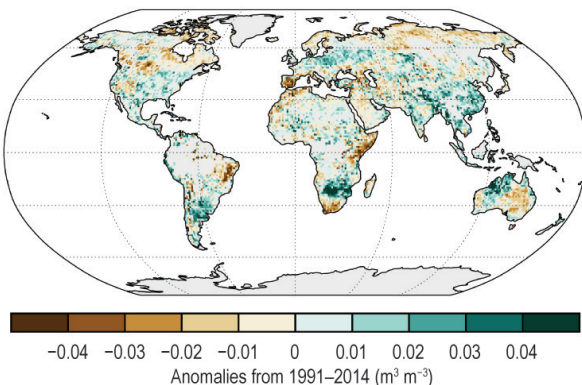
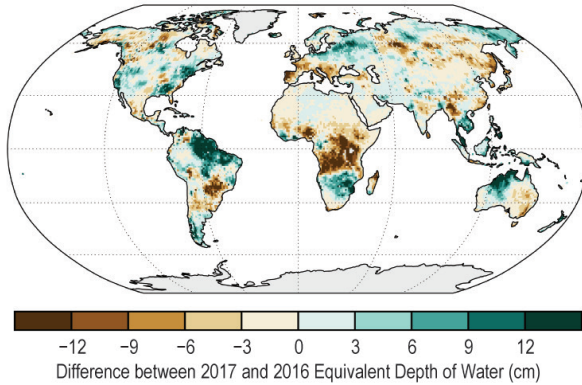


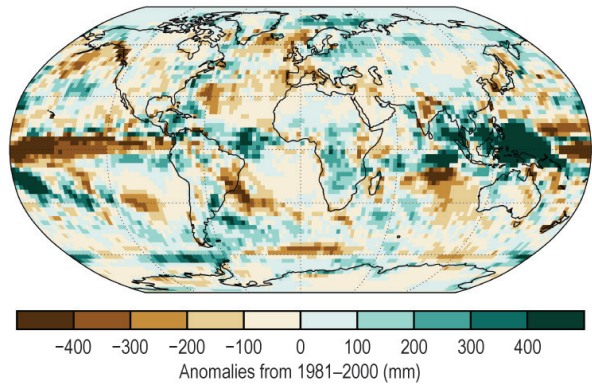
**PLATE 2.1.** (a) NOAA/NCEI surface temperature (NOAAGlobalTemp); (b) Satellite-derived lake surface water temperature; (c) GHCNDEX warm day threshold exceedance (TX90p); (d) GHCNDEX warm night threshold exceedance (TN90p); (e) ERA-Interim lower tropospheric temperature grid anomalies; (f) ERA-Interim gridpoint lower stratosphere temperature anomalies; (g) ESA CCI average surface soil moisture anomalies;



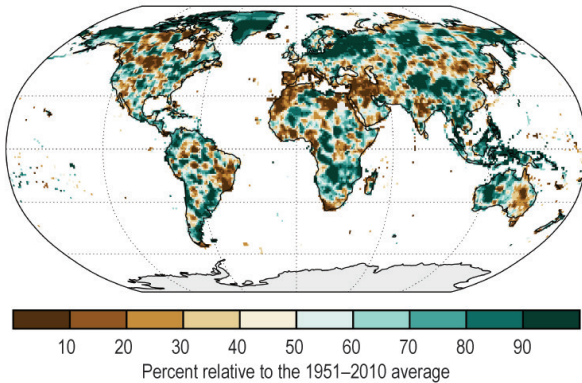
(h) Terrestrial Water Storage



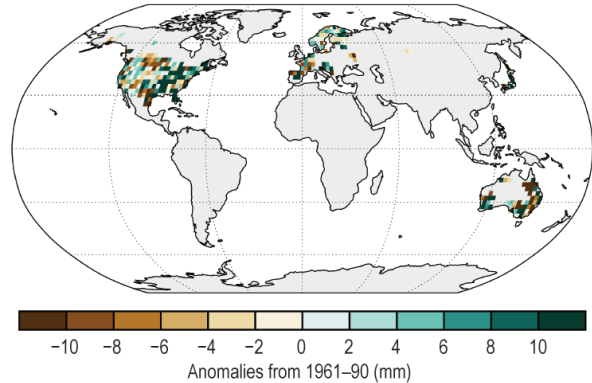
(i) Precipitation



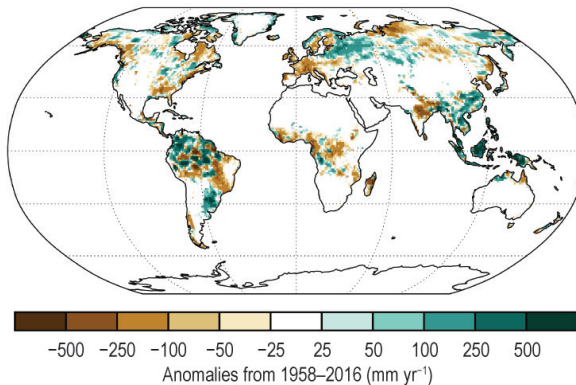
(j) Percentile of the Annual Precipitation Total



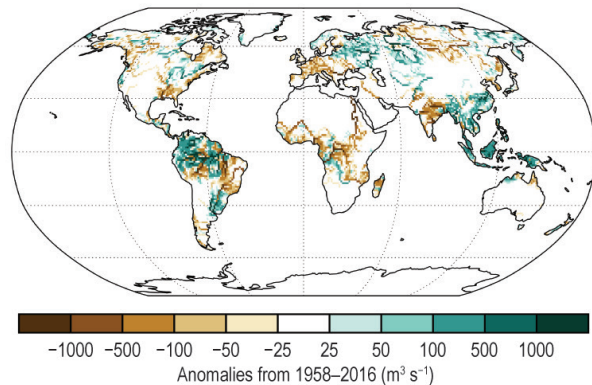
(k) Maximum 1 Day Precipitation Amount (Rx1day)



(l) Runoff



(m) River Discharge



(n) Surface Specific Humidity

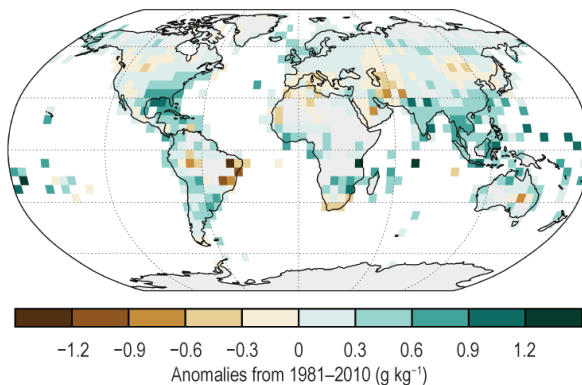
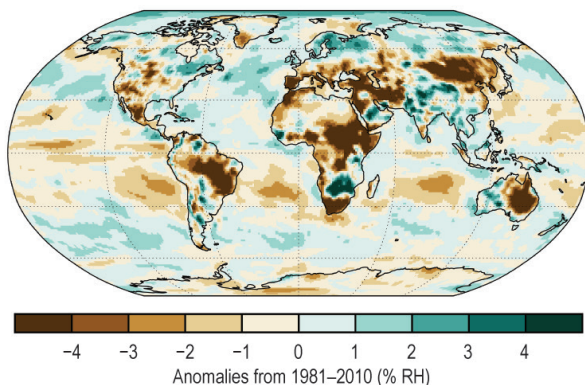
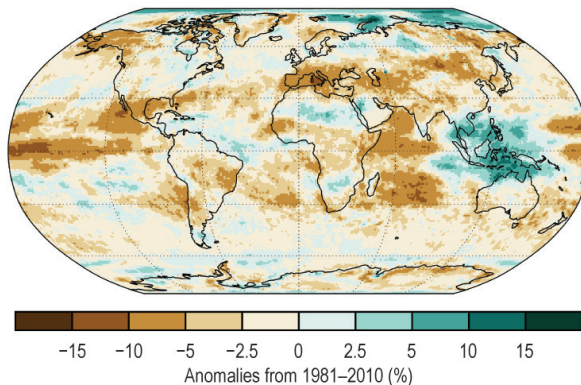


**PLATE 2.1. (CONT.) (h) GRACE difference in annual mean terrestrial water storage between 2016 and 2017; (i) GPCP v2.3 map of annual mean precipitation anomalies; (j) Percentile of annual precipitation total for 2017 GPCC First Guess Daily; (k) GHCNDEX 2017 anomalies for maximum 1 day precipitation total (Rx1day); (l) JRA-55 global distribution of runoff anomaly; (m) JRA-55 global distribution of river discharge anomaly; (n) HadISDH annual average anomaly surface specific humidity over land;**

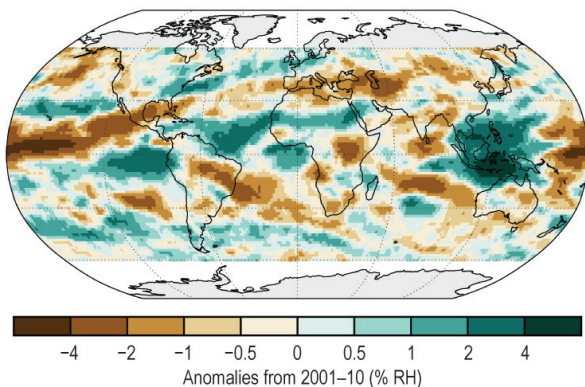
(o) Surface Relative Humidity



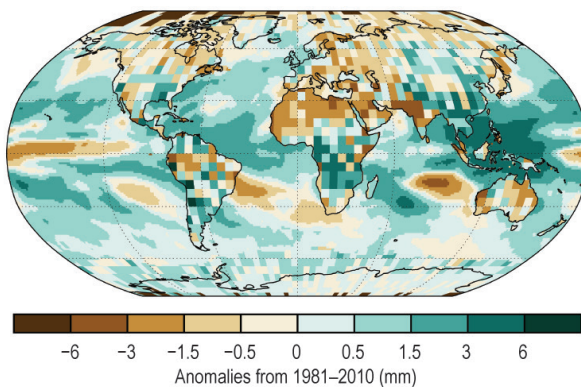
(p) Cloudiness



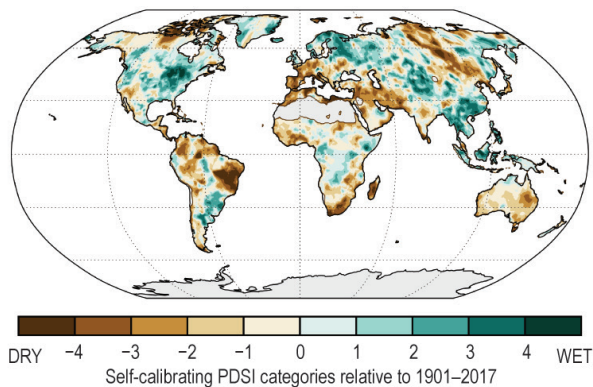
(q) Upper Tropospheric Humidity



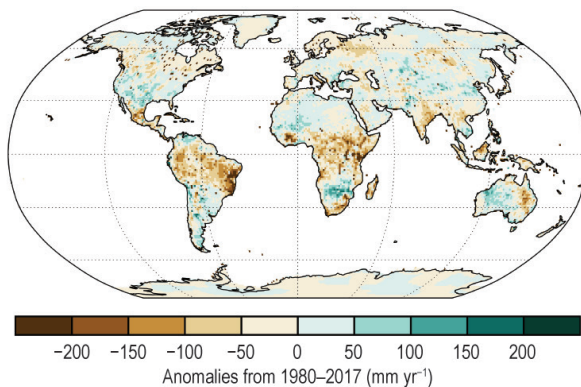
(r) Total Column Water Vapor



(s) Drought



(t) Land Evaporation



(u) Sea Level Pressure

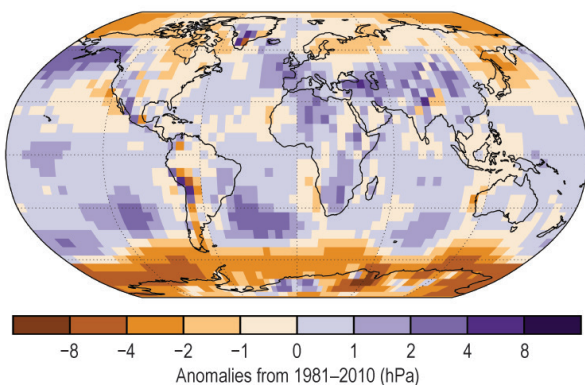
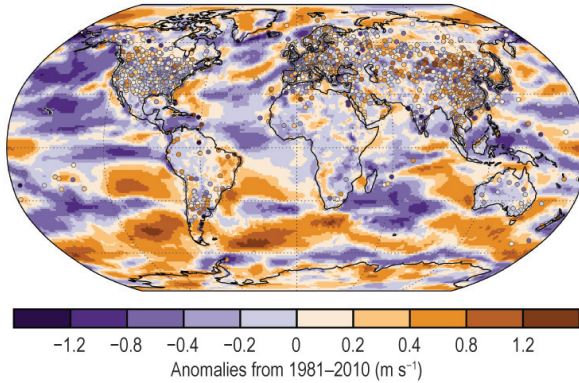


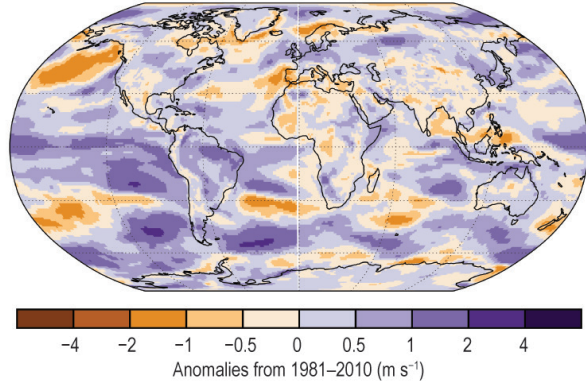
**PLATE 2.1. (CONT.)** (o) ERA-Interim annual average anomaly surface relative humidity; (p) PATMOS-x/ AVHRR global cloudiness anomaly; (q) Microwave UTH anomalies; (r) Total column water vapor anomaly from satellite radiometers (oceans) and COSMIC (land); (s) Mean scPDSI for 2017. Droughts are indicated by negative values (brown), wet episodes by positive values (green); (t) GLEAM land evaporation anomalies; (u) HadSLP2r sea level pressure anomalies;



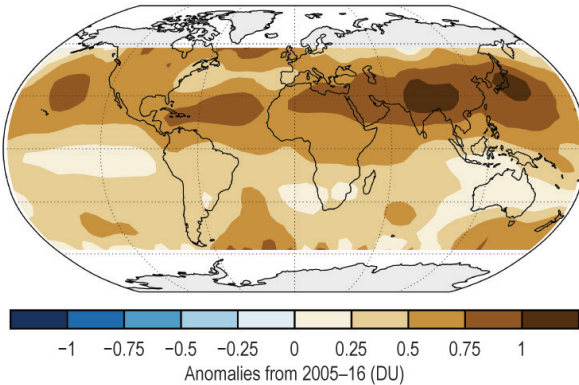
(v) Surface Winds



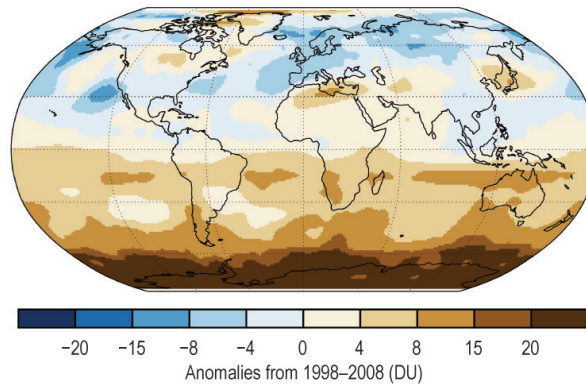
(w) Upper Air (850-hPa) Winds



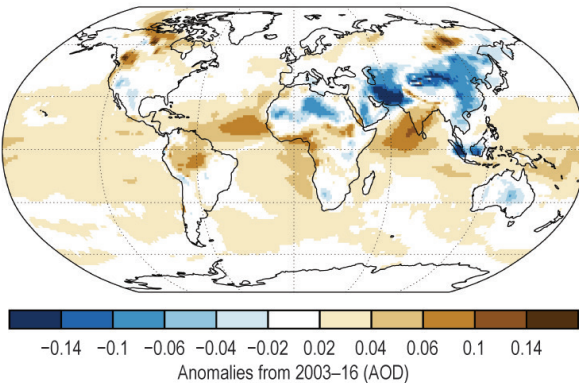
(x) Tropospheric Column Ozone



(y) Stratospheric (Total Column) Ozone



(z) Total Aerosol



(aa) Dust Aerosol

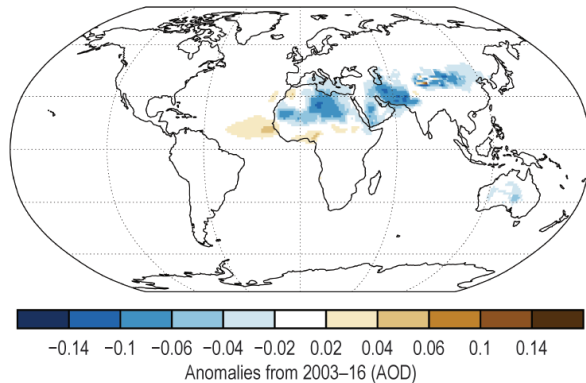
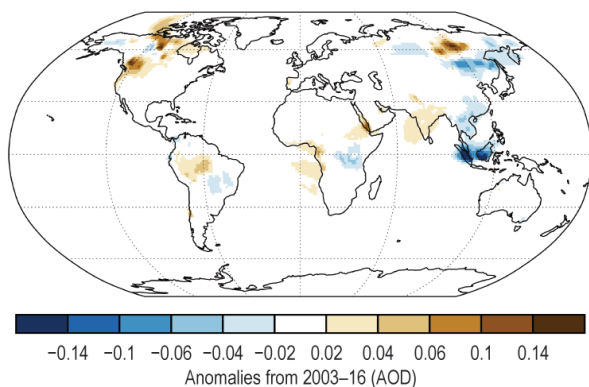


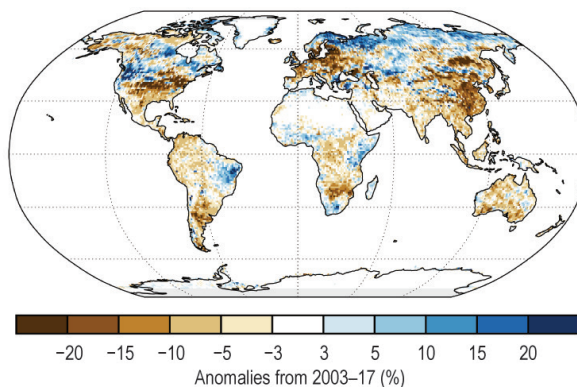
**PLATE 2.1. (CONT.)** (v) Land surface wind speed anomalies (circles: observational HadISD2 and Australian datasets, and worldwide shaded grids: MERRA-2); (w) ERA-Interim upper air winds; (x) Global distribution of OMI/MLS tropospheric column ozone annual mean anomalies (in Dobson Units) for year 2017 relative to the 2005-2016 average field. White areas poleward of 60°N and 60°S were flagged as missing due to lack of sufficient OMI ozone measurements during winter polar night to calculate annual averages; (y) GOME-2 2017 total column ozone anomalies [using GOME, SCIAMACHY, and GOME-2 (GSG) for 1998-2008 climatology]; (z) Anomalies of total AOD at 550 nm; (aa) Anomalies of dust AOD at 550 nm;



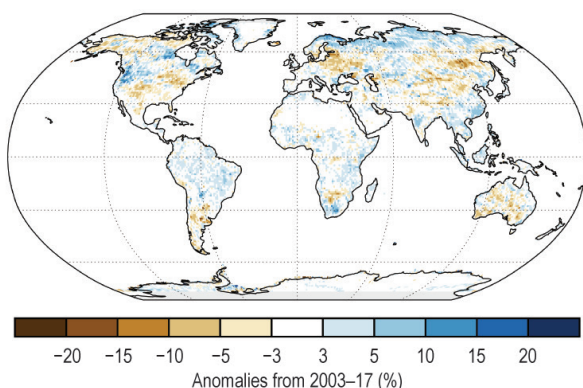
(ab) Biomass Burning Aerosol



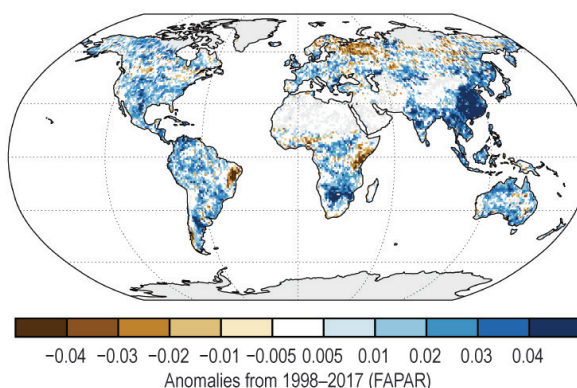
(ac) Land Surface Albedo in the Visible



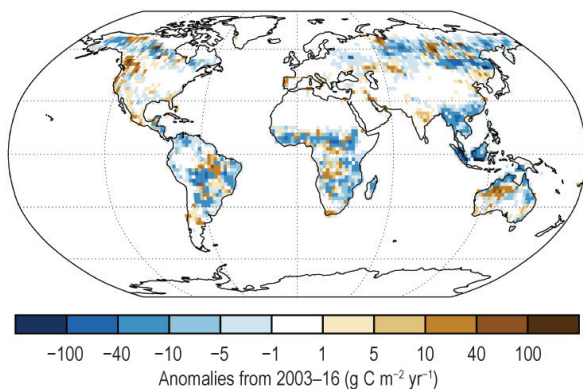
(ad) Land Surface Albedo in the Near-Infrared



(ae) Fraction of Absorbed Photosynthetically Active Radiation



(af) Carbon Emissions from Biomass Burning



(ag) Carbon Monoxide

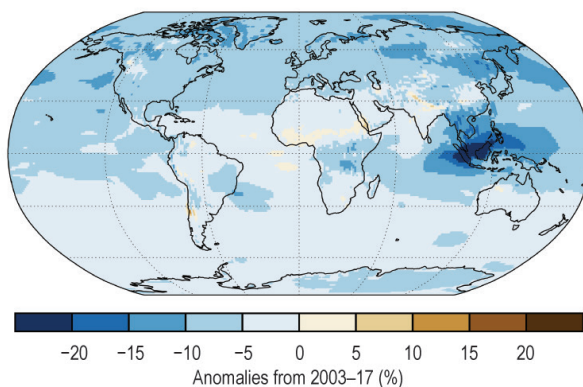


**PLATE 2.1. (CONT.) (ab) Anomalies of biomass burning AOD at 550 nm; (ac) Visible broadband albedo anomalies; (ad) Near-infrared broadband albedo anomalies; (ae) FAPAR anomalies; (af) GFASv1.4 carbonaceous emission from biomass burning; (ag) CAMS total column CO anomalies.**

of global surface sites. The metrics are focused on the impacts of tropospheric ozone on human health, vegetation, and climate, and are based on the TOAR's large database of surface hourly ozone observations.

In 2017, there were no regional biomass burning events that had a global impact on the annual carbon monoxide (CO) regional burden, evidenced by the fact that 2017 had the lowest CO burden since 2003. In Indonesia and central Africa, the CO burden was considerably lower than in previous years due to reduced fire activity. Globally during 2017, the levels of fire activity (as opposed to impacts or losses) were the lowest since at least 2003, 15% below the 2003–16 average. However, stronger activity occurred in North America, Europe, and Siberia, with an unusually long season in Portugal and northwestern Spain, and the worst fires experienced in recent history in British Columbia in terms of burned area.

A sidebar (2.3) focusing on land surface phenology observations in the Northern Hemisphere is also included. In contrast to meteorological and hydrological observations, which give a physical description of the current climate, phenology information shows how the natural environment is responding as the state of the climate changes over time.

A common theme across a number of sections is the lack of available data to adequately monitor the climate and make assessments of change. While naturally an issue for this publication, we believe it is worth highlighting more widely. Some examples from this chapter include surface humidity, where no observational marine product is currently available; terrestrial water storage, where no satellite observations currently exist past June 2017; and subdaily (extreme) precipitation. Furthermore, there are several ECVs where various estimates are not in good agreement with each other or with reanalysis products. Limited

availability of high-quality, high-resolution, and timely datasets is impinging on the ability to monitor the climate in these cases. Improved (open) access to data, continued stable monitoring, and near-real time data releases all help in allowing accurate assessments of current changes.

Time series and anomaly maps for many variables described in this chapter are shown in Plates 1.1 and 2.1 respectively. Many sections refer to online figures that can be found here (<http://doi.org/10.1175/2018BAMSStateoftheClimate.2>).

## b. Temperature

### 1) GLOBAL SURFACE TEMPERATURES—A. Sánchez-Lugo, C. Morice, P. Berrisford, and A. Argüez

The 2017 global surface temperature was the second or third highest annual global temperature since records began in the mid-to-late 1800s at 0.38°–0.48°C above the 1981–2010 average (Table 2.1; Fig. 2.1), according to four independent in situ analyses (NASA-GISS, Hansen et al. 2010; HadCRUT4, Morice et al. 2012; NOAA GlobalTemp, Smith et al. 2008, Huang et al. 2015; JMA, Ishihara 2006). The 2017 value was lower than the record set in 2016 and, depending on the dataset, 2015, both of which were years influenced by a strong El Niño episode. In contrast, ENSO-neutral conditions were present across the tropical Pacific Ocean during much of 2017, transitioning to La Niña in October. Despite this, global temperature anomalies were high throughout the year, resulting in the warmest non-El Niño year on record. Separately, the global land annual temperature ranked as either the second or third highest on record, again, depending on the dataset, and the globally averaged sea surface temperature (SST) was third highest.

**TABLE 2.1. Temperature anomalies (°C) and uncertainties (where available) for 2017 wrt the 1981–2010 base period. Temperature anomalies provided in the table are the central values of a range of possible estimates. Uncertainty ranges are represented in terms of a 95% confidence interval. Note that the land values computed for HadCRUT4 used the CRUTEM.4.6.0.0 dataset (Jones et al. 2012), the ocean values were computed using the HadSST.3.1.1.0 dataset (Kennedy et al. 2011a, 2011b), and the global land and ocean values used the HadCRUT4.6.0.0 dataset.**

Global	NASA-GISS	HadCRUT4	NOAA-Global Temp	JMA	ERA-Int	JRA-55	MERRA-2
Land	+0.73	+0.66 ± 0.13	+0.70 ± 0.15	+0.69	+0.73	+0.70	+0.47
Ocean	+0.35	+0.30 ± 0.07	+0.31 ± 0.16	+0.28	+0.45	+0.38	+0.36
Land and Ocean	+0.48 ± 0.05	+0.38 ± 0.08	+0.41 ± 0.15	+0.38	+0.53	+0.48	+0.39

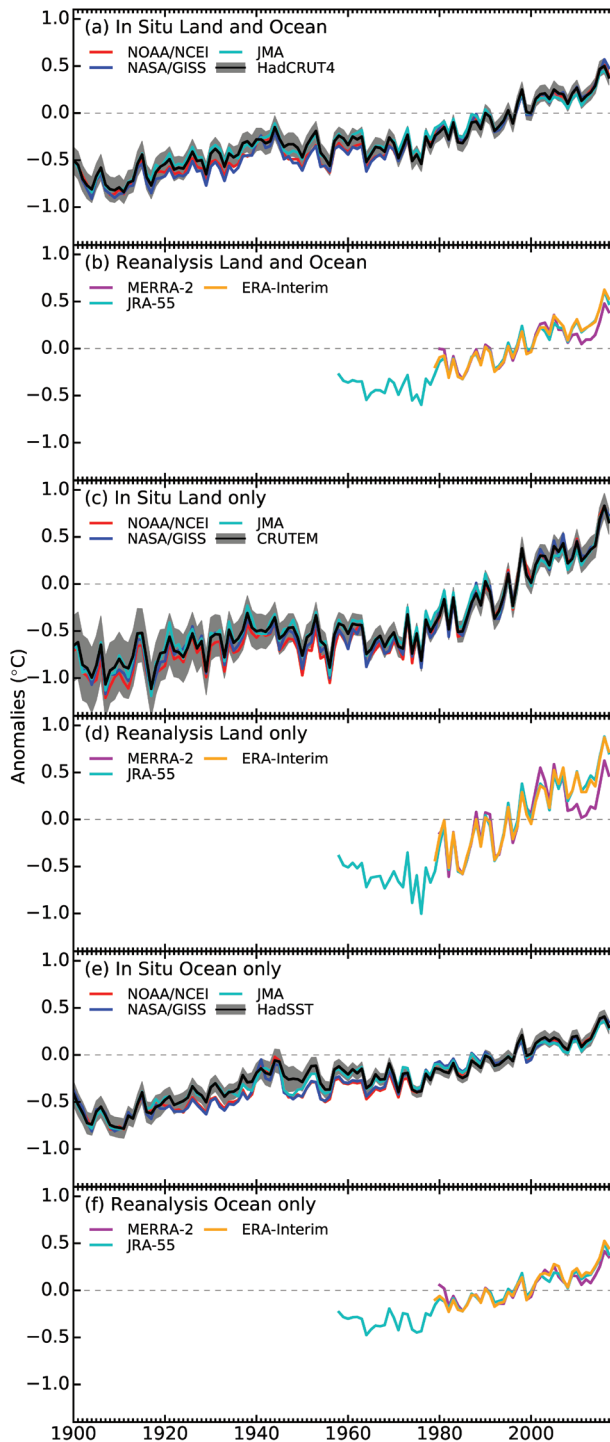


**FIG. 2.1. Global average surface temperature anomalies (°C; 1981–2010 base period).** In situ estimate are shown from NOAA/NCEI (Smith et al. 2008), NASA-GISS (Hansen et al. 2010), HadCRUT4 (Morice et al. 2012), CRUTEM4 (Jones et al. 2012), HadSST3 (Kennedy et al. 2011a,b), JMA (Ishihara 2006). Reanalyses estimates are shown from ERA-Interim (Dee et al. 2011a), MERRA-2 (Bosilovich et al. 2015; Gelaro et al. 2017) and JRA-55 (Ebita et al. 2011; Kobayashi et al. 2015).

The global surface temperature analyses assessed here are derived from air temperatures observed at weather stations over land and SSTs observed from ships and buoys. Differences between analyses are mainly due to how each methodology treats areas with little to no data, such as the polar regions, and how each analysis accounts for changes in measurement methods [for more details see Kennedy et al. (2010); Hansen et al. (2010); Huang et al. (2015); and Sánchez-Lugo et al. (2017)]. The ranges of temperature anomalies provided in this summary are ranges of best estimates for the assessed in situ analyses. These ranges do not include uncertainty information from each in situ analysis, which can be found in Table 2.1.

The ten warmest years on record have all occurred since 1998, with the four warmest years occurring since 2014. Incrementally adding years to the analysis starting from 1988, each year initially ranks among the ten warmest years on record (with the exception of 2011, which ranked among the top twelve years at the time). The median value for the initial ranking since 1988 for a newly ended year is second or third highest, suggesting that the current ranking of 2017 is consistent with recent tendencies.

In addition to the ranking, it is illustrative to distinguish between warmer and colder years relative to the sustained trend (e.g., looking at the residuals from an ordinary least squares regression, Fig. 2.2). The average rate of change of global average surface temperature since 1901 is  $0.7^{\circ}\text{--}0.9^{\circ}\text{C century}^{-1}$ . However, this rate of change has nearly doubled in the period since 1975 ( $1.5^{\circ}\text{--}1.8^{\circ}\text{C century}^{-1}$ ). Relative to the trend, the years 2008 and 2011 (both years influ-

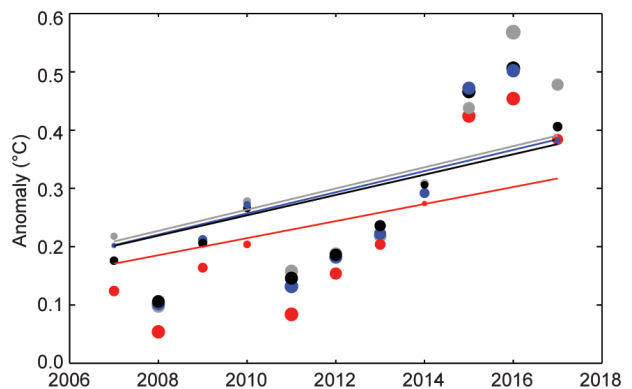


**FIG. 2.2. Annual global temperature anomalies (°C; displayed as dots) from 2007–17.** Lines represent the linear trends over the 1975–2017 period, while the size of the dot represents the trend residuals. The black, gray, red, and blue colors represent the NOAA GlobalTemp, NASA GISS, JMA, and HadCRUT datasets, respectively.



enced by a strong La Niña) were considerably cooler than surrounding years and below the overall trend line, whereas 1998 and 2016 were not only considered the warmest years on record when reported, but their values are considerably above the trend line. The year 2014, on the other hand, was considered to be the warmest year on record at the time, even though its value is near the 1975–2017 trend line. The 2017 anomaly is near the trend line for the HadCRUT4 series (~50th percentile) and above the trend in the other in situ datasets (~60th to 80th percentile). While the value of residuals may shift with the addition of each new year of data, the current data suggest that the 2017 annual global temperature and ranking are consistent with the progression of the upward trend since the mid-1970s.

During 2017, much-warmer-than-average conditions were present across most of the world's land and ocean surfaces, with limited areas (parts of the north, central, and eastern Pacific Ocean, the southern Atlantic Ocean, eastern Indian Ocean, and a small area in western North America) experiencing near- to cooler-than-average conditions (Plate 2.1a).

Global average surface air temperatures are also estimated using reanalyses. Reanalysis produces datasets with uniform temporal and spatial coverage of the whole globe, but can suffer from regional model biases and the effects of changes in the observation network during the analysis period. However, surface temperatures from reanalyses should be consistent with observations in regions of good observational coverage. Here we consider three reanalyses: ERA-Interim (Dee et al. 2011a), JRA-55 (Ebita et al. 2011; Kobayashi et al. 2015), and MERRA-2 (Bosilovich et al. 2015; Gelaro et al. 2017). The ERA-Interim 2-m temperature was adjusted by merging analyses over land with short forecasts over ocean and subtracting 0.1°C from the latter before 2002, in order to account for a change in SST provider, following Simmons et al. (2017) and Simmons and Poli (2014). ERA-Interim provides data from 1979, JRA-55 from 1958, and MERRA-2 from 1980.

According to the reanalyses, the annual global 2-m temperature for 2017 was the second highest since their records began and was between 0.39°C and 0.53°C above average, depending on the reanalysis (Table 2.1). The temperatures for the warmest year, 2016, ranged between 0.47°C and 0.62°C above average.

ERA-Interim and MERRA-2 for 2017 also show warmer-than-average conditions over many regions of the world (Online Figs. S2.1–S2.3), particularly over higher northern latitudes. A few regions were

cooler than average, including Antarctica. The 2017 global ocean temperature is the second highest on record in all three reanalyses, whereas over global land the temperature is the second highest in JRA-55 and ERA-Interim but only the fourth highest in MERRA-2, where temperatures were lower than in 2016, 2005, and 2002.

- 2) LAKE SURFACE TEMPERATURE—R. I. Woolway, L. Carrea, C. J. Merchant, M. T. Dokulil, E. de Eyto, C. L. DeGasperis, J. Korhonen, W. Marszelewski, L. May, A. M. Paterson, A. Rimmer, J. A. Rusak, S. G. Schladow, M. Schmid, S. V. Shimaraeva, E. A. Silow, M. A. Timofeyev, P. Verburg, S. Watanabe, and G. A. Weyhenmeyer

Observed lake surface water temperature anomalies in 2017 are placed in the context of the recent warming observed in global surface air temperature (Section 2b1) by collating long-term in situ lake surface temperature observations from some of the world's best-studied lakes and a satellite-derived global lake surface water temperature dataset. The period 1996–2015, 20 years for which satellite-derived lake temperatures are available, is used as the base period for all lake temperature anomaly calculations. Warm-season averages (i.e., time periods without ice cover: July–September in the Northern Hemisphere above 23.5°N and January–March in the Southern Hemisphere below 23.5°S) are analyzed in line with previous lake surface temperature analyses (Schneider and Hook 2010; O'Reilly et al. 2015; Woolway and Merchant 2017). Temperatures of lakes located within 23.5° of the equator are averaged over the whole year.

Satellite-derived lake surface water temperatures for 688 lakes are used in this analysis to investigate global variations in lake surface water temperature. Satellite-derived surface water temperatures were retrieved during the day using the methods of MacCallum and Merchant (2012) on image pixels filled with water according to both the inland water dataset of Carrea et al. (2015) and a reflectance-based water detection scheme (Xu 2006). The satellite temperatures represent midmorning observations throughout the record (except at the highest latitudes, where observations may be available at other times of day). The observations were generated using data from the ATSR (Along Track Scanning Radiometer) series including ATSR-2 (1995–2003) and the Advanced ATSR (AATSR) (2002–12), extended with *MetOp-A* AVHRR (2007–17). In this study, lake-wide average surface temperatures are used to remove the intralake heterogeneity of surface water temperature responses to climate change (Woolway and Merchant 2018).

In 2017, satellite-derived lake surface temperatures were lower than observed in 2016 by 0.3°C in the 688-lakes average (Fig. 2.3a), though the mean anomaly for 2017 was still +0.4°C above the baseline, continuing the long-term lake surface warming trend identified in previous analyses (e.g., Woolway et al. 2017) and reflecting the observed increase in global surface air temperature (section 2b1). Lake surface water temperatures in 2017 were the second highest since 1995 (the earliest satellite data used), behind only 2016. Eight of the ten warmest years for lake surface waters in the record have occurred since 2007 (1998 and 2001 rank fifth and ninth, respectively).

Lake surface water temperatures in 2017 were not above average in all regions (Figs 2.3b,c; Plate 2.1b). Below-average lake surface temperatures prevailed throughout north and northwestern Europe (Plate 2.1b; Fig. 2.4) in summer, where lake surface temperatures were up to 1°C cooler than the 20-year base period mean. The satellite data and in situ lake

temperature anomalies agree in this respect. For example, in situ measurements of temperature anomaly in Vättern (Sweden) were  $-0.03^{\circ}\text{C}$  (i.e., below the 20-year base period mean) in summer 2017. There is a clear contrast between Scandinavian lake surface temperature anomalies and those in central Europe, with lake temperature anomalies in the latter region up to  $1^{\circ}\text{C}$  higher than average (Plate 2.1b; Fig. 2.4). This is also confirmed by in situ lake temperature anomalies, for example,  $+0.7^{\circ}\text{C}$  in 2017 for Lake Zurich (Switzerland). Above-average lake surface temperature anomalies are also observed from the satellite data in northwest Canada and the western United States, confirmed by in situ data (e.g.,  $+0.8^{\circ}\text{C}$  in Lake Washington). Lakes in the central and eastern U.S. experienced near-normal lake surface temperatures in 2017, with some regions showing below-average

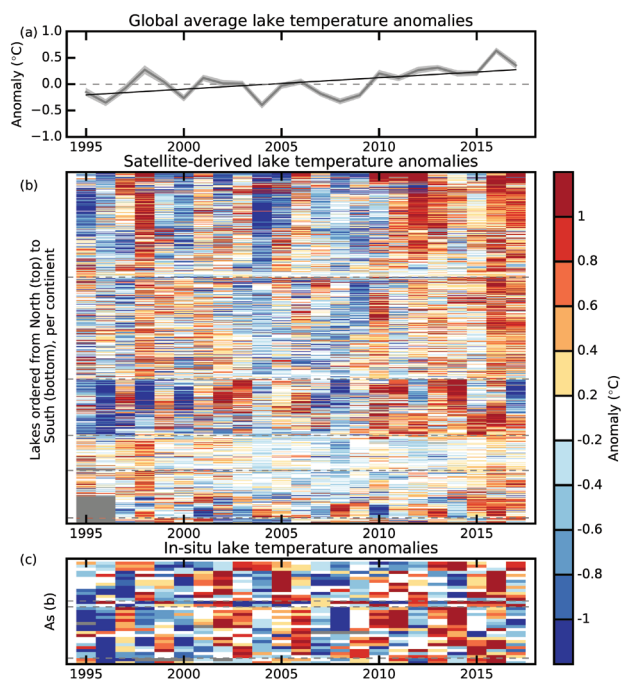


**FIG. 2.3. Annual lake surface water temperature anomalies 1995–2017 ( $^{\circ}\text{C}$ ; relative to 1996–2015). (a) Global average (with 95% confidence intervals) satellite-derived lake surface temperature anomalies; (b) satellite-derived lake surface temperature anomalies for 688 lakes; and (c) in situ lake surface temperature anomalies for 34 globally distributed lakes. Annual lake surface water temperatures anomalies are calculated for the warm season (Jul–Sep in NH; Jan–Mar in SH), except within  $23.5^{\circ}$  of the equator, where the averages are taken over the whole year.**

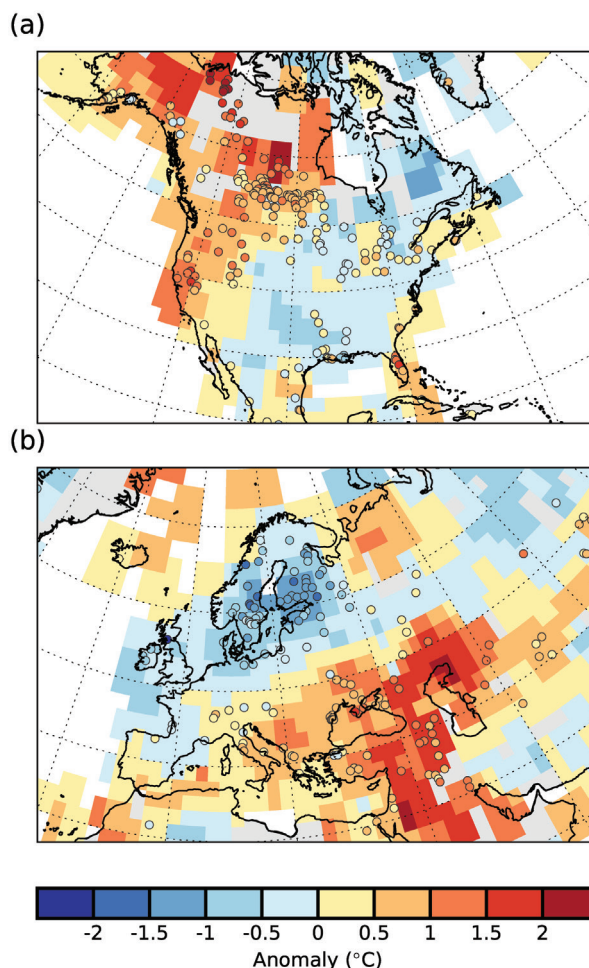


**FIG. 2.4. Comparisons of satellite-derived lake surface water temperature anomalies (colored dots) to air surface temperature anomalies (calculated from the NASA GISS Surface Temperature Analysis) in (a) North America and (b) Europe in 2017. Temperatures anomalies ( $^{\circ}\text{C}$ ; relative to 1996–2015) are calculated for the NH warm season (Jul–Sep).**

lake surface temperatures. These regional differences in lake surface temperature anomalies in 2017 reflect the July–September average surface air temperature anomalies (relative to 1996–2015), calculated from the NASA GISS surface temperature analysis (Fig. 2.4; Hansen et al. 2010; GISTEMP Team 2016). In summary, surface air and lake water temperatures in 2017 were generally coherent.

### 3) LAND SURFACE TEMPERATURE EXTREMES—

S. E. Perkins-Kirkpatrick, M. G. Donat, and R. J. H. Dunn

Changes in temperature extremes are important for climate monitoring due to their sensitivity to relatively small changes in average conditions. Small changes in average temperature can induce much larger changes in the intensity and frequency of corresponding heat extremes. Land surface temperature extremes during 2017 were characterized by overall increased occurrences of warm temperatures and reduced occurrences of cooler temperatures compared to long-term averages. A number of anomalously high temperature events occurred in 2017, in both maximum and minimum daily temperatures. As in previous reports, the GHCNDEX quasi-global gridded dataset (Donat et al. 2013b) is used to monitor global temperature extremes over land. This is quasi-global, as an absence of data over some locations hinders the robust calculation of extremes indices and their trends. A suite of temperature and precipitation extremes indices (Zhang et al. 2011) is first calculated from observed daily station time series in the GHCN-Daily archive (Menne et al. 2012), before interpolating the indices on global grids. Some of the fields of extremes indices have limited spatial coverage, especially across central and eastern Asia, for those derived from minimum temperatures compared to those from maximum temperatures. Therefore, complete coverage derived from the ERA-Interim reanalysis (Dee et al. 2011a) is shown separately in Online Figs. S2.7–S2.9.

Results are presented for a selection of the temperature indices in GHCNDEX: TX90p (frequency of warm days when daily temperatures exceed the 90th percentile of daily maximum temperatures calculated over the 1961–90 base period), TX10p (cool day frequency, daily temperatures below the 10th percentile), TN90p and TN10p (warm and cool night frequency, respectively), and TXx, TXn, TNx, and TNn (extrema of annual maximum and minimum temperatures, respectively; see online supplement for full definitions). Averaged over areas where there are observations, there were fewer warm days (TX90p) and more cool nights (TN10p) in 2017 compared to 2016. However,

such values are still typically well above and below the climatologically defined threshold of 36.5 days per year, respectively (Fig. 2.5).

Over areas where observations exist, the annual occurrence of warm days (TX90p) and nights (TN90p; Plates 2.1c,d) was typically well above the climatological average. In particular, eastern Asia experienced 20 more warm days than the threshold, whereas southern Europe and eastern Australia experienced more than 40 additional warm days. The frequency of warm nights was less than warm days over Australia and southern Europe but was still 10–30 days and 30–40 days more than the threshold, respectively. Conversely, the U.S. and Canada experienced slightly more warm nights than warm days.

Cool days and nights (TX10p, TN10p; Fig. 2.6) were less frequent than the threshold over some regions, with around 20 fewer cool nights over the U.S. and Canada and 30 fewer nights for Europe. For northern regions with available data, annual minima during both daytime and nighttime (TXn, TNn, Online Figs. S2.4c,d) were very high. The respective annual maxima, however, did not always display similar anomalies (TXx, TNx; Online Figs. S2.4a,b).

The frequency of warm daytime temperatures (TX90p; Online Fig. S2.5) varied across the seasons. During boreal winter (DJF 2016/17), warm day occurrences much higher than the threshold occurred over northern Europe and eastern China, Russia, and Australia. However, western Australia and the

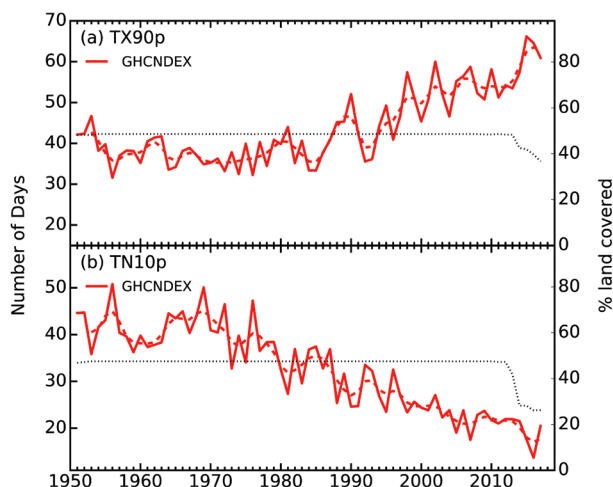


**FIG. 2.5.** Global average time series of the number of (a) warm days (TX90p) and (b) cool nights (TN10p) from GHCNDEX relative to 1961–90. (This reference period is used for consistency with other ETCCDI index products.) By construction, these indices have an average of 36.5 days over the reference period. The dotted black line shows the percent of land area with data. Units: days.



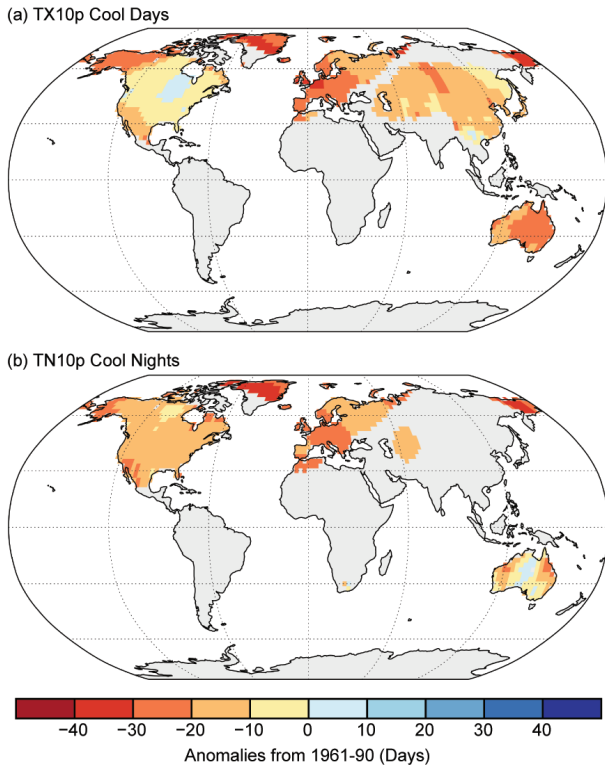


**FIG. 2.6. (a) Cool days (TX10p) and (b) cool nights (TN10p) anomaly maps for 2017 (GNCHDEX).**

western U.S. and Canada experienced occurrences of warm days lower than the threshold. Near-average or higher than the threshold occurrences of warm days occurred during boreal spring (MAM), particularly over northwest Russia and China, where more than ten extra warm days were observed.

With the exception of the eastern U.S. and northern Europe, all areas with available data saw around five or more warm days than average in the boreal summer (JJA). During this period, numerous warm temperature events occurred worldwide: Australia experienced its warmest winter on record based on daily maximum temperature observations ([www.bom.gov.au/climate/current/season/aus/archive/201708.summary.shtml](http://www.bom.gov.au/climate/current/season/aus/archive/201708.summary.shtml), accessed 16 February 2018). However, over Southern Australia cool day occurrences during the austral winter (TN10p; Online Fig. S2.5) were higher than average, indicative of very dry conditions early in the season. A severe heatwave also impacted the southwest U.S. during June, resulting in temperatures so high that some aircraft in Arizona and California were grounded ([www.climate.gov/news-features/event-tracker/heat-roasts-western-united-states](http://www.climate.gov/news-features/event-tracker/heat-roasts-western-united-states), accessed 16 February 2018). Also during June, extreme temperatures of at least 50°C were reported for multiple locations in the Middle East

(<https://public.wmo.int/en/media/news/records-fall-amid-heatwaves>, accessed 16 February 2018). A heatwave engulfed southern and eastern Europe during late July and early August, causing human casualties.

Boreal autumn (SON) saw higher-than-threshold occurrences of warm days (TX90p) over most regions except for northern Russia and Europe, where around five fewer warm days than the threshold occurred. For most regions, the anomalous frequency of seasonal warm days was larger than that of seasonal cool days (TX10p; Online Figs. S2.5e–h); however, there were still fewer cool days than the climatological average, giving warm anomalies.

During each season, the vast majority of the globe experienced two to five fewer cool nights than the threshold (TN10p; Online Figs. S2.5m–p) but higher numbers of warm nights (TN90p; Online Figs. S2.5i–l), with scattered areas experiencing warm nights close to the climatological average.

With the exception of JJA, much of the globe experienced minimum daytime temperatures (TXn; Online Figs. S2.6e–h) that were at least 2°C above the 1961–90 average. During JJA, such anomalies were up to 2°C below the climatological average over northeast Europe and East Asia. The former were caused by cyclonic activity, especially in June. The signature of these events is also evident in the reduced frequency of warm days (TX90p) during JJA (Online Figs. S2.5a,b). Anomalies 2°C below average were also experienced over East Asia during SON. Minimum nighttime temperatures (TNn, Online Figs. S2.6m–p) were consistently warm throughout most seasons and were quite large (3°C or higher) over the U.S., Canada, and Europe during MAM and DJF.

#### 4) TROPOSPHERIC TEMPERATURE—J. R. Christy, S. Po-Chedley, and C. Mears

Following the record high global lower tropospheric temperature (LTT) in 2016, LTT decreased by more than 0.1°C in 2017. The annual, globally averaged LTT (the bulk atmosphere below 10-km altitude) was, depending on the dataset, +0.38° to +0.58°C above the 1981–2010 mean. 2017 was generally the second or third warmest year since measurements began in 1958 (Fig. 2.7) and the warmest non-El Niño year.

Direct measurements of LTT by radiosonde datasets have reasonable spatial coverage since 1958. Radiosonde data are complemented by satellites and reanalysis products since late 1978, except JRA-55 reanalyses which begin in 1958. These datasets are described in Christy (2016). These bulk-layer

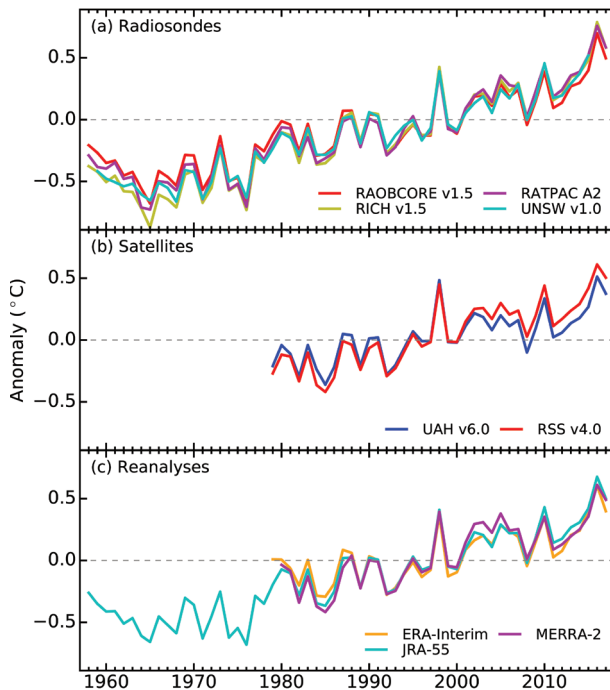


**FIG. 2.7. Anomalies of global mean LTT (°C; 1981–2010 base period): (a) radiosondes, (b) satellites, and (c) reanalyses.**

atmospheric temperatures are closely related to the heat content of the atmospheric climate system and thus are valuable indicators for quantifying heat energy changes expected from rising concentrations of greenhouse gases and other forcings.

The latitude–time depiction of the LTT anomalies (Fig. 2.8) beginning in 1979 illustrates major tropospheric responses to El Niño events, most clearly evident in the tropics (1983, 1987, 1998, 2010, and 2016). The major El Niños in 1998 and 2016 reveal comparable magnitudes of peak anomalies, but 2016 is set against higher background temperatures. Since 2013, few zonal average anomalies have been negative.

Annual global LTT anomalies are closely tied to El Niños and La Niñas, which can be characterized by the Multivariate El Niño Southern Oscillation Index (MEI; Wolter and Timlin 2011) shown in Fig. 2.8a. As noted, 2017 followed a major El Niño (MEI > 2 in early 2016) yet its global LTT experienced a small decline of less than 0.2°C while previous year-to-year declines were greater (e.g., 1999 was over 0.4°C cooler than the El Niño year of 1998). Part of the reason was the rise of El Niño-like characteristics (MEI > 1.4) by May 2017 before La Niña conditions ensued. The LTT anomaly, which generally lags the MEI by 3–5 months, apparently responded with record high values in September and October, thereby mitigating the late-year La Niña cooling effect in the annual average.

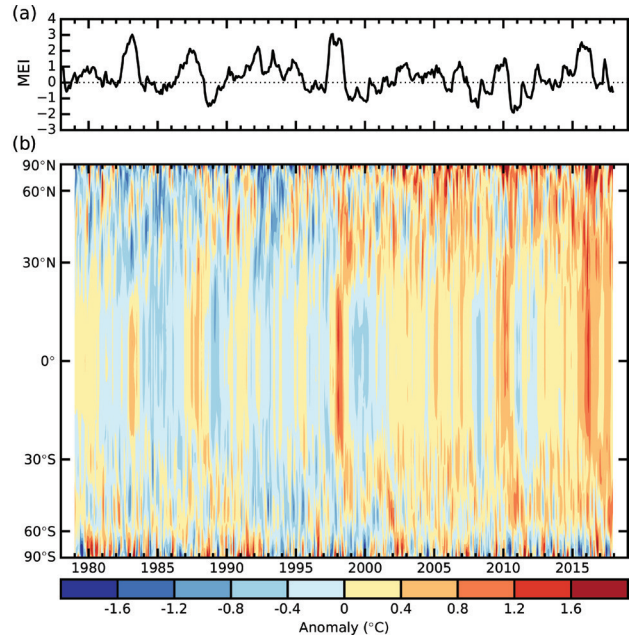


**FIG. 2.8. (a) Multivariate ENSO index (MEI; Wolter and Timlin 2011). (b) Latitude–time depiction of ERA-Interim LTT anomalies (°C; base period of 1981–2010, cosine latitude weighting).**

Annually averaged LTT was above average over most of the globe in 2017 (Plate 2.1e). Regionally, warm anomalies for the year occurred throughout the Arctic poleward of 65°N. The midlatitude belts in both hemispheres featured areas with mostly above-normal temperatures with centers in southwestern North America, southwestern Europe, central China, the northern Pacific Ocean, southern midlatitude oceans, and eastern Australia. The Antarctic was generally cooler than average as were other scattered locations. (Plate 2.1e).

The long-term global LTT trend based on radiosondes (starting in 1958) is  $+0.17^{\circ} \pm 0.02^{\circ}\text{C decade}^{-1}$ . Starting in 1979 and using the average of radiosondes, satellites, and reanalyses (weighted one-third each), the trend is fairly similar, at  $+0.16^{\circ} \pm 0.04^{\circ}\text{C decade}^{-1}$ . The range represents the variation among the individual datasets which serves as a proxy for the structural uncertainty seen in Fig. 2.7 and Table 2.2. Efforts to document and understand the differences among datasets continue. Accounting for the magnitude of the year-to-year variations results in a statistical confidence range of  $\pm 0.06^{\circ}\text{C decade}^{-1}$ , meaning that the trends are significantly positive.

The positive trends noted in this assessment represent the net effect of both anthropogenic (e.g., increasing concentrations of greenhouse gases) and natural forcings. For example, major volcanic eruptions injected solar-reflecting aerosols into the strato-

**TABLE 2.2. Estimates of lower tropospheric temperature decadal trends ( $^{\circ}\text{C decade}^{-1}$ ) beginning in 1958 and 1979 from the available datasets.**

	Global LTT		Tropical LTT		Tropical TTT	
Start Year:	1958	1979	1958	1979	1958	1979
<b>Radiosondes</b>						
RAOBCORE	+0.15	+0.15	+0.14	+0.13	+0.14	+0.13
RICH	+0.19	+0.20	+0.18	+0.17	+0.17	+0.17
RATPAC	+0.18	+0.20	+0.15	+0.15	+0.15	+0.15
UNSW (to 2015)	+0.17	+0.16	+0.15	+0.11	+0.13	+0.10
<b>Satellites</b>						
UAHv6.0 <sup>a</sup>	—	+0.13	—	+0.12	—	+0.12
RSSv4.0 <sup>b</sup>	—	+0.19	—	+0.15	—	+0.19
NOAAv4.0	—	—	—	—	—	+0.21
UWv1.0 <sup>c</sup>	—	—	—	—	—	+0.17
<b>Reanalyses and Climate Models after Reanalyses</b>						
ERA-I	—	+0.13	—	+0.10	—	+0.13
JRA-55	—	+0.16	—	+0.13	—	+0.14
MERRA-2	—	+0.17	—	+0.14	—	+0.15
CMIP5 Mean	+0.21	+0.27	+0.22	+0.29	+0.25	+0.31

<sup>a</sup>The UAH LTT vertical profile is slightly different than the others with much less emphasis on surface emissions and slightly more in the midtroposphere. Calculations indicate UAH LTT would be  $+0.01^{\circ}\text{C decade}^{-1}$  warmer if using the traditional LTT profile represented by other datasets here.

<sup>b</sup>RSS value of TTT utilizes RSSv4.0 of MTT and RSSv3.3 of LST.

<sup>c</sup>UW value of TTT utilizes MTT from UWv1.0 and LST from NOAAv4.0.

sphere in 1963, 1982, and 1991, depressing global temperatures for a few years each time. The latter two events, being early in the current 1979–2017 period, tilted the global trend since 1979 to be more positive by about  $+0.06^{\circ}\text{C decade}^{-1}$  (Christy and McNider 2017). There is evidence that other time-varying factors such as internal climate variability related to oceanic processes, a recent reduction in solar irradiance, and/or the presence of aerosols from natural (e.g., minor volcanic activity) and anthropogenic sources also affected the temperature and likely had a role in reducing post-2000 values and thus contributed to the so-called “warming hiatus” from 2000 to 2014 (Wuebbles et al. 2017).

Christy (2017) examined tropical trends for the layer centered in the midtroposphere (MTT), where trends are expected to respond rapidly to increases in greenhouse gases. However, the tropical MTT profile includes a small portion of the stratosphere where long-term cooling has occurred (not shown). This influence leads to an MTT trend that is cooler than would be measured in the troposphere alone by approximately  $0.03^{\circ}\text{--}0.04^{\circ}\text{C decade}^{-1}$ . Following

the method of Fu et al. (2004), this year’s results are provided from a weighted average of the MTT and LST channels that largely removes the stratospheric portion, producing a better estimate of the full troposphere itself.

Examining the various datasets of the tropical TTT trend for 1979–2017 (Table 2.2), it is noted that the magnitude of the trend is similar to LTT in most cases and always greater than MTT (not shown). Using the average of 102 climate model simulations from the IPCC CMIP-5 (Flato et al. 2013), we see that because of the incorporation of more influence of the upper level tropospheric layers, for which trends are more positive than the lower troposphere (Christy 2017), the TTT trends slightly exceed those of LTT in most cases.

##### 5) STRATOSPHERIC TEMPERATURE—J. R. Christy and C. Covey

The stratosphere is the atmospheric layer above the tropopause ( $\sim 17$  km altitude near the equator,  $\sim 9$  km at the poles). Its upper boundary is  $\sim 50$  km. Radiosondes have observed the stratosphere, typically up to  $\sim 20$  km, with coverage sufficient for global



averaging since 1958. Since 1978 satellites have carried microwave sounding units (MSUs) to monitor the intensity of radiances which is directly related to lower stratospheric temperature (LST). The MSU LST channel detects emissions from ~14 to ~27 km with maximum signal at ~18 km; thus in the deep tropics there is some upper tropospheric influence. Stratospheric sounding units (SSUs) monitor layers completely above the tropopause.

In 2017, the annual globally averaged LST rose about 0.2°C from its value in 2016, which was the record low in six of the nine datasets (Figs. 2.9a–c). Episodes in which the tropopause rises into typically stratospheric levels lead to cooler MSU LST values because upper tropospheric air is cooler than the stratospheric air it displaces. This occurred during the major El Niño event of 2016. The 2017 anomaly was approximately –0.4°C, but varied among the datasets analyzed here by  $\pm 0.2^\circ\text{C}$ .

Observed long-term globally averaged LST time series in Figs. 2.9a–c include three volcanic events

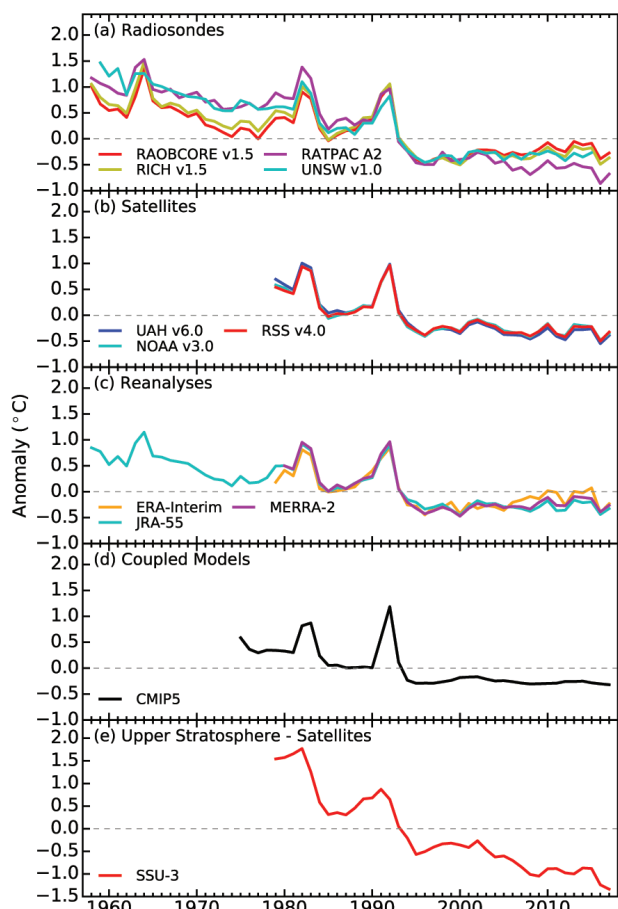


**FIG. 2.9. Time series of annual LST anomalies (°C; 1981–2010 base period): (a) radiosondes, (b) satellites, (c) reanalyses, and (d) coupled climate models. (e) Upper stratospheric temperature anomalies.**

(1963 Mt. Agung, 1982 El Chichón, and 1991 Mt. Pinatubo), whose stratospheric aerosols each led to warming spikes. After Pinatubo (and perhaps El Chichón), LST declined to levels lower than prior to the eruption, giving a stair-step appearance. Ozone depletion and increasing CO<sub>2</sub> in the atmosphere contribute an overall decline, so trends in global LST are clearly negative until approximately 1996.

In Figs. 2.9a–c, the global trends through 2017, based on the average of all displayed datasets, are  $-0.29^\circ$ ,  $-0.27^\circ$ , and  $+0.01^\circ\text{C decade}^{-1}$  for periods beginning in 1958, 1979, and 1996, respectively. The satellite time series are in exceptional agreement with each other ( $r > 0.99$ ) and with reanalyses (highest  $r$  with JRA-55  $> 0.96$ ). The radiosonde datasets are limited by geographical coverage; even so, satellites and radiosondes achieved  $r > 0.95$ .

Absence of lower stratospheric cooling in the global mean since 1996 is due to recovery of the ozone layer, especially at high latitudes, as the Montreal Protocol and its Amendments on ozone-depleting substances has taken effect (Solomon et al. 2017; Randel et al. 2017). The pattern of LST anomalies in 2017 is depicted in Plate 2.1f. Warmer-than-average conditions occurred poleward of 50°S and over the north polar Western Hemisphere (180°E to 360°E). In general below-average temperatures prevailed elsewhere, consistent with the generally negative trends in Figs. 2.9a–c.

Two prominent features of LST are sudden stratospheric warmings (SSWs) and the quasi-biennial oscillation (QBO). SSWs usually appear during the northern polar night. Figures 2.10a,b shows pentad (5-day average) LST anomalies for the north and south polar caps (65°–85° latitude average, values smoothed 1–2–1 in time). Excursions over the North Pole often exceed 10°C, with 5°C departures in almost every year. 2017 did not experience an event  $> 5^\circ\text{C}$  in the north, but in pentad 66, near the end of 2016, both polar caps exceeded 5°C (unsmoothed). Because these events are related to the breakdown of the polar night vortex, they occur less frequently and with less intensity over the South Pole due to its more zonally symmetric circulation. Sudden cooling episodes also occur and are related to the impact of ozone depletion in spring over the south polar cap.

The QBO is typically defined by the time–height pattern of zonal wind anomalies in the tropics, but it can also be detected in the LST temperature anomalies. The QBO alternates between westerly (warm) and easterly (cold) wind shear regimes in the tropical stratosphere in which the feature propagates downward from the upper stratosphere and dissipates near

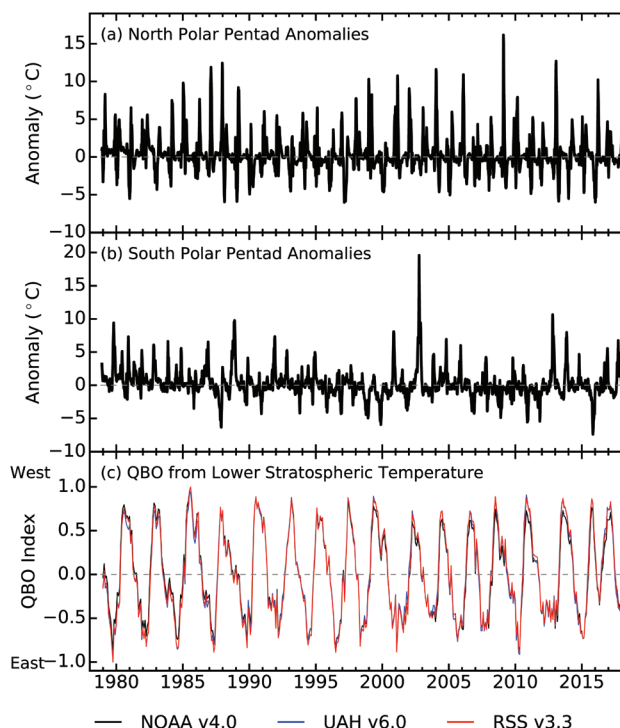


**FIG. 2.10. Time series of pentad (5-day averages, smoothed by 1-2-1 in time) LST anomalies (°C) for (a) northern and (b) southern polar caps bounded by 65° and 85° latitude. (c) Monthly time series of QBO index as averaged from UAH, RSS, and NOAA LST.**

the tropopause. Figure 2.10c extends the temperature-based QBO index of Christy and Drouilhet (1994) through 2017.

The 16 QBO periods in Fig. 2.10c indicate a mean length of 27.4 months. The longest (35 months) ended in April 2002, and the shortest by a substantial margin (17 months) concluded in March 2017. The cycle that finished in 2017 included the weakest (warmest) easterly regime in this 39-year history.

There is relatively high confidence in explaining the variations of global mean stratospheric temperature. When climate models used in the IPCC AR5 (Flato et al. 2013) are provided with forcing estimates related to changes in ozone, carbon dioxide, volcanic aerosols, solar variability, etc., the multi-model mean agrees with the satellite observations to a high level ( $r > 0.96$ ). Figure 2.9d shows the mean of 102 CMIP-5 simulations of the LST time series. Aquila et al. (2016) examined forcing agents and concluded that about  $\frac{1}{3}$  of the decline was due to increasing concentrations of greenhouse gases and  $\frac{1}{3}$  to ozone-depleting substances. At higher levels of the stratosphere, in the layer monitored by the SSU channel 3 ( $\sim 40$ – $50$  km altitude; Fig. 2.9e), the observed trend is approximately  $-0.7^{\circ}\text{C decade}^{-1}$  of which 75% is estimated to result from enhanced greenhouse gas concentrations

and most of the remaining decline from ozone loss (Aquila et al. 2016).

### c. Cryosphere

1) PERMAFROST THERMAL STATE—J. Noetzli, H. H. Christiansen, P. Deline, M. Gugliemin, K. Isaksen, V. E. Romanovsky, S. L. Smith, L. Zhao, and D. A. Streletskiy

Permafrost is an invisible component of the cryosphere in polar and high mountain areas and is defined as earth materials (eg., soil, rock) that exist at or below  $0^{\circ}\text{C}$  continuously for at least two consecutive years. Long-term monitoring of its conditions primarily relies on ground temperatures measured in boreholes. Overlying the permafrost is the active layer, which thaws in summer and refreezes in winter. Globally, permafrost observation data (thermal state and active layer dynamics) are collected in the database of the Global Terrestrial Network for Permafrost (GTN-P; Biskaborn et al. 2015), which is part of the Global Climate Observing System (GCOS) of the World Meteorological Organization (WMO).

The long-term trend of rising permafrost temperatures worldwide continued in 2017. There is, however, considerable regional variability, mainly depending on the temperature range, surface characteristics, and ground ice content at the site. The general picture is that a more substantial increase is observed in regions with cold continuous permafrost compared to areas with warm permafrost at temperatures within  $2^{\circ}$ – $3^{\circ}\text{C}$  of the freezing point. This is mainly a result of latent heat effects associated with melting of ground ice. The lowest permafrost temperatures—and thus highest warming rates—were observed in the high Arctic of northern Alaska, Canada, Svalbard, and Russia, as well as in shaded flanks of high mountain peaks. Record high temperatures were observed in 2017 for nearly all sites in Alaska and in northwestern Canada. In other areas (northeastern Canada, Nordic countries), permafrost temperatures measured in 2016/17 were among the highest ever recorded (updates from Christiansen et al. 2010; Romanovsky et al. 2017; Smith et al. 2015, 2017; Ednie and Smith 2015; Boike et al. 2018). A detailed description of permafrost conditions in the Arctic and sub-Arctic is provided in Section 5g. Here, the focus is on updated results from mountain permafrost (European Alps, Nordic countries, and central Asia) and permafrost in continental Antarctica (Streletskiy et al. 2017).

In mountain permafrost in the European Alps most boreholes are located between 2600 and 3000 m a.s.l. (above sea level), with permafrost temperatures typically above  $-3^{\circ}\text{C}$ . Permafrost temperatures have generally increased in the upper 20 m (Fig. 2.11), espe-

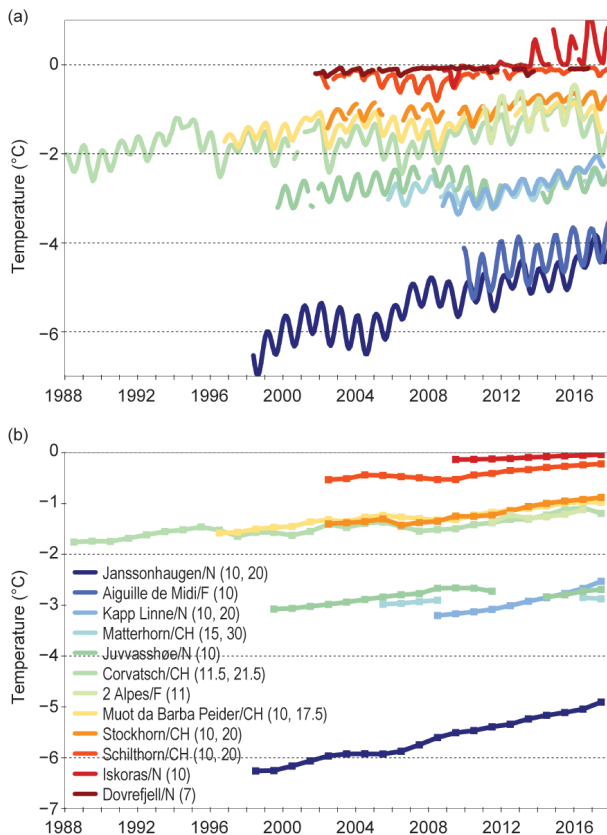


**FIG. 2.11. Temperature (°C) measured in permafrost boreholes in the European Alps and Nordic countries at depths of (a) ~10 m (monthly means) and (b) ~20 m (annual means). (Sources: Swiss Permafrost Monitoring Network PERMOS; Norwegian Meteorological Institute and the Norwegian Permafrost Database NORPERM; French Permafrost Monitoring Network PermaFRANCE.)**

cially since 2009 and accentuated in 2015 (PERMOS 2016). The past two winters (2015/16 and 2016/17) interrupted this warming trend: a late and thin snow cover resulted in lower permafrost temperatures in debris slopes and on rock glaciers, which were visible down to about 20-m depth (updated from PERMOS 2016; Noetzli et al. 2018, paper to be presented at *5th European Conf. Permafrost, EUCOP*), for example, in the borehole on Corvatsch-Murtèl. This short-term cooling has also led to a decrease of rock glacier creep velocities relative to the previous years at multiple sites in Switzerland (updated from PERMOS 2016; Noetzli et al. 2018, paper to be presented at *5th European Conf. Permafrost, EUCOP*). Rock temperatures in shaded flanks of the highest peaks can be as low as temperatures measured in the Arctic (Fig. 2.11; Noetzli et al. 2016). They closely follow air temperatures and the influence of snow is negligible (Gruber et al. 2004; PERMOS 2007), but only few and relatively short time series are available. In the

Aiguille du Midi Mont Blanc (France), permafrost temperature at 10-m depth continued to increase in the past two years and is expected to be at a very high level compared to the past decades (Fig. 2.11; updated from Magnin et al. 2015).

In Nordic countries, mountain permafrost temperatures continued to increase (updated from Isaksen et al. 2007; Christiansen et al. 2010). In southern Norway (Juvvasshøe) ground temperatures in 2017 were near-record high, a warming that followed a period of cooling between 2010 and 2013. Monitoring (since 2008) in northern Norway (Iskoras) shows evidence of thawing permafrost with ground temperatures well above 0°C at 10-m depth since 2013/14 (Fig. 2.11). In the warm permafrost of the higher elevations of central Asia, ground temperatures are estimated to be in the range of -2° to -0.5°C (Zhao et al. 2017) and have increased by up to 0.5°C decade<sup>-1</sup> since the early 1990s (update from Zhao et al. 2010). On the Qinghai-Tibetan Plateau (Fig. 2.12), the increase in ground temperature at 10-m depth

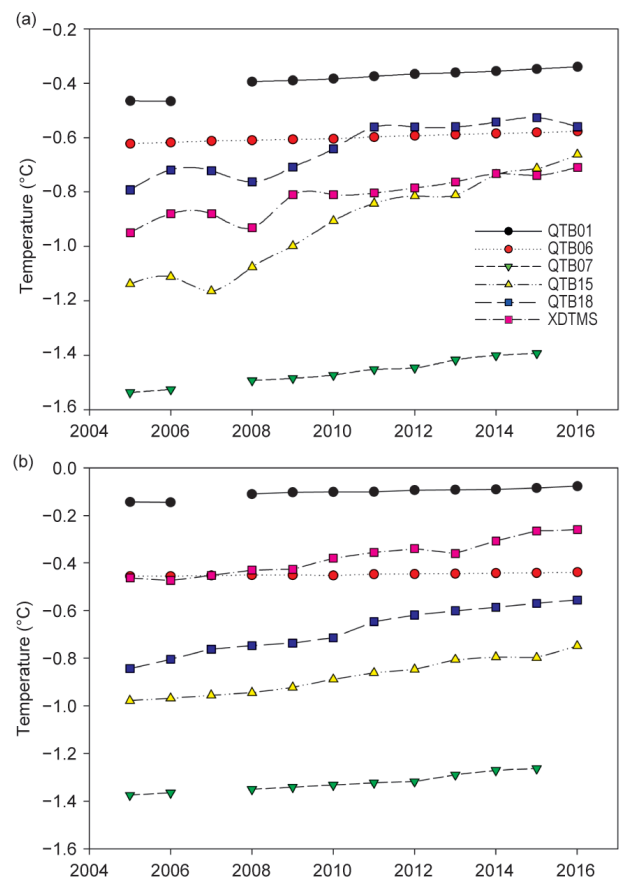


**FIG. 2.12. Temperature (°C) measured in permafrost boreholes along the Qinghai-Xizang Highway on the Tibetan Plateau at (a) 10 and (b) 20 m depth. (Source: Cryosphere Research Station on Qinghai-Xizang Plateau, CAS.)**



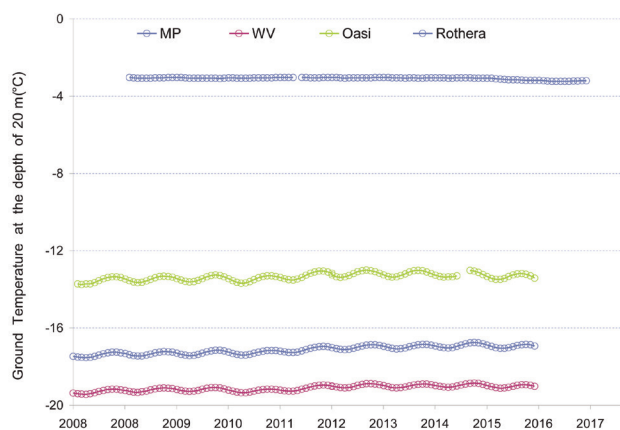


**FIG. 2.13. Observed borehole temperatures (°C) in Antarctica at 20-m depth (monthly means): WV = Wright Valley; MP = Marble Point; Oasi in continental Antarctica; and Rothera in maritime Antarctica. (Source: Insubria Permafrost Database.)**

reached 0.5°C (site QTB15) between 2005 and 2016, and up to 0.3°C at 20-m depth. Along the latitudinal transect in Victoria Land, continental Antarctica [between 77°31'S, Wright Valley (WV in Fig. 2.13) and 74°41'S, Oasi] permafrost temperature at 20-m depth is among the lowest recorded during the period of observation. It continued to increase despite stable air temperatures since 1960, and the temperature rise is more pronounced at the southern coast (Marble Point; MP in Fig. 2.13). In contrast, temperatures measured in the Rothera borehole (67°S) in the northern Antarctic Peninsula decreased in the past two years. This is mainly due to regional cooling of the atmosphere and the influence of snow cover (Guglielmin et al. 2014).

An increasing trend in active layer thickness (ALT) since the mid-1990s is observed

in most permafrost regions except the Antarctic Peninsula, where ALT has been stable or even decreased since 2009 (Hrbáček et al. 2018). Extremely warm summer conditions in the Arctic in 2016 resulted in extremely high ALT values. They were reinforced in North America in the summer of 2017 resulting in the ALT close to the recorded maximum. In contrast, in Europe and along the Russian Arctic coast, the cold summer of 2017 led to a decrease in ALT relative to the previous year to values around the long-term mean (see Chapter 5 for more details).

## 2) NORTHERN HEMISPHERE CONTINENTAL SNOW COVER EXTENT—D. A. Robinson

Annual snow cover extent (SCE) over Northern Hemisphere (NH) lands averaged 25.8 million km<sup>2</sup> in 2017. This is 0.7 million km<sup>2</sup> more than the 48-year average (mapping extends back to late 1967; however, several early years in the record are incomplete) and ranks as the eighth most extensive cover on record (Table 2.3 and Fig. 2.14). This is 1.2 million km<sup>2</sup> greater than the 2016 mean extent. Snow extent over both Eurasia and North America, including the

**TABLE 2.3. Monthly and annual climatological information on Northern Hemisphere and continental snow extent between Nov 1966 and Dec 2017. Included are the numbers of years with data used in the calculations, means, standard deviations, 2017 values and rankings. Areas are in millions of km<sup>2</sup>. 1968, 1969, and 1971 have 1, 5, and 3 missing months respectively, thus are not included in the annual calculations. North America (N. Am.) includes Greenland. Ranks are from most extensive (1) to least (ranges from 48 to 52 depending on the month).**

	Years	Mean SCE	Std. Dev.	2017	2017 NH Rank	Eurasia Rank	N. Am. Rank
Jan	51	47.2	1.6	49.2	6	7	13
Feb	51	46.0	1.8	46.0	22	19	37
Mar	51	40.5	1.9	40.1	28	27	32
Apr	51	30.5	1.7	31.2	16	21	21
May	51	19.3	2.0	20.7	12	12	18
Jun	50	9.6	2.4	9.3	27	20	40
Jul	48	4.0	1.2	3.5	28	36	19
Aug	49	3.0	0.7	2.9	21	28	14
Sep	49	5.4	0.9	6.2	10	12	15
Oct	50	18.4	2.7	21.2	9	11	7
Nov	52	34.1	2.1	36.0	9	17	7
Dec	52	43.7	1.9	43.6	33	31	24
Ann	48	25.1	0.8	25.8	8	11	15

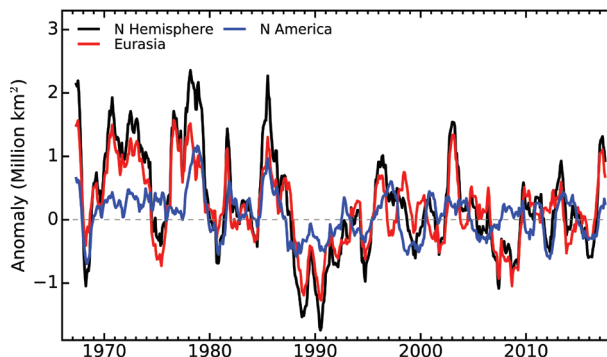


**FIG. 2.14. Twelve-month running anomalies of monthly snow cover extent ( $\times 10^6 \text{ km}^2$ ) over NH lands as a whole (black), Eurasia (red) and North America (blue) plotted on the 7th month using values from Nov 1966 to Dec 2017. Anomalies are calculated from NOAA snow maps. Mean hemispheric snow extent is 25.1 million  $\text{km}^2$  for the full period of record. Monthly means for the period of record are used for 9 missing months between 1968 and 1971 in order to create a continuous series of running means. Missing months fall between Jun and Oct, no winter months are missing.**

Greenland ice sheet, is considered in this analysis. Monthly SCE in 2017 ranged from 49.2 million  $\text{km}^2$  in January to 2.9 million  $\text{km}^2$  in August. SCE is calculated at the Rutgers Global Snow Lab from daily SCE maps produced by meteorologists at the National Ice Center (a U.S. joint NOAA, Navy, and Coast Guard facility), who rely primarily on visible satellite imagery to construct the maps.

January 2017 NH SCE was over 2 million  $\text{km}^2$  above average, which exceeds the average by greater than one standard deviation (SD) and ranks sixth highest of the past 51 Januaries. Eurasia (EU) maintained above-average SCE in February, ranking 19th highest, while SCE over North America (NA) decreased considerably to 15th lowest. Given the greater land area of EU than NA, this resulted in a NH continental ranking of 22nd highest. Conditions across the two continents evened out in March, with each having the 21st highest SCE in April. Melt over both continents was delayed compared to many recent springs, with May SCE the 12th most extensive. Seasonally, spring (March–May) NH SCE was the largest since 2003 and the third most extensive since 1987. June 2017 SCE over Northern Hemisphere land was close to the long-term average, yet the most extensive since 2004, and by far the most extensive since 2007. June cover disappeared rather quickly over NA early in the month, resulting in the 11th smallest SCE on record, while Eurasia SCE was slightly above average but the largest since 2003 and third largest since 1997.

There was an early onset of the 2017/18 snow season across the NH, with NH September cover the tenth most extensive for the month on record. This behavior continued through the remainder of autumn over both EU and NA, with NH SCE ninth most extensive on record for both October and November, each month close to one SD above average. Autumn (September–November) NH SCE was the third highest among the 49 years with complete data, behind 2014 and 1996. As winter began, the pace of the southward snow advance into the middle latitudes slowed, resulting in the 20th least extensive NH snow cover of the past 52 Decembers.

SCE over the contiguous United States was well above average in January 2017, the 13th most extensive on record; however, cover decreased considerably in February and was 12th lowest on record for the month, remaining below average throughout spring. Autumn cover started out on the high side but rankings declined through the end of 2017, with December SCE ranking 20th lowest.

Maps depicting daily, weekly, and monthly conditions, daily and monthly anomalies, and monthly climatologies for the entire period of record may be viewed at the Rutgers Global Snow Lab website (<http://snowcover.org>). Monthly SCE for the NH, EU, NA, contiguous US, Alaska, and Canada are also posted, along with information on how to acquire weekly areas and the weekly and monthly gridded products. Section 5: describes SCE as well as snow cover duration and snow water equivalent.

### 3) ALPINE GLACIERS—M. Peltó and the WGMS network

The World Glacier Monitoring Service (WGMS) record of mass balance and terminus behavior (WGMS 2017) provides a global index for alpine glacier behavior. Glacier mass balance is the difference between accumulation and ablation, reported here in mm of water equivalence (w.e.) and is a GCOS headline indicator. Mean annual glacier mass balance in 2016 was  $-847 \text{ mm}$  for the 37 long-term reference glaciers and  $-761 \text{ mm}$  for all 140 monitored glaciers (Fig. 2.15). Of the reporting reference glaciers, only one had a positive mass balance. Preliminary data reported to the WGMS in 2017 from Austria, Canada, China, France, Italy, Kazakhstan, Norway, Russia, Switzerland, and United States indicate that 2017 will be the 38th consecutive year of negative annual balances with a mean loss of  $-1036 \text{ mm}$  for 29 reporting reference glaciers, with three glaciers reporting a positive mass balance (<http://wgms.ch/latest-glacier-mass-balance-data/>, accessed 2 Feb 2018).

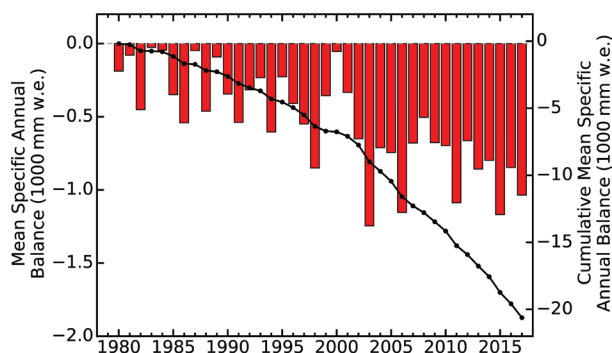


**FIG. 2.15. Global alpine glacier annual mass balance record (mm w.e.) of reference glaciers submitted to the WGMS 1980–2017 (see also: <http://wgms.ch/latest-glacier-mass-balance-data/>).**

The ongoing global glacier retreat affects human society by raising sea levels, changing seasonal stream runoff, and increasing geohazards (Huss et al. 2017a). Huss and Hock (2018) indicate that approximately half of 56 glaciated watersheds globally have already passed peak glacier runoff. Rounce et al. (2017) identify the widespread expansion of glacier lakes due to retreat in Nepal from 2000 to 2015, which pose a glacier lake outburst flood hazard.

Glacier retreat is a reflection of strongly negative mass balances over the last 30 years (Zemp et al. 2015). Marzeion et al. (2014) indicate that most of the recent mass loss, during 1991–2010, is due to anthropogenic forcing. The cumulative mass balance loss from 1980 to 2016 is  $-19.9$  m, the equivalent of cutting a 22-m thick slice off the top of the average glacier (<http://wgms.ch/latest-glacier-mass-balance-data>, see Figure 2). The trend is remarkably consistent from region to region (WGMS 2017). WGMS mass balance based on 41 reference glaciers with a minimum of 30 years of record is not appreciably different from that of all glaciers at  $-19.1$  m. The decadal mean annual mass balance was  $-228$  mm in the 1980s,  $-443$  mm in the 1990s,  $-676$  mm for the 2000s, and  $-896$  mm for 2010–17 (WGMS 2017). The declining mass balance trend during a period of retreat indicates alpine glaciers are not approaching equilibrium, and retreat will continue to be the dominant terminus response.

Exceptional glacier melt was noted across the European Alps in 2017, along with high snowlines (Fig. 2.16), and contributed to large negative mass balances of glaciers on this continent (Swiss Academy of Sciences 2017). In the European Alps, annual mass balance has been reported for nine reference glaciers from Austria, France, Italy, and Switzerland. All had negative annual balances exceeding  $-1000$  mm with a mean of  $-1664$  mm. This continues the

pattern of substantial negative balances in the Alps that continue to lead to terminus retreat. In 2016, in Switzerland 94 glaciers were observed: 82 retreated, 7 were stable, and 5 advanced (Huss et al. 2017b). In 2016, Austria observed 84 glaciers: 82 retreated, 1 was stable, and 1 advanced; the average retreat rate was 25 m (Lieb and Kellerer-Pirklbauer 2018).

In Norway and Svalbard, terminus fluctuation data from 36 glaciers with ongoing assessment indicate that in 2016, 32 retreated, 3 advanced, and 1 was stable. The average terminus change was  $-12.5$  m (Kjøllmoen et al. 2017). Mass balance surveys with completed results for 2017 are available for nine glaciers; six of the nine had negative mass balances with an average loss of  $-80$  mm w.e. In western North America, data for 2017 have been submitted from eight reference glaciers in Alaska and Washington in the United States, and British Columbia in Canada. Seven of these eight glaciers reported negative mass balances with an overall mean of  $-1020$  mm. Winter and spring 2017 had above-average snowfall, but ablation conditions were above average. In Alaska mass losses from 2002 to 2014 have been  $-52 \pm 4$  gigatons  $\text{yr}^{-1}$ , as large as any alpine region in the world (Wahr et al. 2016).

In the high mountains of central Asia, four glaciers reported data from China, Kazakhstan, and Nepal.

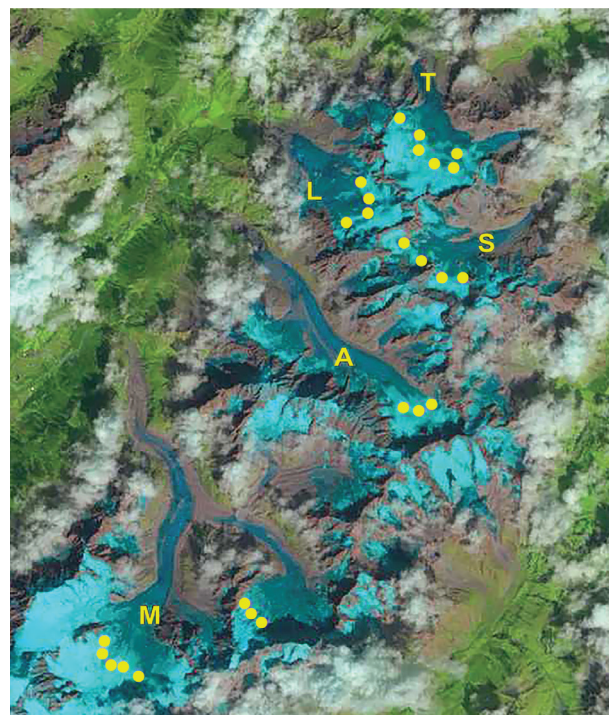


**FIG. 2.16. Landsat image from 19 Aug 2017 illustrating the snowline on Mont Blanc glaciers with one month left in the melt season (M = Mer de Glace; A = Argentière; S = Saleina; L = Le Tour; T = Trient).**



All four were negative, with a mean of  $-674$  mm. This is a continuation of regional mass losses, such as reported by King et al. (2017) who found for 2000–15 the mean annual mass balance of 32 glaciers in the Mount Everest region was  $-520 \pm 220$  mm.

The mass balance of the Arctic glaciers reported in the WGMS is described in Section 5f.

#### d. Hydrological cycle

1) SURFACE HUMIDITY—K. Willett, D. Berry, M. Bosilovich, and A. Simmons

2017 was a humid year over land and ocean in terms of surface specific humidity ( $q$ ; Figs. 2.17a–d). Over land it was comparable with the El Niño–driven peak in 2010 but lower than those of 1998 and 2016. Interestingly, compared with other post-El Niño years of 1999 and 2011, the decline from the El Niño–driven peak was much smaller. However, 2017 saw generally neutral ENSO conditions with

weak La Niña conditions both at the beginning and end of the year, whereas 1999 and 2011 each had a strong La Niña present. Over ocean, the moisture levels at the surface over the last ~3 years have been higher than at any other time during the record according to the reanalyses. There are currently no in situ-only datasets for comparison beyond 2015, but this feature is consistent with high global sea surface temperatures (Section 2b1) and total column water vapor (Section 2d2).

Despite high surface moisture levels (specific humidity), in terms of relative humidity (RH), the atmosphere remained drier than average over land and near average over oceans (Figs. 2.17e–h). ERA-Interim and JRA-55 reanalyses show low RH anomaly values, comparable with the lowest years on record. The HadISDH in situ RH product is similar interannually to ERA-Interim and JRA-55, but more moderate. MERRA-2 is similar interannually but

with significant deviations that are thought to be linked to variability in precipitation forcing (Reichle and Liu 2014; Willett et al. 2016).

Month-to-month, ERA-Interim and HadISDH also track similarly. Variability was low over ocean during 2017, but over land both RH and  $q$  declined throughout the year. December had the driest monthly mean anomaly with respect to both variables.

Global average HadISDH is consistently higher than ERA-Interim for both variables. HadISDH has gaps over the particularly dry regions of South America, Africa, and Australia and also over Antarctica where dry anomalies are widespread in ERA-Interim (Plate 2.1 and Online Fig. S2.12). This is a large source of uncertainty for in situ products and may explain some of the difference. Indeed, when spatially matched, ERA-Interim and HadISDH are more similar (Figs. 2.17 a and e dotted). The data sparse regions and regions of poor data quality are also where reanalyses differ most (Plate 2.1b and Online Figs.

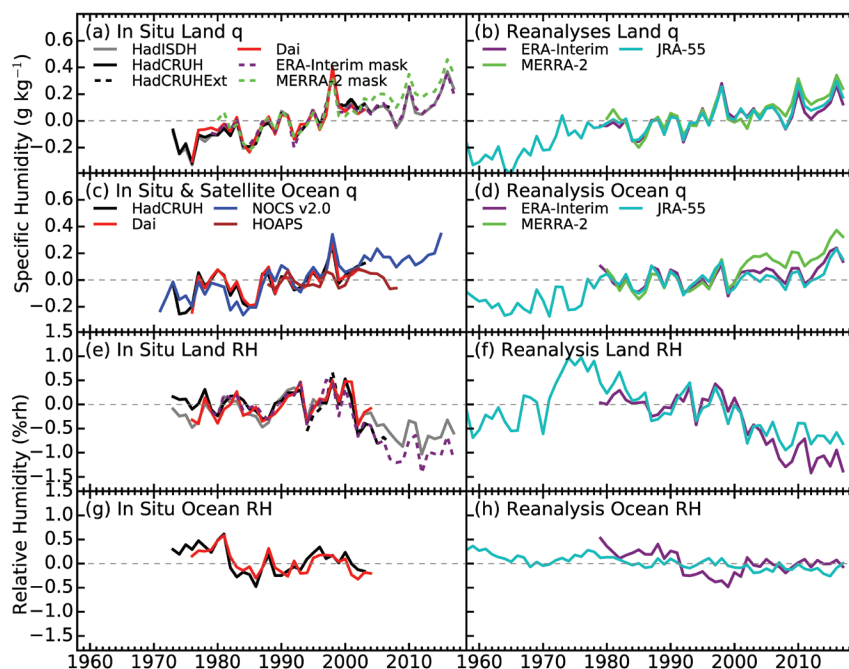


**FIG. 2.17.** Global average surface humidity annual anomalies (1979–2003 base period). For the in situ datasets 2-m surface humidity is used over land and ~10-m over the oceans. For the reanalysis 2-m humidity is used over the whole globe. For ERA-Interim ocean series-only points over open sea are selected and background forecast values are used as opposed to analysis values because of unreliable use of ship data in producing the analysis. All data have been adjusted to have a mean of zero over the common period 1980–2003 to allow direct comparison, with HOAPS given a zero mean over the 1988–2003 period. Additional dotted lines are plotted for ERA-Interim and MERRA-2 reanalyses where they have been spatially matched to HadISDH for comparison. [Sources: HadISDH (Willett et al. 2013, 2014); HadCRUH (Willett et al. 2008); Dai (Dai 2006); HadCRUHExt (Simmons et al. 2010); NOCSv2.0 (Berry and Kent 2009, 2011); HOAPS (Fennig et al. 2012) and reanalyses as in Fig. 2.1].



S2.10 and S2.11) due to model differences and how/which observational datasets are used.

Spatially, ERA-Interim and HadISDH are similar. The annual average  $q$  anomaly patterns for 2017 were predominantly moist but more muted than in 2016 (Plate 2.1a; Online Figs. S2.10 and S2.11). The strongly moist anomalies over India to China and south to Southeast Asia were still prominent but to a lesser degree. Dry anomalies were more widespread and quite zonal; there were bands of dry anomalies around 30°–60°N and 0°–30°S. Dry anomalies over eastern Brazil, South Africa, and Iran/Afghanistan/Pakistan persisted from 2016. Additional dry anomalies developed over eastern Australia and Spain during 2017, stronger in ERA-Interim than HadISDH. The dry anomaly over East Africa, a data sparse and therefore uncertain region, was stronger than 2016 in ERA-Interim but not MERRA-2.

Spatial patterns of RH were predominantly negative (Plate 2.1b; Online Fig. S2.12) and broadly similar to both 2016 and the long-term drying trend patterns. Humid anomalies were apparent over southern Africa around Botswana and Zimbabwe in 2017 that were dry in 2016. All regions showing dry  $q$  anomalies in 2017 had spatially more extensive corresponding dry RH anomalies over land and ocean. This shows the importance of looking at both variables in tandem. While a region may be moister than average it could be relatively drier if the regional temperature anomaly is particularly high. The combination of moisture, closeness to saturation, and temperature can lead to different societal impacts in terms of water availability for people and plants, flooding, and heat stress.

There is currently no in situ-only marine product (Willett et al. 2017). The decline in spatial coverage and data quality has made it difficult to continue or develop new in situ marine humidity monitoring products and resulted in the use of background forecast fields instead of analysis fields for ERA-Interim marine humidity in this section. Although satellite products can provide measures of water vapor, and total column water vapor (TCWV) has good interannual agreement with global surface  $q$ , these are not directly comparable with in situ observations and records are shorter. Surface  $q$  can be derived from brightness temperature based on empirical relationships with in situ data. Several datasets were compared alongside the in situ-only NOCSv2.0 marine  $q$  product (Berry and Kent 2009, 2011; Prytherch et al. 2015) and to reanalyses (Schröder et al. 2018). Considerable differences were found. Over land, derivations are complicated by the diverse surface properties. The ability to monitor the climate fully depends on

a comprehensive suite of observations with sufficient numbers that are long term and of climate quality (Thorne et al. 2018).

## 2) TOTAL COLUMN WATER VAPOR—C. Mears, S. P. Ho, J. Wang, and L. Peng

As Earth's surface and the lower troposphere warm, the total column water vapor (TCWV) is expected to increase under the assumption of near-constant relative humidity, and in turn amplify the initial warming through positive water vapor feedback. Thus, measurements of TCWV provide an important check to estimates of temperature increase in addition to the role of changing TCWV in the global hydrological cycle. In 2017, total column water vapor (TCWV) retreated from record levels in 2016 but remained above the 1981–2010 climatological average in most locations. Estimates are available from satellite-borne microwave radiometers over ocean (Mears et al., 2018), COSMIC GPS-RO (Global Positioning System–Radio Occultation) over land and ocean (Ho et al. 2010a,b; Teng et al. 2013; Huang et al. 2013), and ground-based GNSS (Global Navigation Satellite System) stations (Wang et al. 2007) over land. An anomaly map for 2017 (Plate 2.1r) was

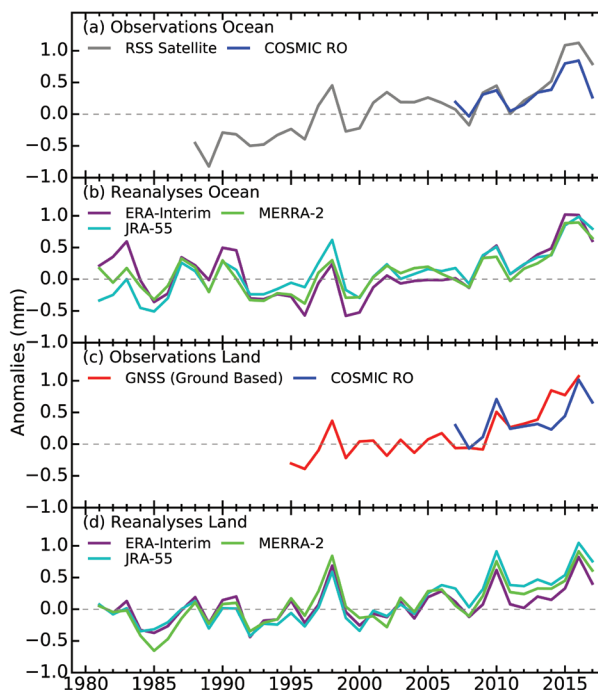


**FIG. 2.18. Global mean total column water vapor annual anomalies (mm) for (a),(b) ocean only and (c),(d) land only for observations and reanalysis (see Fig. 2.1 for reanalysis references) averaged over 60°N–60°S. Shorter time series have been adjusted so that there is zero mean difference relative to the mean of the three reanalyses over the 2006–14 period.**

made by combining data from satellite radiometers over ocean and COSMIC GPS-RO over land. Much of the globe showed small wet anomalies, except for dry anomalies in the central tropical Pacific Ocean and the southeastern tropical Indian Ocean, and a large wet anomaly in the western Pacific warm pool and over the maritime continent, consistent with the presence of La Niña conditions. The patterns in TCWV over the ocean are confirmed by COSMIC ocean measurements and by output from the MERRA-2, ERA-Interim, and JRA-55 reanalyses (not shown). Over land, the patterns from COSMIC are in general agreement with the reanalysis output.

Over the ocean, the TCWV anomaly time series (Figs. 2.18a,b) from reanalysis and microwave radiometers show maxima in 1982/83, 1987/88, 1997/98, 2009/10, and 2015/16 associated with El Niño events. The 2015/16 anomaly is the largest recorded in all datasets. The radiometer data show a discernible increasing trend, while the different reanalysis products show a wide range of long-term trends over the entire period but agree well with the radiometer data after the mid-1990s. The COSMIC data show the same general features as both the radiometer and reanalysis data after COSMIC began in 2007. After the 2015/16 peak, all datasets show a return to drier conditions due to the onset of La Niña but remained wetter than the 1981–2010 normal for almost all latitudes.

Over land, average anomalies from the ground-based GNSS stations are used in place of the satellite radiometer measurements (Figs. 2.18c,d). The various reanalysis products, COSMIC, and GNSS are in good agreement. A land-and-ocean Hovmöller plot derived from JRA-55 (Fig. 2.19) indicates a long-term increase in TCWV at all latitudes, with less variability outside

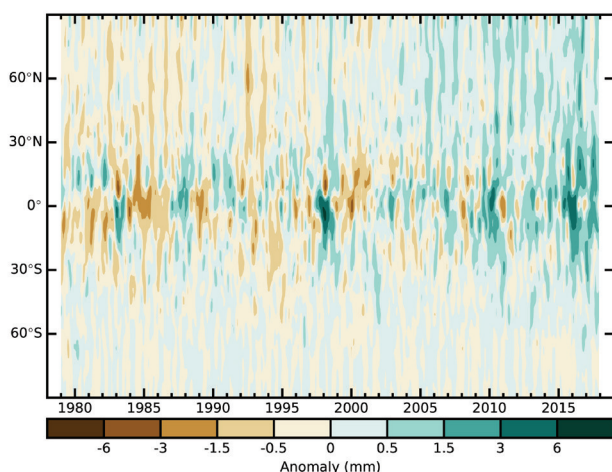


**FIG. 2.19.** Hovmöller plot of TCWV anomalies (mm; base period 1981–2010) including both land and ocean derived from the JRA-55 reanalysis

the tropics. Previous strong El Niño events (1983/84 and 1997/98) showed pronounced drying events in the years following the El Niño events, which were not seen after the 2015/16 event.

### 3) UPPER TROPOSPHERIC HUMIDITY—V. O. John, L. Shi, E.-S. Chung, R. P. Allan, S. A. Buehler, and B. J. Soden

In the atmosphere as a whole, water vapor is the principal greenhouse gas (Held and Soden 2000). Despite water vapor in the upper troposphere being insignificant by total mass when compared to the total column, it nevertheless contributes a major part to the feedbacks present in the climate system. Thus, upper tropospheric water vapor is responsible for most of the tropospheric radiative cooling (Manabe and Möller 1961), and the radiative effect of water vapor is proportional to relative changes in the amount of water vapor in the upper troposphere (John and Soden 2007).

Following John et al. (2017), upper tropospheric (relative) humidity (UTH) is monitored on a global scale by two independent global satellite UTH datasets: (1) the High Resolution Infrared Sounder (HIRS) dataset (Shi and Bates 2011) and (2) the microwave-based UTH dataset (Chung et al. 2013). In these datasets, UTH represents a Jacobian weighted average of relative humidity in a broad layer which is roughly between 500 and 200 hPa but varies depending upon atmospheric humidity profile. Both datasets have been constructed through careful bias corrections and intersatellite calibration. As the microwave-based UTH dataset only begins in 1999, anomalies are computed relative to the 2001–10 base period.

Figure 2.20 shows the area-weighted mean de-seasonalized anomaly time series of UTH for 60°N–60°S using two observational datasets as described later in this section: one from HIRS and the other

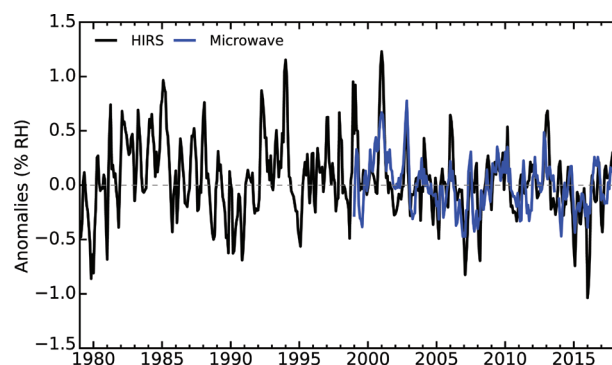


**FIG. 2.20.** Time series of UTH anomalies (% RH; 2001–10 base period) using HIRS (black) and microwave (blue) datasets. Time series are smoothed to remove variability on time scales shorter than three months.

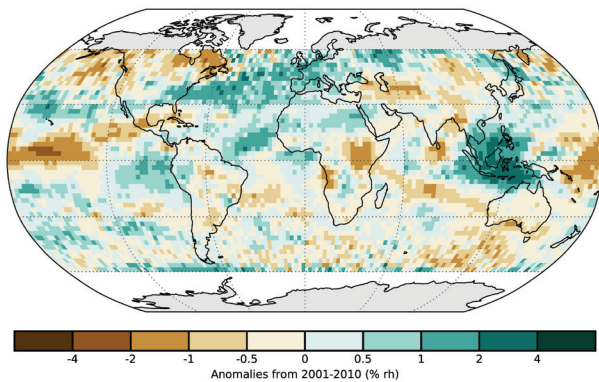


**FIG. 2.21. Annual average UTH anomalies (% RH, 2001–10 base period) for 2017 based on the “clear-sky” HIRS UTH dataset.**

from microwave humidity sounder measurements. The anomalies are close to zero in 2017 and are fairly similar to the previous year, even though 2016 began with an El Niño whereas there were neutral or weak La Niña conditions in 2017. To maintain the same relative humidity, warmer air has to contain more water vapor (have a higher specific humidity). Therefore, the presence of a near-zero decadal trend in the UTH requires an increase in absolute (specific) humidity in step with the warming upper troposphere (Section 2b4) and hence is consistent with a positive water vapor feedback (Chung et al. 2016). Good agreement between the two independent datasets despite their differences in sampling—microwave data having an almost all-sky sampling whereas HIRS data sample mainly clear-sky scenes—provides confidence in the observed long-term behavior of UTH (John et al. 2011). The higher short-term variability in the HIRS time series arises from the sampling issues discussed by John et al. (2011). The spatial variation of annual average UTH anomalies for 2017 (Plate 2.1q for microwave data and Fig. 2.21 for HIRS data) shows dry anomalies over the central Pacific and moist anomalies over the maritime continent, which reflect neutral ENSO conditions during the year; however, the moist anomaly seen in the eastern Pacific is typical for El Niño conditions. The dry anomaly over the Indian subcontinent is an indication of the below-normal monsoon rainfall in 2017 (Sections 2d9, 7g4).

#### 4) PRECIPITATION—R. S. Vose, R. Adler, A. Becker, and X. Yin

Precipitation over global land areas in 2017 was clearly above the long-term average (Fig. 2.22). All available datasets are consistent on this point, but there is a wide range of estimates across the analyses (ranging from 15 to 80 mm above average). The datasets with the most complete global coverage, that is, the gauge-based product from the Global Precipitation

Climatology Centre (GPCC; Becker et al. 2013) and the blended gauge–satellite product from the Global Precipitation Climatology Project (GPCP; Adler et al. 2003), both depict 2017 as about 15 mm above average. The operational version of the gauge-based Global Historical Climatology Network (GHCN; Peterson and Vose 1996) dataset is somewhat wetter, with an anomaly of about 40 mm, while a new experimental version of GHCN (with five times as many stations) has an anomaly of about 80 mm (implying 2017 was the wettest year in the historical record). Notably, when the blended gauge–satellite GPCP product is adjusted using a new gauge analysis for 2014–present, the anomaly for 2017 increases to about 30 mm, which would be the wettest year in the satellite era. Large areas with above-normal precipitation in 2017 (Plate 2.1i) include northwestern North America, northern Eurasia, interior sub-Saharan Africa, southeastern Asia, the Maritime Continent, and western Australia. Areas with below-normal precipitation include southern Alaska, central Canada, southeastern Brazil, western Europe, eastern Africa, northern India, the Korean peninsula, and eastern Australia (Plate 2.1i). Relative to 2016, aridity was much less pronounced in many areas, particularly Central America, South America, and southern Africa.

According to GPCP, precipitation over the global ocean surface in 2017 was near the long-term average for the satellite era. In the tropics, the annual anomaly pattern (Plate 2.1i) reflects much wetter-than-normal conditions stretching from the eastern Indian Ocean across the Maritime Continent to the western equatorial Pacific Ocean, with much drier-than-normal conditions extending eastward across the rest of the equatorial Pacific. Indeed, the seasonal anomaly patterns during 2017 (not shown) indicate that similar features in the Pacific Ocean/Maritime Continent area existed in varying strengths during

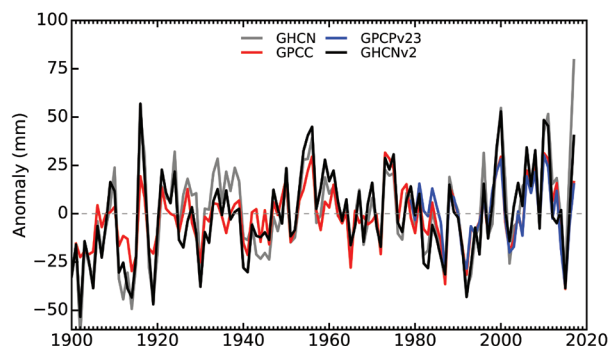


**FIG. 2.22. Globally averaged precipitation anomalies (mm yr<sup>-1</sup>) over land areas relative to the 1961–90 base period (except GPCP v2.3, which is 1981–2000).**

## SIDEBAR 2.1: **LAND SURFACE PRECIPITATION EXTREMES**—M. R. TYE, S. BLENKINSOP, M. DONAT, I. DURRE, AND M. ZIESE

2017 was a mixed year in terms of extreme precipitation, with remarkable tropical and post-tropical cyclone precipitation at one end of the scale and extended droughts at the other (see Sections 2d4, 2d9, respectively). The range of events demonstrates that extreme precipitation is not evenly distributed across the globe (Herold et al. 2015), while anthropogenic climate change has likely increased their probability of occurrence (e.g., Risser and Wehner 2017). Annual precipitation totals were above the 90% percentile in coastal east Asia, western and northern Australia, northeastern Europe, parts of northern North America, Central America, and southeastern South America (Plate 2.1j; see also Section 2d4). The year was also notable for the large proportion of moderate to heavy extreme precipitation (i.e., days with accumulations  $\geq$  90th and 95th percentiles; Zhang et al. 2011) with respect to previous years.

Robust and reliable global datasets for extreme precipitation that include data throughout 2017 are limited, particularly for sub-monthly resolutions. Here we make use of the Global Historical Climatology Network Daily (GHCND; Menne et al. 2012), GHCND-based GHCNEX (Donat et al. 2013a) and GPCC-FirstGuess Daily (Schamm et al. 2013) gridded extremes to calculate the precipitation indices summarized in Table SB2.1. However, near-realtime updates including 2017 are primarily available from North America, Europe, Australia, and parts of Asia for GHCNEX.

The highest daily precipitation totals are typically found as orographically enhanced rainfall in tropical regions,

making only indices such as Rx1day or R95P (Table SB2.1) meaningful for global comparisons. During 2017 some of these regions also experienced anomalously high precipitation events that resulted in significant impacts, such as Rx1day (Plate 2.1k, Online Fig. S2.17) for 31 March–1 April in Colombia (130 mm in Mocoa).

While boreal spring 2017 saw high seasonal precipitation totals across all continents (Section 2d4), individual indices do not reflect the full picture of extremity. For instance, although atmospheric rivers (e.g., Dettinger et al. 2011) were very active along the U.S. West Coast early in the year, Rx1day and Rx5day rank low for that region with respect to climatology (Plate 2.1k). The year as a whole is notable for the moderate extreme indices. That is, the anomalies in total precipitation (PRCPTOT) appear to be attributable more to anomalies in R10mm and/or R20mm than, say, R95P (Plate 2.1j, Fig. SB2.1, Online Fig. S2.18).

Munich Re (2018) summarized 2017 global loss events within four hazard categories. From the meteorological and hydrological events hazard categories, the precipitation induced insured losses from Severe Tropical Cyclone Debbie (27 March–6 April) in eastern Australia and New Zealand, and Hurricane Harvey (25 August–1 September) in Texas and Louisiana are unprecedented. Hurricane Harvey set numerous daily rainfall records at NOAA weather stations throughout the area, with Rx1day exceeding 600mm and Rx5day at almost double previous records (Fig. SB2.2; see online supplemental information; see Sidebar 4.3 for more details on Harvey). Severe Tropical Cyclone Debbie strengthened to a Saf-

**TABLE SB2.1. Extreme precipitation indices from the Expert Team on Climate Change Detection and Indices (ETCCDI).**

Index	Name	Definition	Unit
<b>PRCPTOT</b>	Total annual precipitation	Annual wet day ( $R \geq 1$ mm) precipitation total	mm
<b>Rx1day</b>	Max 1 day precipitation amount	Annual maximum 1 day precipitation	mm
<b>Rx5day</b>	Max 5 day precipitation amount	Annual maximum consecutive 5 day precipitation	mm
<b>R10mm</b>	Number of heavy precipitation days	Annual count when precipitation $\geq 10$ mm	days
<b>R20mm</b>	Number of very heavy precipitation days	Annual count when precipitation $\geq 20$ mm	days
<b>R95P</b>	Very wet days	Annual total precipitation from days $>95$ th percentile of wet days	mm



fir–Simpson category 3 storm before making landfall over the North Queensland coast. While Debbie is considered to be one of the costliest and most deadly cyclones to affect Australia (Insurance Council Australia 2017), associated Rx1day and Rx5day totals have been exceeded

at least three times at several locations since 1918 (Online Fig. S2.19). Other events such as those in South Asia (monsoon rains June–October), Peru (wet season floods January–March), and Sierra Leone (landslides 14 August) were notable for their longevity and/or high human cost.

Further information is available at <http://floodlist.com/?s=2017&submit=>.

Many of the events witnessed in 2017 originated from stationary mesoscale convective systems (MCS). MCSs are organized systems of thunderstorms, larger than individual storms but smaller than extratropical cyclones. They can last for over 12 hours and can rival tropical cyclones for impacts due to their intensity and repetition leading to soil saturation, and they contribute up to \$20 billion (U.S. dollars) economic losses each year (Munich Re 2016). Across the North American Midwest, where the conditions are often suitable for generating these events, it is notable that the pattern of extreme deviations from climatology (negative and positive) for R10mm and R20mm are similar to PRCPTOT. That is, the greatest contributions to the annual total came from more moderate extremes. Many of the flood inducing extremes in 2017 (Brakenridge 2018) appear to be derived from these moderate extremes, suggesting that more attention should be paid to “nuisance events” (i.e., unusual but not so rare that they are unknown within the record; Schroeer and Tye 2018, manuscript submitted to *J. Flood Risk Manage.*). It should be noted that the available data, such as GHCNDEX, are often too coarse to resolve MCSs and may miss these extremes.

Limited availability of in situ high-resolution rainfall observations has confounded long-term assessments of changes in sub-daily extreme precipitation (significant in generating flash floods; Westra et al. 2014). Historical analyses of change have typically been conducted on regional scales using a variety of methods (Online Fig. S2.20) making it difficult to assess the state of the climate and to place notable events in context. However, studies do indicate a tendency towards more intense extremes. A global data collection exercise is underway (Lewis et al. 2018, manuscript submitted to *J. Climate*) under the INTENSE (Intelligent Use of Climate Models for Adaptation to Nonstationary Hydrological

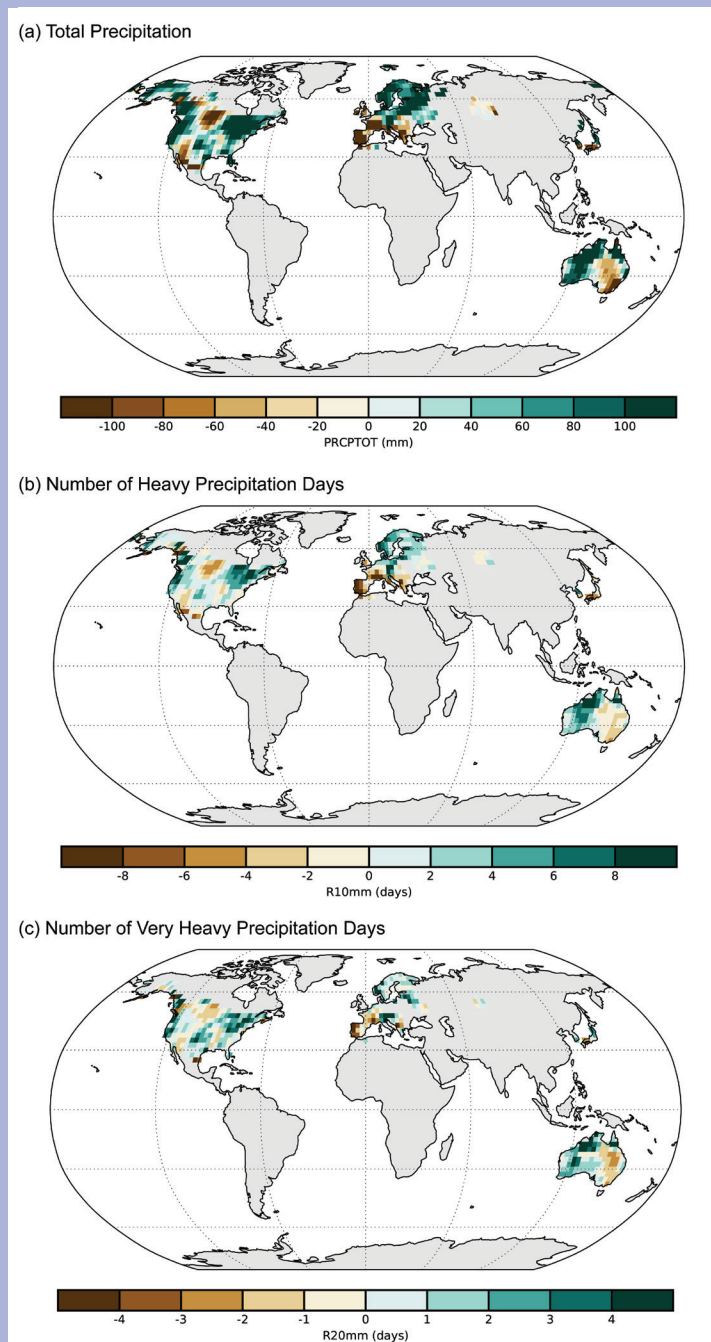


**FIG. SB2.1. 2017 anomalies (1961–90 base period) from GHCNDEX for (a) PRCPTOT (mm), (b) R10mm (days), and (c) R20mm (days).**

Extremes) project (Blenkinsop et al. 2018, manuscript submitted to *Adv. Sci. Res.*) and will result in a quality-controlled sub-daily dataset. This will include the production of comparable sub-daily extreme indices to those in Table SB2.1 to enable the monitoring of these events. New analyses using these data have indicated continental-scale increases in the intensity of hourly rainfall (Barbero et al. 2017; Guerreiro et al. 2018, manuscript submitted to *Nat. Climate Change*). Observational evidence, coupled with that from climate models, suggests that heavy rainfall will

intensify with temperature according to or exceeding the Clausius–Clapeyron (CC) relation (a rate of  $\sim 6\%–7\% \text{ }^{\circ}\text{C}^{-1}$ ) (Trenberth et al. 2003; Pall et al. 2007), although changes in dynamics may lead to regionally higher or lower rates of intensification. Improved quality and global coverage of sub-daily observations will enable a much needed advance in understanding of how local thermodynamics and large-scale circulations interact to generate short-duration intense rainfall (Pfahl et al. 2017).

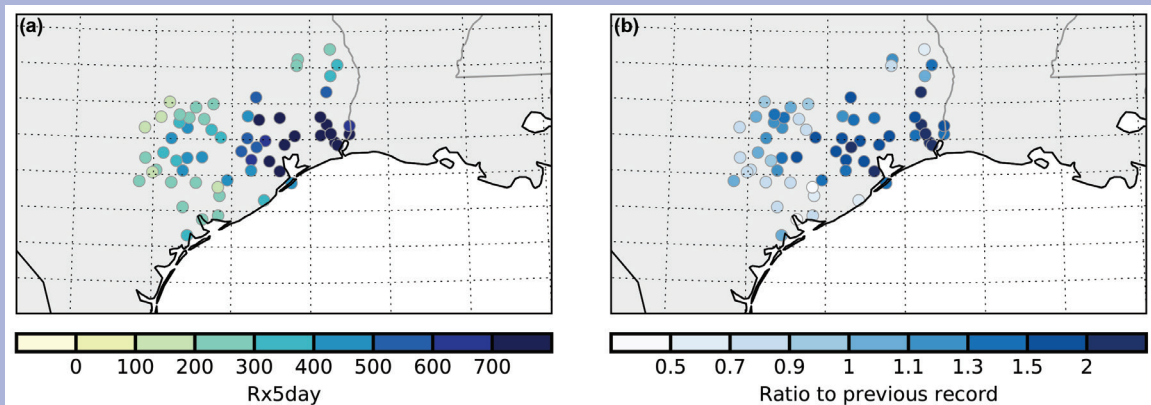


**FIG. SB2.2. (a) Rx5day from GHCNDEX for Hurricane Harvey and (b) ratio of the 2017 value to the previous maximum in the record.**

the entirety of 2017. Large parts of the North Pacific, North Atlantic, South Atlantic, and south Indian Oceans had notable negative anomalies, whereas parts of the South Pacific convergence zone and the equatorial Atlantic Ocean were wetter than normal. A negative anomaly feature across the very southern tip of the African continent was also apparent, where Cape Town, South Africa, experienced its driest year since 1933.

For an assessment of precipitation extremes in 2017, see Sidebar 2.1, and for more detailed discussion on regional precipitation quantities, see Chapter 7.

- 5) CLOUDINESS—M. J. Foster, S. A. Ackerman, K. Bedka, L. Di Girolamo, R. A. Frey, A. K. Heidinger, S. Sun-Mack, C. Phillips, W. P. Menzel, M. Stengel, and G. Zhao

Cloud observations are important for monitoring climate because they modulate energy flow through reflection of incoming solar radiation and absorption of outgoing terrestrial radiation, and they affect global water distribution through storage and precipitation of atmospheric water. Global cloudiness in 2017 decreased incrementally ( $\sim 0.2\%$ ) from that of 2016. This analysis is based on several satellite cloud

records including PATMOS-x/AVHRR (Pathfinder Atmospheres Extended/Advanced Very High Resolution Radiometer; Heidinger et al. 2014), *Aqua* MODIS C6 (Moderate Resolution Imaging Spectroradiometer Collection 6; Ackerman et al. 2008), *CALIPSO* (Cloud-Aerosol Lidar and Infrared Pathfinder Satellite Observation; Winker et al. 2007), CERES (Clouds and the Earth's Radiant Energy System; Minnis et al. 2008; Trepte et al. 2010) *Aqua* MODIS, MISR (Multi-angle Imaging SpectroRadiometer; Di Girolamo et al. 2010), and SatCORPS (satellite cloud and radiative property retrieval system; Minnis et al. 2016). All of these records show a decrease in cloudiness from 2016 to 2017 ranging from 0.1% to 0.34%, depending on the dataset. Figure 2.23 shows global cloudiness from 1981 to present with additional records: HIRS High Cloud (High Resolution Infrared Sounder; Wylie et al. 2005; Menzel et al. 2016), CLOUD\_CCI (Cloud Climate Change Initiative AVHRR-PM v3.0; Stengel et al. 2017), CLARA-A2 (cloud, albedo and radiation dataset; Karlsson et al. 2017), and PATMOS-x/*Aqua* MODIS that do not currently extend through 2017. While there is interannual and inter-record variability in the early part of the record, there is an overall

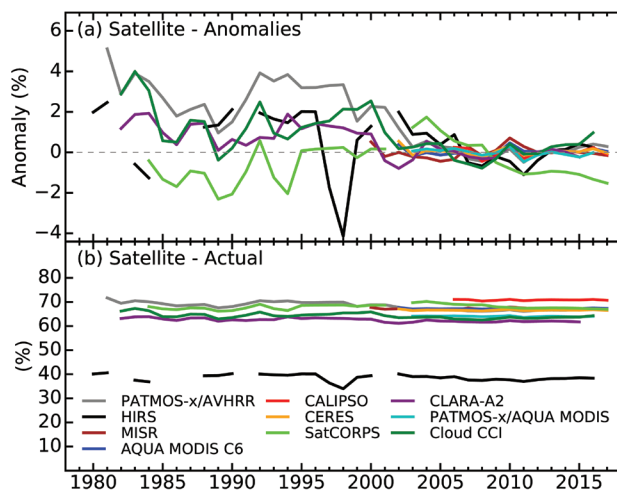


**FIG. 2.23. (a) Annual global cloudiness anomalies (%) for 1981–2017, defined as the annual value minus the mean, derived between 2003 and 2015, a period common to the satellite records excluding CALIPSO, where the entire record was used instead. (b) Annual actual global cloudiness (%). The datasets include PATMOS-x/AVHRR, HIRS High Cloud, MISR, Aqua MODIS C6, CALIPSO, CERES Aqua MODIS, SatCORPS, CLARA-A2, PATMOS-x/Aqua MODIS, and CLOUD\_CCI.**

tendency for convergence after 2000. Much of the convergence can be explained by the use of a common baseline of 2003–15, though it does not explain interannual variability. Online Figure S2.13 plots the records that extend back before 2000 and removes the common baseline, which results in the spread among the records to be similar throughout. Figure 2.23b shows absolute cloudiness and the overall interannual stability of these records. It also shows there is no consensus on global cloudiness trends. We should note the HIRS record is noticeably lower because it focuses on detecting high cloud. It is included here because comparison with anomalies is still valuable, and it is the only non-AVHRR record we have that extends back into the 80s and 90s.

Although global-scale events such as ENSO and volcanic eruptions may be responsible for some early-record interannual variability, it is likely that much of the interannual and most of the inter-record variability relates to the combinations of satellites and sensors used in the records. Four of the records that extend back into the 1980s—PATMOS-x/AVHRR, SatCORPS, CLARA-A2, and CLOUD\_CCI—are derived from the AVHRR sensor flown on NOAA POES. The morning satellites flown in the 1980s and 1990s lack a second infrared channel and have a greater tendency to drift from their original orbit thereby shifting the local overpass time and potentially cre-

ating an aliasing effect. Therefore, when generating a cloud data product, the selection of which satellite records to include is significant. SatCORPS, CLARA-A2, and CLOUD\_CCI are derived from afternoon satellites, while PATMOS-x/AVHRR uses afternoon and morning satellites. PATMOS-x, SatCORPS, and CLARA-A2 have a diurnal correction applied (Foster and Heidinger 2013). This correction usually takes the form of a cloudiness adjustment to a single local overpass time based on a linear regression. Several international collaborative efforts exist with the goal of better characterizing these differences and addressing some of these issues, including the Global Energy Water Cycle Experiment (GEWEX) Cloud Climatology Assessment (Stubenrauch et al. 2013), the International Clouds Working Group (ICWG; formerly the EUMETSAT Cloud Retrieval Evaluation Workshops; Wu et al. 2017), the WMO Sustained and Coordinated Processing of Environmental Satellite data for Climate Monitoring (SCOPE-CM; Kearns and Doutriaux-Boucher 2015) AVHRR Climate Initiative, and the WMO Global Space-based Inter-Calibration System (GSICS).

There were a few noteworthy cloudiness anomalies (those found to be significant at the 5% level) in 2017 relative to the PATMOS-x/AVHRR base period of 1981–2010. Almost all of these anomalies were less cloudy than average with two exceptions of cloudier-than-average areas over the Arctic Ocean. Global cloudiness patterns frequently correspond with large-scale circulation patterns. SST and low-level wind anomalies between the central equatorial Pacific and Indonesia characteristic of ENSO drive convection, which, in turn, drives global cloudiness

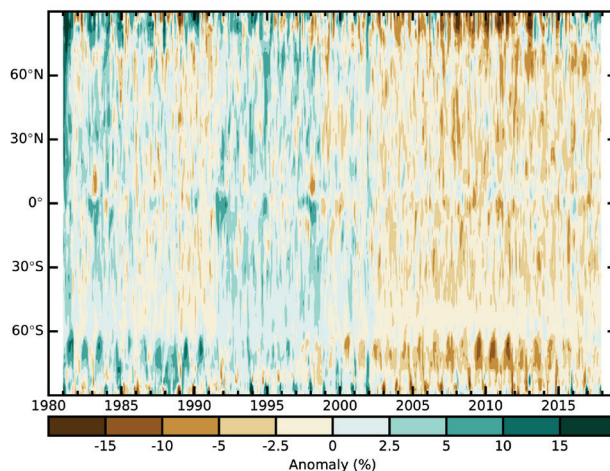


**FIG. 2.24. Annual global cloudiness anomalies (%; relative to 1981–2010) from the PATMOS-x/AVHRR record calculated using the same method as Fig. 2.23 but zonally for each degree latitude.**



distribution. El Niño events often correspond with cloudier conditions over the central equatorial and southeastern Pacific, while La Niña events correspond with less cloudy conditions. This can be seen in Fig. 2.24 where cloudiness anomalies are consistent with phases of ENSO in the PATMOS-x/AVHRR record. In 2017 the ENSO index was largely neutral, beginning and ending the year with weak La Niña conditions. Seasonal cloudiness reflects this evolution (Online Fig. S2.14). Due to this pattern, Plate 2.1p shows cloudiness anomaly patterns between the western Pacific and Indonesia generally consistent with weak La Niña conditions but lacking significance at the 5% level, with the exception of small areas off the west coasts of Mexico and Chile. The Indian Ocean dipole (IOD) is an interannual weather pattern that affects the tropical Indian Ocean. 2017 saw sporadic negative phases of the IOD at the beginning and end of the year, which typically correspond with cooler sea surface temperatures in the western Indian Ocean that likely contributed to below-average cloudiness seen in the northern and southwestern parts of the Indian Ocean. Continental below-average cloudiness frequently corresponds with warm and dry conditions as experienced in Alaska, western Europe, and large portions of Russia and China.

#### 6) RIVER DISCHARGE AND RUNOFF—H. Kim

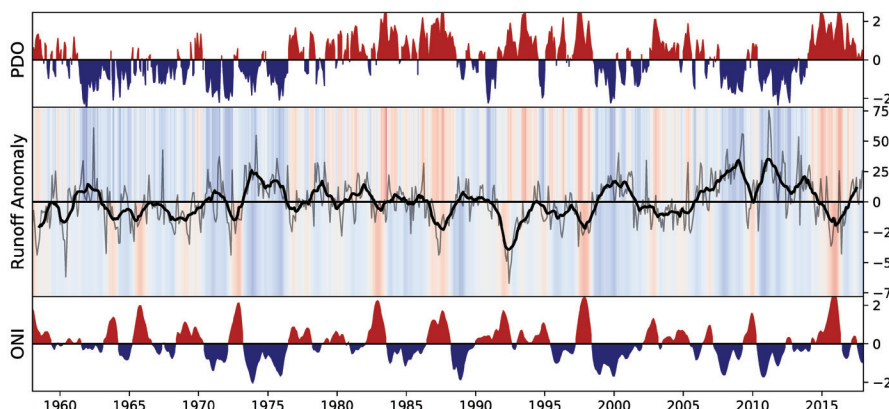
After evapotranspiration, induced by the available energy at the land surface and from moisture uptake from the root zone by the photosynthesis of vegetation, the remaining precipitated water is transported by gravity. The water eventually forms narrow and meandering rivers, transporting it to the oceans. Freshwater in the channel network is the first source

for water resources required by humans and their activities and industries.

Sixty years (1958–2017) of global runoff and river discharge were estimated by off-line land surface simulations on the ensemble land surface estimator (ELSE; Kim et al. 2009). The simulation configuration remains the same as in the previous report (e.g., Kim 2017), and atmospheric boundary conditions were extended by combining the Japanese global atmospheric reanalysis (JRA-55; Kobayashi et al. 2015) and the Global Precipitation Climatology Centre (GPCC) Monitoring Product version 5 (Schneider et al. 2015).

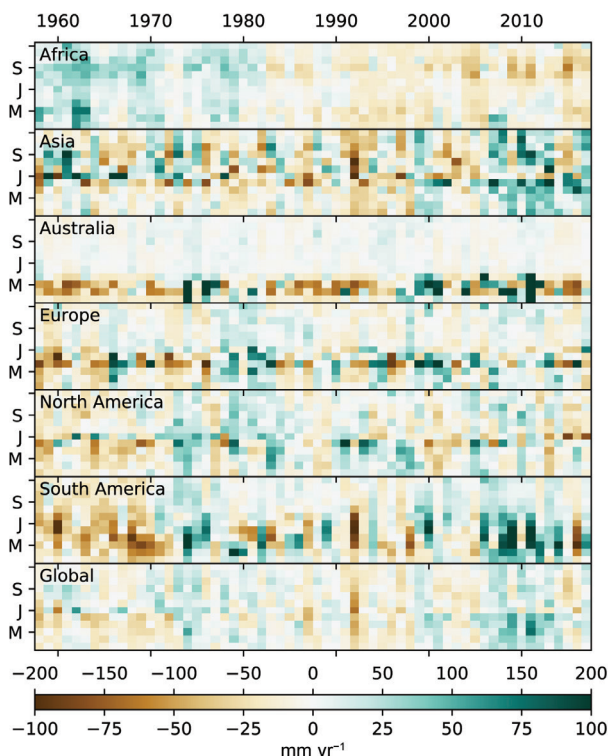
In 2017, the global distributions of runoff (Plate 2.1l) and discharge (Plate 2.1m) anomalies show that large areas of South America, Southeast Asia, eastern Europe, and western and eastern Siberia were under significantly wet conditions. In contrast, Africa, central Siberia, India, the eastern United States, and eastern Europe including the Mediterranean were under drier conditions compared to their normal climate. Among these, the African, European, and Siberian regions tended to experience a similar state as the previous year. Long-term variability of global runoff is shown with the El Niño–Southern Oscillation (ENSO) and the Pacific decadal oscillation (PDO; Mantua et al. 1997) in Fig. 2.25. It has been found that the La Niña phase of ENSO and a neutral phase of PDO result in global runoff that is weakly wetter than the long-term average. The ENSO and PDO indices explain approximately 50% of the variability of the global runoff (Kim 2017). After a strong positive phase of the 2015/16 ENSO, the weak La Niña conditions in 2017 and the relatively weak positive phase of the PDO led to slightly wetter conditions.

Figure 2.26 indicates a monthly time series



**FIG. 2.25. Interannual variability of ONI (Oceanic Niño Index, lower), PDO (upper), and global runoff (middle; mm; thick line is 12-month moving average). ONI and PDO are shaded red (positive phase) or blue (negative phase). Shading above and below the zero-line of global runoff is proportional to PDO and ONI, respectively.**

deviation (i.e., excess or deficiency) runoff from the long-term mean of seasonal variations globally and on each continent. South America shows the typical seasonal variation of a wet year that has excessive runoff in the earlier season (i.e., February–April) compared to the wet season in dry years (i.e., May–July). The Amazon River is wetter than normal except in a few sub-basins such as the Rio Madeira, the Rio Tocantins, and the Rio Araguaia. The Rio Parana and the Rio Sao



**FIG. 2.26. Interannual variability of global and continental runoff ( $\text{mm yr}^{-1}$ ) for 1958–2017. The x- and y-axes correspond to annual and seasonal variations, respectively. Europe and South America refer to the upper scale of the color bar, and the others refer to the lower scale.**

Francisco maintained the same wet and dry conditions as in the previous year, respectively. In Asia, the dry condition of high latitude regions in 2016 was alleviated slightly. The state of the Ob and Kolyma Rivers (Siberia) shifted from dry to wet. However, the Yenisey River still remained dry and the Lena River took on dry conditions. Over mid- and low latitudes in Asia, many regions were wetter than normal (e.g., the Yangtze, Huang He, Chao Phraya, Mekong Rivers), while Amur and Ganges–Brahmaputra were drier than normal. Europe showed a considerable deviation from the climatological seasonality, with considerably drier conditions during the early half of the year; the phase shifted radically into a wet-year condition beginning in June. North America was in a weak dry condition, and most of the rivers in the region, including the Mississippi (U.S.) and Mackenzie (Canada), were facing a water deficit. Africa has been experiencing a persistent dry condition since the 1980s, and Australia has had near-neutral to dry conditions after a historic wet year in 2011.

## 7) GROUNDWATER AND TERRESTRIAL WATER STORAGE—

M. Rodell, D. N. Wiese, B. Li, and J. S. Famiglietti

Precipitation that falls on the land and does not immediately evaporate or run off becomes terrestrial water storage (TWS; the sum of groundwater, soil moisture, surface water, snow, and ice). Groundwater and total TWS exhibit larger variations on multiannual timescales than the near-surface TWS components (Li et al. 2015). Both are difficult to monitor using in situ observations, but from 2002 to 2017 the Gravity Recovery and Climate Experiment (GRACE; Tapley et al. 2004) satellite mission mapped TWS variations on a monthly basis at regional scales, worldwide. During the last few years of the mission, on-board battery issues caused frequent, multimonth measurement gaps, and no TWS data are available past June 2017. To create the 2016–2017 difference map (Plate 2.1h) output from a GRACE data assimilating land surface model (Li et al. 2018, manuscript submitted to *Water Resour. Res.*) was used.

Changes in TWS between 2016 and 2017, plotted as equivalent heights of water in Plate 2.1h, integrate the effects of other hydroclimatic conditions (see Plates 2.1i, n, o, p, t, and v). All continents experienced a somewhat even mix of TWS increases and decreases, with many reversals. The Amazon basin recovered from huge, widespread water losses in 2016, with large gains in the eastern part of the basin. However, southern Brazil endured significant TWS reduction. Across the Atlantic the reverse scenario occurred—with large-scale, deep drying in central and eastern Africa and wetting to the south. Southern Europe suffered serious drought-related water losses, most notably in Portugal, while northern Europe was normal to wet. Northwestern Australia regained water lost in the

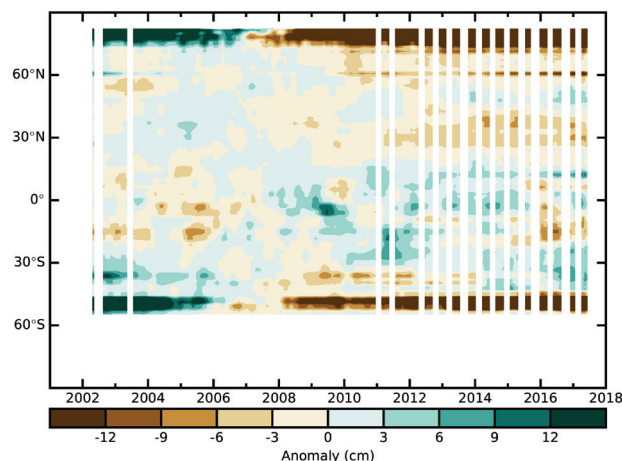


**FIG. 2.27. Zonal mean terrestrial water storage anomalies (cm, equivalent height of water, 2005–10 base period) from GRACE. White areas indicate months when data were unavailable.**

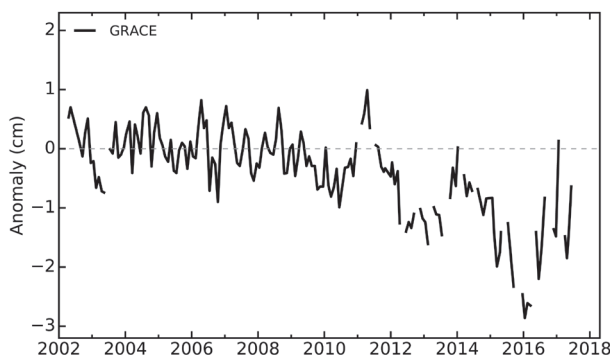


**FIG. 2.28. Global average terrestrial water storage anomalies from GRACE (cm, equivalent height of water, 2005–10 base period).**

previous year, while conditions in the southeast were generally dry. TWS changes in North America were also mixed. The heavy winter rains that led to flooding and mudslides in central and southern California aided in its recovery from long-term drought. Much of the eastern and mountain regions of the U.S. also gained TWS, while Canada and Mexico were generally dry, including drought in British Columbia that contributed to its most extensive wildfire season on record (see Section 7b1). Central and southern Asia exhibited patchy drying, while heavy rains in the Indochina peninsula increased TWS dramatically. Eastern Siberia also was wetter than normal. While GRACE has measured significant reductions in TWS in Antarctica, Greenland, southern coastal Alaska, and Patagonia (the latter two are apparent at 60°N and 46°–55°S, respectively, in Fig. 2.27) due to ongoing ice sheet and glacier ablation, these processes are not properly simulated by the model and the regions must be ignored in Plate 2.1h.

Figures 2.27 and 2.28 plot zonal mean and global mean deseasonalized monthly TWS anomalies from GRACE (excluding Greenland and Antarctica). Reduced dryness in the southern tropics (Fig. 2.27) is associated with the TWS increases in the Amazon, southern Africa, and northwestern Australia. While only five months of GRACE data are plotted in Fig. 2.28, GRACE data assimilation output (not shown) indicate that recovery from the January 2016 global TWS minimum continued in 2017, owing largely to the increases in the Amazon.

**8) SOIL MOISTURE**—W. A. Dorigo, T. Scanlon, A. Gruber, R. van der Schalie, C. Reimer, S. Hahn, C. Paulik, W. Wagner, and R. A. M. de Jeu

The ESA Climate Change Initiative soil moisture (ESA CCI SM) product combines observations from a large number of historical and present-day passive and active microwave instruments in a synergistic

way (Dorigo et al. 2017b; Gruber et al. 2017; Liu et al. 2012). The latest dataset version (COMBINED v04.3) merges 11 different sensors between late 1978 and December 2017 into a single harmonized long-term dataset with reduced uncertainties and fewer data gaps compared to the single sensor products. The dataset has been validated against a large number of land surface models and in situ datasets used for a wide range of applications (Dorigo et al. 2017b). Based on the ESA CCI SM the yearly and monthly anomalies are computed here with respect to a 1991–2016 climatology.

For several regions, spatial soil moisture anomaly patterns in 2017 (Plate 2.1g) were remarkably drier or wetter than normal. While after several dry years in a row (Blunden and Arndt 2017) soil moisture conditions in the northeast of South Africa were partly alleviated in 2017, drought conditions in the region around Cape Town intensified in the course of the year (Online Fig. S2.15; see Section 7e4). Dry soil moisture conditions already observed in 2016 in the Greater Horn of Africa (Blunden and Arndt 2017) persisted into 2017 and reportedly led to a displacement of more than 1 million people, according to a report from the World Meteorological Organization. On the other hand, soil moisture contents were higher than normal for most other parts of southern Africa, particularly during the first half of the year, and contributed to severe flooding, for example, in Botswana. Very dry soils were also observed in Morocco and southern Europe. Italy suffered particularly severe rainfall deficits and had its driest January–September period on record.

While soil moisture conditions in most parts of Brazil were around average, some parts of northeastern Brazil showed strong anomalous negative soil moisture conditions for the sixth consecutive year [see previous *State of the Climate* reports, e.g., Dorigo et al. (2017a)]. Wet conditions were observed for southern South America and the west coast of Peru, which strongly contrasts with the anomalously dry conditions that were observed in this region in 2016 (Dorigo et al. 2017a). Also, most of the southern and eastern United States were much wetter than normal. In particular, August was very wet (Online Fig. S2.15) with Hurricane Harvey making landfall in southern Texas. On the other hand, the Canadian Prairies and adjacent northern border areas of the United States were anomalously dry, mainly during the summer months (Online Fig. S2.15).

In 2017, soils in large parts of Southeast Asia were much wetter than normal. The monthly anomaly images reveal that this pattern persisted throughout



the year (Online Fig. S2.15). A much wetter-than-average start to the year in many parts of western and northern Australia (Online Fig. S2.15) resulted in net average soil moisture conditions in 2017 that were wetter than usual for these areas. At the same time, most parts of eastern Australia were drier than average, reflecting precipitation amounts that were well below average (see Section 7h3).

The year 2017 was mostly dominated by a neutral state of ENSO (see Section 4b). ENSO anomalies are known to potentially cause continent-wide deviations in terrestrial water storages (Bauer-Marschallinger

et al. 2013; Boening et al. 2012; Dorigo et al. 2017b; Miralles et al. 2014). Although soil moisture conditions in the Southern Hemisphere were on average wetter than normal, deviations were far from being as pronounced as in 2000 or 2010/2011 (Figs. 2.29 and 2.30), which were episodes associated with strong La Niña events. In the Northern Hemisphere, average soil moisture was close to normal in 2017 (Fig. 2.30).

No evident large-scale long-term global soil moisture trends can be observed (Fig. 2.30). However, this does not exclude the existence of long-term trends at the regional or local scale (An et al. 2016; Rahmani et al. 2016; Wang et al. 2016). However, anomalies and trends in average global soil moisture should be treated with caution, owing to dataset properties changing over time and the inability to observe beneath dense vegetation, mountain areas, or frozen or snow-covered soils (cf. gray regions in Plate 2.1g and Online Fig. S2.15).

9) DROUGHT—I. J. Osborn, J. Barichivich, I. Harris, G. van der Schrier, and P. D. Jones

Hydrological drought results from a period of abnormally low precipitation, sometimes exacerbated by additional evapotranspiration (ET), and its occurrence can be apparent in reduced river discharge, soil moisture, and/or groundwater storage, depending on season and duration of the event. Here, an estimate of drought called the self-calibrating Palmer drought severity index (scPDSI; Wells et al. 2004; van der Schrier et al. 2013) is presented, using precipitation and Penman–Monteith potential ET from an early update of the CRU TS 3.26 dataset (I. Harris et al. 2014). Moisture categories are calibrated over the complete 1901–2017 period to ensure that “extreme” droughts and pluvials relate to events that do not oc-

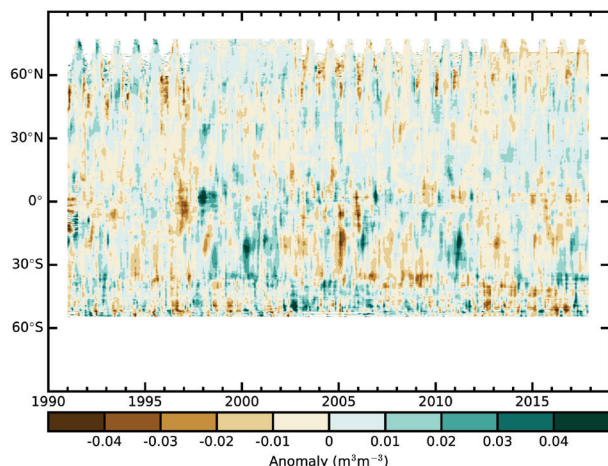


**FIG. 2.29.** Time–latitude diagram of surface soil moisture anomalies ( $\text{m}^3 \text{m}^{-3}$ , base period: 1991–2016). Data were masked as missing where retrievals are either not possible or of low quality (dense forests, frozen soil, snow, ice, etc.). (Source: ESA CCI Soil Moisture.)

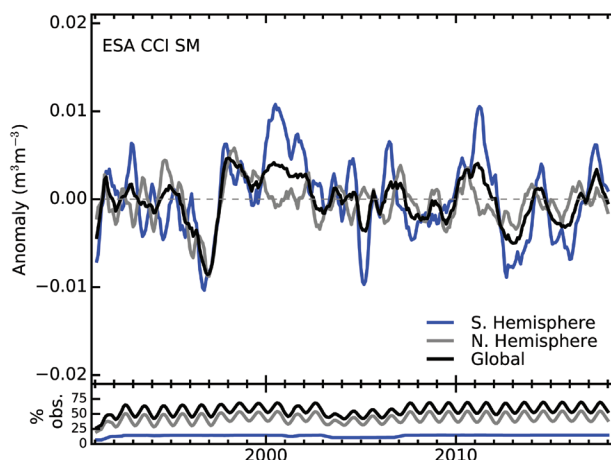


**FIG. 2.30.** Time series of average global surface soil moisture anomalies for 1991–2017 ( $\text{m}^3 \text{m}^{-3}$ , base period: 1991–2016). Data were masked as missing where retrievals were either not possible or of low quality (dense forests, frozen soil, snow, ice, etc.). (Source: ESA CCI Soil Moisture.)

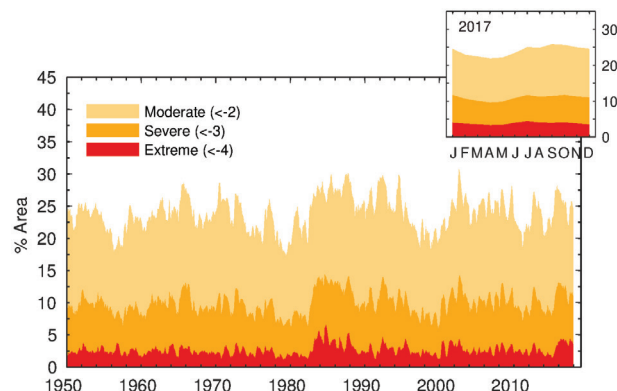


**FIG. 2.31.** Percentage of global land area (excluding ice sheets and deserts) with scPDSI indicating moderate (<-2), severe (<-3), and extreme (<-4) drought for each month of 1950–2017. Inset: each month of 2017.

cur more frequently than in approximately 2% of the months. This affects direct comparison with other hydrological cycle variables in Plate 2.1s that use a different base period.

After a notable peak in the overall area of drought across the globe in the second half of 2015 and all of 2016 (Osborn et al. 2017), drought area declined sharply by early 2017 (Fig. 2.31) before increasing to above average once more (though still below the 2016 area). Extreme drought conditions affected at least 3% of global land area in every month of 2017, which was matched only by 1984, 1985, and 2016, but the geographical extents of moderate and severe droughts were not so unusual. The area where scPDSI indicates moderate or worse drought began at 24% in January, fell below 22% by April, before rising to around 25% in the latter months of 2017. Altogether, three months had moderate or worse drought affecting more than 25% of the global land area, which has been matched or exceeded in 34 other years since 1950. The area of severe plus extreme droughts exceeded 10% for ten months during 2016, which has been matched or exceeded in 12 other years since 1950. The 2017 values should be interpreted cautiously because they may be modified by additional observations that will become available in due course. Drought area is just one of several ways to measure drought conditions; for example, Heim (2017) shows that area-integrated drought severity or duration yields different rankings for the major droughts of the 20th and 21st centuries over the contiguous United States since 1900.

Extensive severe or extreme droughts affected all continents except North America during 2017 (Plate 2.1s). Starting in the Western Hemisphere, persistent moderate-to-severe drought conditions affecting

south-central Chile (Garreaud et al. 2017) continued for the eighth consecutive year, though the geographic extent of extreme drought decreased with a slight increase in winter rainfall. Notably, severe drought in the semiarid northeastern Brazil (Jiménez-Muñoz et al. 2016) continued in 2017 without much change in intensity and extent (Fig. 2.32). Moderate, or occasionally severe, drought was present across the Northern Hemisphere part of the South American continent (Plate 2.1s) though its intensity had eased compared with 2016 in most areas (Fig. 2.32).

Many coastal countries in Africa experienced drought in 2017, with the exception of some in East Africa (see Section 7e3). These droughts intensified compared with 2016 especially in southern Madagascar and the Western Cape of South Africa, the latter contributing to water supply restrictions in Cape Town in early 2018 (Le Page 2018). The partial easing of drought farther north, including in the Zambezi basin, is important given the increasing concentration of hydropower in the region that increases the risk of concurrent drought-related disruption to electricity production (Conway et al. 2017). Conditions were drier in 2017 than in 2016 in a band across Eurasia around 45°N (Fig. 2.32). This exacerbated drought in western and southern Europe, resulting in many impacts, including reduced agricultural yields and hydroelectric power production in the Balkans and Albania, and wildfire and hydrological impacts in Iberia.

Parts of the Middle East remained in drought, and particularly severe drought developed in the southwestern peninsula of India (especially Kerala) during 2017. Farther north in Asia, severe drought conditions were present in the Krasnoyarsk region of Russia, extending south to northern China. The severe drought in mainland Southeast Asia in 2016 was ended by much wetter conditions during 2017 (Plate 2.1s and Fig. 2.32). Much of Australia was drier than normal during 2017, with severe drought most notable in Tasmania.

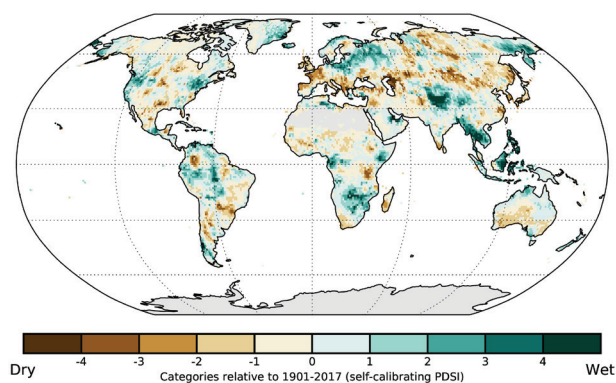


**FIG. 2.32. Change in drought (mean scPDSI) from 2016 to 2017. Increases in drought severity are indicated by negative values (brown), decreases by positive values (green). No calculation is made where a drought index is meaningless (gray areas: ice sheets or deserts with approximately zero mean precipitation).**

**10) LAND EVAPORATION—D. G. Miralles, B. Martens, H. E. Beck, A. J. Dolman, C. Jiménez, M. F. McCabe, and E. F. Wood**

Evaporation, the return flux of water from terrestrial ecosystems to the atmosphere, modulates regional energy and water balances and affects precipitation, both locally and in remote locations. Estimating this variable in near real-time is important for both agricultural and hydrological management, while being able to monitor long-term trends enables the identification of climatological impacts

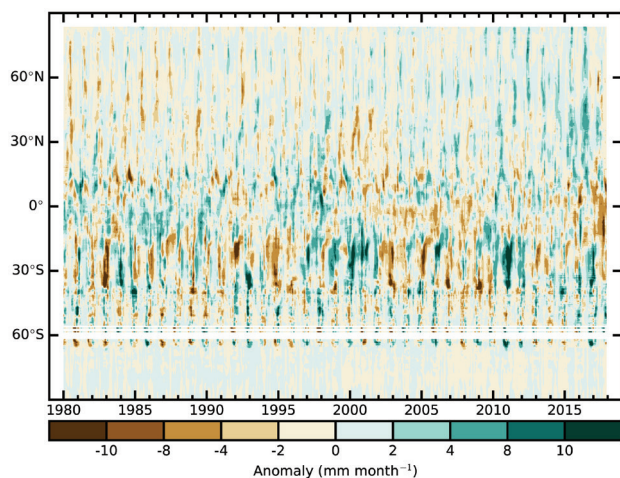
on the global hydrosphere. Despite promising advances in the global sensing of evaporation from space (e.g., Mallick et al. 2016; McCabe et al. 2017b), and a potentially bright future as novel sensors are launched into space (McCabe et al. 2017a; Fisher et al. 2017), evaporation remains an elusive variable: in situ measurements are scarce and satellites can only sense it indirectly. As such, models that combine the satellite-observed environmental and climatic drivers of the flux are often applied to yield global evaporation estimates (Wang and Dickinson 2012). Ongoing efforts aim to reduce product latency and improve spatial resolution, which is essential for applications such as drought monitoring, seasonal extreme forecasting, or irrigation management (Ghilain et al. 2011; Anderson et al. 2011; Mu et al. 2013; McCabe et al. 2017a). The results shown here reflect recent simulations of the Global Land Evaporation Amsterdam Model (GLEAM; Miralles et al. 2011) version v3.2a by Martens et al. (2017). While GLEAM was not intentionally designed with an operational intent, the long-term record is updated to near real-time on an annual basis.

The geographical patterns of evaporation anomalies shown in Plate 2.1t resemble those from El Niño years (see Miralles et al. 2014), yet the ENSO condition in 2017 was neutral on average. Consequently, regional negative anomalies coincide with those in 2016: eastern South America, Amazonia, southern Africa, the Horn of Africa, and India (Plate 2.1t). In addition, other regions such as central-eastern Australia and Central America also experienced low values. A closer look at these patterns indicates that evaporation was below normal in most of the tropics during the second half of the year (Fig. 2.33). In

wet tropics this is typically associated with negative anomalies of incoming radiation (due to cloudy conditions, for example), while in dry tropics it reflects an abnormally low supply of rainfall (Miralles et al. 2011). As such, the low evaporation in the semiarid eastern South America likely relates to the drought that started in 2011, intensified in 2012, and persisted into 2017 (Brito et al. 2018). These conditions were particularly intense in the Caatinga shrubland ecosystems of Brazil. In fact, the strong anomaly in evaporation, shown in Fig. 2.33 around 20°S in the second half of the year, possibly relates to the shortage in plant-available water in this region. Likewise, the negative anomaly in Amazonia, shown in Plate 2.1t, persisted throughout the year, reflecting the impact of the meteorological drought that started in 2015, and was driven by the strong El Niño (Jiménez-Muñoz et al. 2016). The legacy of such events on rainforest ecosystem functioning is known to extend over prolonged periods of time (Zemp et al. 2017).

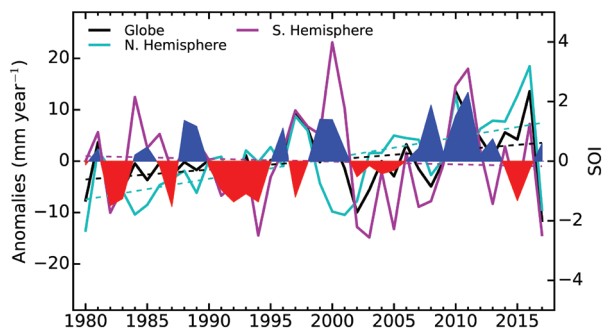
The spatial patterns found in Africa also relate to anomalies in the supply of water to a large extent. Negative anomalies in the Sahel region and Horn of Africa can be attributed to below-average rainfall (Mpelasoka et al. 2018), particularly during the second half of the year. A low water supply also explains the negative anomaly in the Congo basin. While the Congo rainforest is thought to be primarily energy limited, recent studies have shown evidence of ecosystem water limitation (Zhou et al. 2014). Furthermore, the flux of interception loss, i.e., the vaporization of the rainfall captured by the leaves and branches of plants, constitutes a large fraction of the evaporation in the Congo region (Miralles et al. 2010). Conversely, the positive anomaly in the Kalahari Desert (Plate 2.1t) relates to above-average rainfall in January and February, which was followed by a positive anomaly in the atmospheric demand for water in March (Section 2f). Finally, in the absence of particularly strong anomalies in water supply in North America, the positive anomaly in evaporation over the U.S. likely relates to the abnormally high temperatures during the first months of 2017 (see Section 7b2).

Figure 2.34 shows the multiannual (1980–2017) variability in terrestrial evaporation derived from GLEAM v3.2a (Martens et al. 2017). A linear trend of approximately  $0.3 \text{ mm yr}^{-1}$  ( $p = 0.002$ ) for the entire continental surfaces is obtained. While the year-to-year variability is mostly dictated by the variability in the Southern Hemisphere—and particularly affected by the signature of ENSO (Miralles et al. 2014)—the multidecadal trend detected by GLEAM relates almost exclusively to the dynamics of evaporation in the



**FIG. 2.33. Zonal mean terrestrial evaporation anomalies ( $\text{mm month}^{-1}$ ; relative to 1980–2017). (Source: GLEAM.)**





**FIG. 2.34.** Land evaporation anomaly ( $\text{mm yr}^{-1}$ ; 1980–2017 base period) for the NH, SH, and the entire globe (blue, purple, and black solid lines, respectively). Linear trends in evaporation (dashed lines) and the SOI from NOAA (right axis, shaded area) are also shown. (Source: GLEAM.)

Northern Hemisphere. This trend is qualitatively and quantitatively in agreement with Clausius–Clapeyron expectations in a warming atmosphere (Miralles et al. 2014; Brutsaert 2017). The global average terrestrial evaporation in 2017 was slightly below this trend and close to the 1980–2016 mean (Fig. 2.34). Notwithstanding the novel insights made available from remote platforms, trends in satellite-based evaporation should be interpreted with care, and the weighted use of multiple retrieval approaches is usually recommended (Miralles et al. 2016; McCabe et al. 2016). Unfortunately, as of today, algorithms dedicated to estimating evaporation using satellite observations at global scales are mostly intended for research applications and are not regularly updated in near-real time (Fisher et al. 2017).

### e. Atmospheric circulation

#### 1) MEAN SEA LEVEL PRESSURE AND RELATED MODES OF VARIABILITY—R. Allan and C. K. Folland

Overviews of the most recent El Niño have been made in papers such as L’Heureux et al. (2017), but the protracted nature of the El Niño from 2014 to 2016 should also be noted (Allan and D’Arrigo 1999; Allan et al. 2018, manuscript submitted to *Atmosphere*). The climate system exhibited weak La Niña (positive SOI) to neutral conditions follow-

ing the 2014–16 episode. ENSO, arguably the most globally impactful mode of variability, encompasses a family of events and episodes. Individually, these exhibit wide-ranging effects across the Indo-Pacific region, with teleconnections to higher latitudes in both hemispheres (Capotondi et al. 2015; C. Wang et al. 2017). The sea level pressure derived Southern Oscillation index (SOI; Allan et al. 1996; Kaplan 2011) was primarily positive (the phase typically associated with La Niña conditions) from mid-2016 through the end of 2017 (Fig. 2.35). Nevertheless, the immediate impacts of the 2014–16 El Niño episode have lingered in the eastern Australian region, where its influence was particularly profound (Allan and Folland 2017). This has taken the form of persistent above-average eastern Australian SST anomalies from the Coral Sea southwards via major extensions of the East Australian Current into the Tasman Sea region from 2014 through 2017 (Australian Bureau of Meteorology 2017; Oliver et al. 2017). Historically, periods of persistent drought (widespread flooding) in this region have been strongly amplified by protracted El Niño (La Niña) episodes (Murphy and Ribbe 2004; Allan et al. 2018, manuscript submitted to *Atmosphere*).

Mean sea level pressure (MSLP) can also be used to derive indices of many regional modes of variability that drive significant weather and climate events

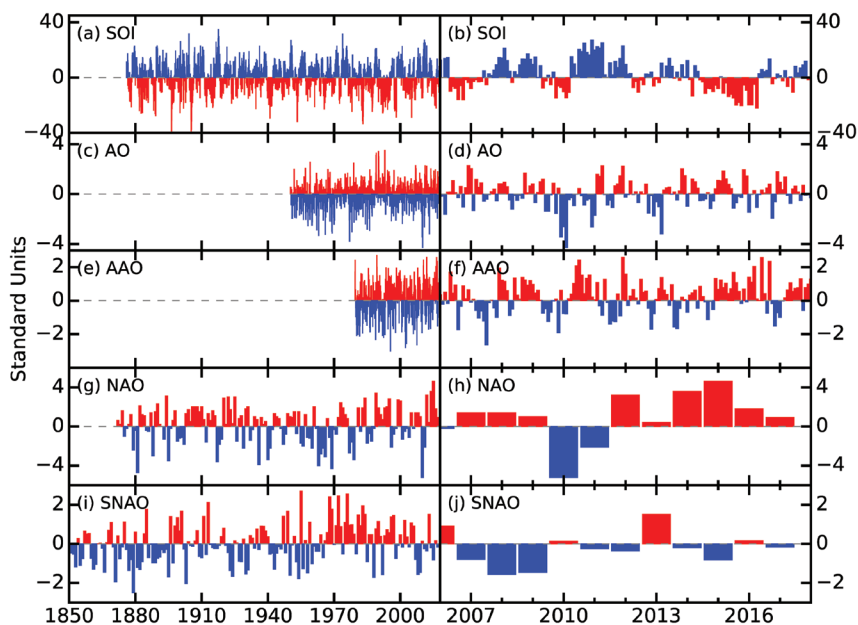


**FIG. 2.35.** Time series for modes of variability described using sea level pressure for the (left) complete period of record and (right) 2006–17. (a),(b) SOI (provided by the Australian Bureau of Meteorology); (c),(d) AO (NCEP Climate Prediction Center); (e),(f) AAO (NCEP Climate Prediction Center); (g),(h) winter (Dec–Feb) NAO average (NCAR; presented for winter at the beginning of each year so winter 2017/18 is not shown); (i),(j) summer (Jul–Aug) SNAO average (Folland et al. 2009).

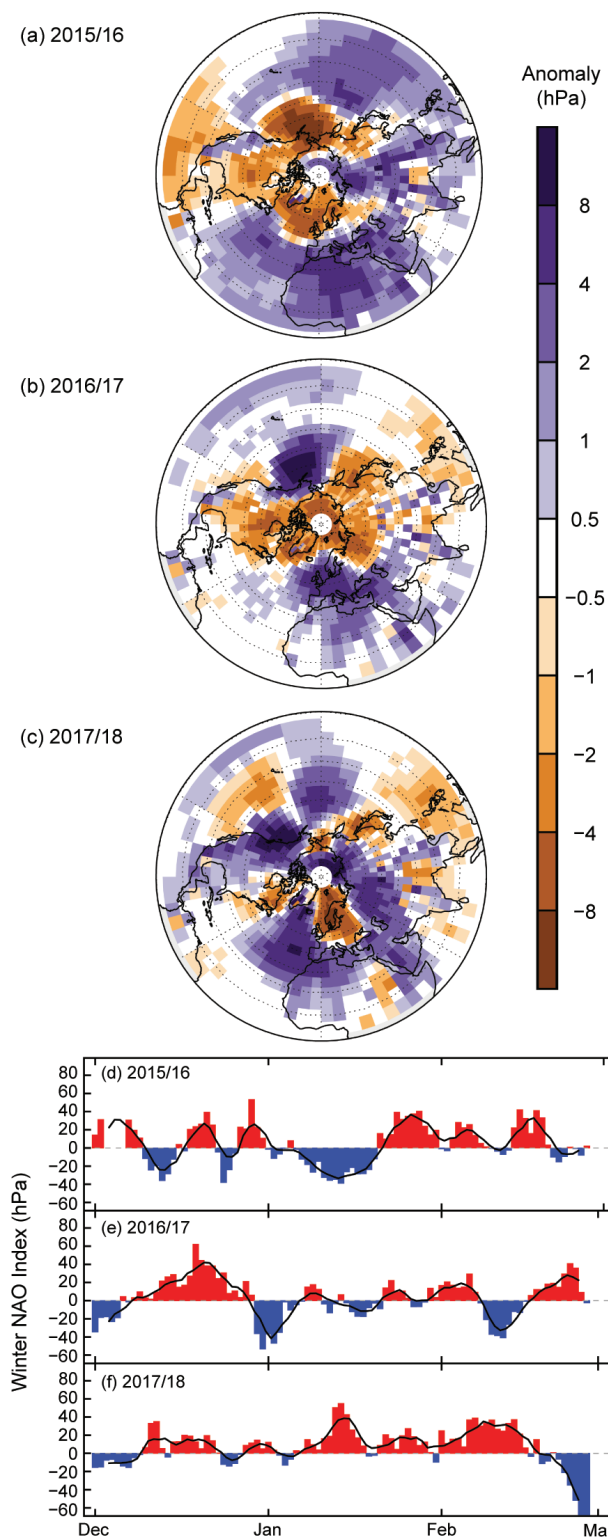
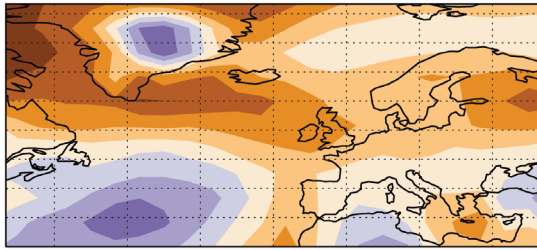


**FIG. 2.36.** Boreal winter sea level pressure anomalies (hPa; 1981–2010 base period) averaged over Dec–Feb for (a) 2015/16, (b) 2016/17, and (c) 2017/18. NAO daily time series (hPa) for winter (d) 2015/16, (e) 2016/17, and (f) 2017/18. The 5-day running mean is shown by the solid black line. The data are from HadSLP2r (Allan and Ansell 2006).

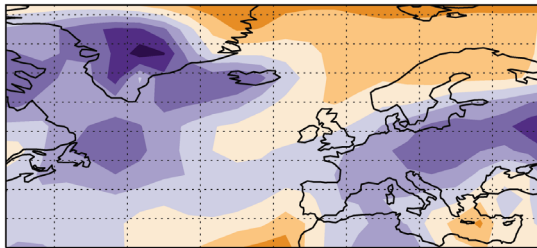
(Kaplan 2011): the Arctic Oscillation (AO); North Atlantic Oscillation (NAO); summer NAO (SNAO); and the Antarctic Oscillation (AAO) (Fig. 2.35). In the Northern Hemisphere, the last six winters have displayed broadly positive NAO conditions but a diverse range of circulation patterns. During the early winter of 2015/16 the NAO oscillated between phases, with a deep trough over the North Atlantic leading to an enhanced jet stream that directed a series of extratropical cyclones toward northern Ireland and Scotland–northern England (Fig. 2.36). By the mid-to-latter part of the 2015/16 winter the pattern had changed, with the NAO swinging from slightly negative in January 2016 to positive in February 2016 (Allan and Folland 2017). The 2016/17 boreal winter was marked by an increasingly positive NAO through mid-December 2016, temporarily negative NAO values around the start of 2017, and then a fluctuation between phases for the rest of January (Fig. 2.36; Allan and Folland 2017). During the 2017/18 boreal winter, the NAO has been mainly positive (Fig. 2.36). As a consequence, temperatures in Europe were mild to warm, and the region experienced its fifth warmest year on record, while Portugal in particular was strongly impacted, with its driest April to December period in its 87-year record (Section 2d9, Section 7f4). As in 2016/17, the Aleutian low was markedly weakened, leading to reduced rainfall and conditions conducive to major wildfires in the British Columbia region of Canada (Section 2h3; Figs. 2.36a–c; Section 7b1).

In 2017, the phase of the SNAO defined over July and August as in Folland et al. (2009) was on average slightly negative (Figs. 2.37a,b). As in 2016 (Allan and Folland 2017), there was a rather persistent anticyclonic anomaly over southern Greenland in both months, but this was markedly less intense and smaller than in 2016. This feature is normally associated with a negative SNAO. In fact, July (Fig. 2.37a) had a variable and overall negative SNAO as seen in the daily values (Fig. 2.37c). The most notable feature in summer 2017 was a mostly strong negative SNAO that lasted ten days from the end of July into early August. August overall showed a near-neutral SNAO despite the anticyclonic MSLP anomaly over southern Greenland (Fig. 2.37b) and the variable August daily SNAO series. The multidecadal tendency noted in Allan and Folland (2017) toward a more negative SNAO index since 1970 continued to slow. Thus, the average level of the SNAO index in the last five years is near the average observed over 1850–1960 but is considerably more negative than the positive

(a) Jul



(b) Aug



(c) Summer NAO Index

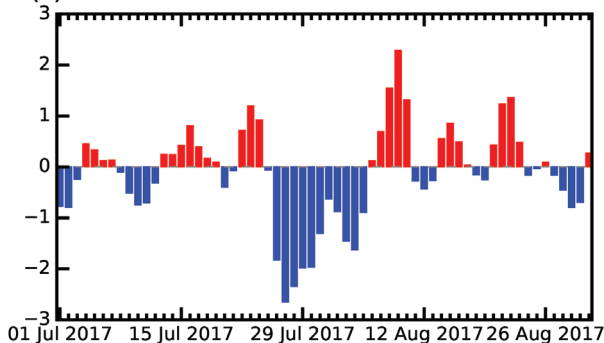


**FIG. 2.37.** MSLP anomalies (hPa; 1961–90 base period) in (a) Jul and (b) Aug 2017 over the extratropical North Atlantic and Europe. (c) Daily SNAO index for Jul and Aug 2017, calculated from eigenvectors of the daily SNAO.

index averaged over the two decades 1966–1985. Linderholm and Folland (2017) provide more detail on recent multidecadal changes in the SNAO index.

In the Southern Hemisphere, the AAO has been predominantly in its positive phase since 2015/16 (Fig. 2.35). This favors reduced sea ice extent in the West Antarctic Peninsula (WAP) region, owing to enhanced westerly wind conditions (Stammerjohn et al. 2008). In the interplay between the protracted El Niño, which favors a weaker polar jet stream, and a positive AAO mode, with stronger westerly winds, the former appears to have dominated. With the cessation of the protracted El Niño episode in mid-2016 (Allan and Folland 2017; Allan et al. 2018, manuscript

submitted to *Atmosphere*), and of a negative AAO (Fig. 2.35), there was a major reduction in the WAP sea ice margin centering on November 2016 and a slight recovery in extent through 2017 (see Section 6e) despite a return to positive AAO values (Fig. 2.35f; [http://nsidc.org/data/seaice\\_index/](http://nsidc.org/data/seaice_index/)).

## 2) SURFACE WINDS—C. Azorin-Molina, R. J. H. Dunn, C. A. Mears, P. Berrisford, and T. R. McVicar

Over land, observations of globally averaged wind speed continued to “recover” (commencing in ~2013; Dunn et al. 2016a; Azorin-Molina et al. 2017a) from the previous slowdown of winds (from ~1960s onwards; McVicar et al. 2012), termed “stilling” by Roderick et al. (2007). Surface wind speed increased in 2017 (Fig. 2.38a), showing a global (excluding Australia) average wind speed anomaly of  $+0.024 \text{ m s}^{-1}$  with respect to the 1981–2010 climatology (Table 2.4). Regionally, this recent rebound was caused by positive anomalies for central ( $+0.142 \text{ m s}^{-1}$ ) and East ( $+0.108 \text{ m s}^{-1}$ ) Asia, with Europe ( $+0.002 \text{ m s}^{-1}$ ) being very close to average. North America ( $-0.068 \text{ m s}^{-1}$ ) showed a negative anomaly but less negative than its 2012 record lowest anomaly. In contrast, Australia

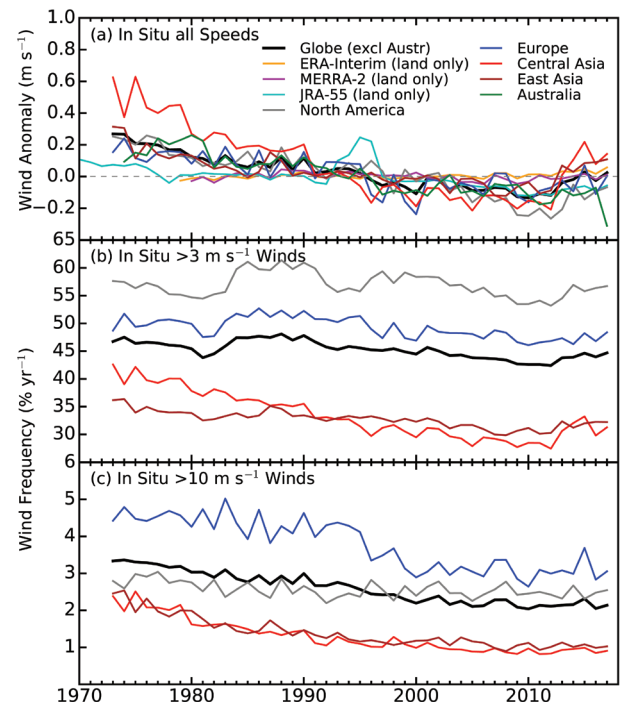


**FIG. 2.38.** Global (excluding Australia) and regional annual time series of land surface wind speed anomaly ( $\text{m s}^{-1}$ ; relative to 1981–2010) using HadISD2 (1973–2017), an Australian dataset, and ERA-Interim (1979–2017), MERRA-2 (1980–2017) and JRA-55 (1970–2017). Occurrence frequencies (in %) for wind speeds (b)  $>3 \text{ m s}^{-1}$  and (c)  $>10 \text{ m s}^{-1}$  do not include Australia.



**TABLE 2.4. Global and regional statistics for land surface wind speed using observational HadISD2 and Australian datasets for 1979–2017.**

Region	Mean 1981–2010 (m s <sup>-1</sup> )	Anomaly 2017 (m s <sup>-1</sup> )	Trend 1979–2017 (m s <sup>-1</sup> decade <sup>-1</sup> ) and 5th to 95th percentile confidence range	Number of Stations
<b>Globe (excluding Australia)</b>	3.332	+0.024	–0.066 (–0.074 → –0.058)	2632
<b>North America</b>	3.728	–0.068	–0.088 (–0.099 → –0.076)	598
<b>Europe</b>	3.662	+0.002	–0.057 (–0.070 → –0.047)	788
<b>Central Asia</b>	2.875	+0.142	–0.128 (–0.144 → –0.099)	263
<b>East Asia</b>	2.738	+0.108	–0.036 (–0.045 → –0.027)	474
<b>Australia</b>	2.091	–0.311	–0.092	28

(–0.311 m s<sup>-1</sup>) had the lowest anomaly in its time series. Excluding the latter, the 2017 anomalies continue to support the reversal in the “stilling” detected over the last few years. This rebound of wind speeds has also been reported elsewhere (South Korea, Kim and Paik 2015; and Saudi Arabia, Azorin-Molina et al. 2018a). The recent strengthening in terrestrial wind speed is much clearer for the moderate (>3 m s<sup>-1</sup>) than the strong (>10 m s<sup>-1</sup>) winds (Figs. 2.38b,c), as the occurrence of moderate winds has slightly increased after a steady slowdown since records began. The recovery of surface winds is not detected for those of strong intensity in 2017, which only showed a stabilization in frequency recently.

Two observational databases from anemometer records were chosen for evaluating the spatio-temporal variability of land-surface winds globally: (1) the HadISD2 (1973–2017; Dunn et al. 2012, 2016b) and (2) an Australian dataset (1979–2017; McVicar et al. 2008). As a result of unresolved differences for the wind run and wind speed data over Australia, this region is treated separately (see Dunn et al. 2016a). Both data sources were subject to quality control checks resulting in 2660 series for 1979–2017. Additionally, three reanalysis products (MERRA-2, 1980–2017; Gelaro et al. 2017; ERA-Interim, 1979–2017; Dee et al. 2011a; and JRA-55, 1970–2017; Kobayashi et al. 2015) were used to assess wind speed variability across land and ocean surfaces. A global reanalysis intercomparison (Torralba et al. 2017) has pointed out the large uncertainty in the ability of atmospheric

reanalyses to reproduce wind speed trends. This is shown in Fig. 2.38a, as the long-term variability of reanalyzed land surface winds is almost stable as opposed to the decline in the observations. The underestimation of the magnitude of reanalysis wind trends is mainly due to the shortcomings in the simulation of near-surface layer processes (e.g., McVicar et al. 2008; Pryor et al. 2009; Vautard et al. 2010).

The global land wind speed trend from observations was –0.066 m s<sup>-1</sup> decade<sup>-1</sup> for 1979–2017, which is slightly less negative than the 1979–2016

trends (–0.070 m s<sup>-1</sup> decade<sup>-1</sup>; Azorin-Molina et al. 2017a). As shown in Table 2.4, the strongest 1979–2017 negative trends are in Central Asia (–0.128 m s<sup>-1</sup> decade<sup>-1</sup>) and North America (–0.088 m s<sup>-1</sup> decade<sup>-1</sup>), whereas the weakest ones are in East Asia (–0.036 m s<sup>-1</sup> decade<sup>-1</sup>) and Europe (–0.057 m s<sup>-1</sup> decade<sup>-1</sup>). For all these regions, the magnitude of observed trends is also less negative than Azorin-Molina et al. (2017a), except for Australia (–0.092 m s<sup>-1</sup> decade<sup>-1</sup>). Individual station trends (Fig. 2.39) are 64.9% negative from the HadISD2 dataset, and 96.4% negative for the Australian dataset. Even though a recent recovery of terrestrial surface wind speeds is detected, when considering the past four decades “stilling” remains widespread (McVicar et al. 2012).

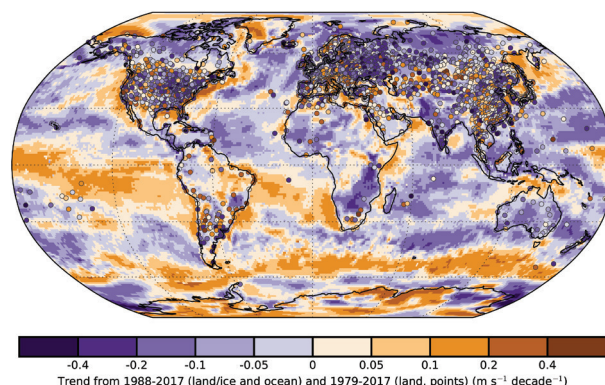


**FIG. 2.39. Wind speed trends (m s<sup>-1</sup> decade<sup>-1</sup>) for the observational HadISD2 and Australian datasets (circles) over land for 1979–2017, and MERRA2 over land/ice and RSS over ocean for 1988–2017 (shaded areas).**

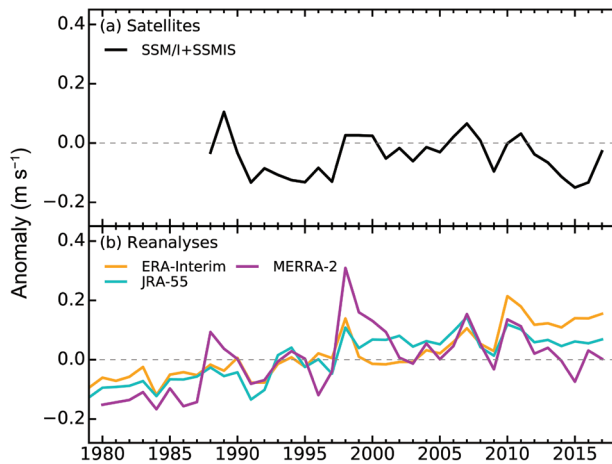


**FIG. 2.40. Global average surface wind anomaly ( $\text{m s}^{-1}$ ; 1981–2010 base period) over ocean from (a) satellite radiometers and (b) reanalyses.**

Satellite-borne microwave radiometers and the three above-mentioned reanalysis products were chosen for assessing surface wind variability over oceans. During 2017, global wind speed anomalies for the satellite estimates (Fig. 2.40a) were close to zero, with reanalysis showing neutral to positive anomalies (Fig. 2.40b). In comparison to 2016, over ocean, globally averaged wind speed anomalies tended to be less negative (or even positive) for all products; in agreement with the observed recovery of terrestrial surface winds. The strongest spatial anomalies for 2017 (Plate 2.1v) corresponded to: (1) strong negative anomalies dominating in the Gulf of Alaska and for much of the Atlantic Ocean north of the equator, as well as in the southwest Pacific–Tasman Sea and western Indian Ocean; and (2) strong positive anomalies mostly observed over the South Pacific and South Atlantic Oceans and parts of the Southern and Arctic Oceans.

The limited knowledge about the causes behind the stalling phenomenon and the recent recovery of surface winds suggests the need for comprehensive attribution analyses of wind speed variability over land and ocean and at different altitudes (i.e., including high-elevation stations; Azorin-Molina et al. 2017c). In the last few years the scientific literature has attributed the stalling over land to three major drivers: (1) increase of surface roughness (Vautard et al. 2010; Bichet et al. 2012; Wever 2012; Wu et al. 2016); (2) large-scale atmospheric circulation changes (Azorin-Molina et al. 2014, 2016); and (3) instrumental issues (Wan et al. 2010; Azorin-Molina et al. 2017b, 2018b). The attribution analysis of the recent recovery of surface winds is also complicated by interplaying factors, and future research should fill this knowledge gap.

### 3) UPPER AIR WINDS—L. Haimberger, M. Mayer, and V. Schenzinger

Figure 2.41 shows global (land + ocean) mean 850-hPa wind speed anomalies from reanalyses and in situ upper air (TEMP and PILOT) observations, for comparison with surface wind speed anomalies in Section 2e2. There is a general tendency towards higher wind speeds at this level, at least in the reanalysis data, but only trends from ERA-Interim (Dee et al. 2011a) and MERRA2 (Gelaro et al. 2017) for 1979–2017 are statistically significant (95% confidence). Trends are larger over the oceans, particularly in the Pacific trade wind region, and weaker over land. At higher levels (200–300 hPa), the global wind trends turn negative (not shown) but remain weak.

The annual mean 850-hPa wind speeds for 2017 are clearly above normal ( $0.22 \text{ m s}^{-1}$  in ERA-Interim), consistent with the overall increasing trend at this level and also with the recovery of the surface winds from wind stalling noted in Section 2e2. They appear anomalously high particularly in the tropics, as can be seen from Plate 2.1w, with stronger-than-normal easterlies over large regions. This result should be taken with care though, because Liu and Allan (2018) recently have detected problems with reanalysis winds.

Over land (not shown), the 850-hPa trends from reanalyses are only weakly positive ( $0.01 \text{ m s}^{-1} \text{ decade}^{-1}$  in ERA-Interim for the 1979–2017 period; the 2017 anomaly is  $0.13 \text{ m s}^{-1}$ ). They are still slightly more positive than the surface wind trends over land (see Section 2e2). The in situ upper air dataset (GRASP; Ramella Pralungo et al. 2014) has negative trends ( $-0.03 \text{ m s}^{-1} \text{ decade}^{-1}$ ) in the period 1979–2016. The anomalies of this dataset in the most recent years were, however, also slightly positive, similar to the surface wind anomalies (see Section 2e2).

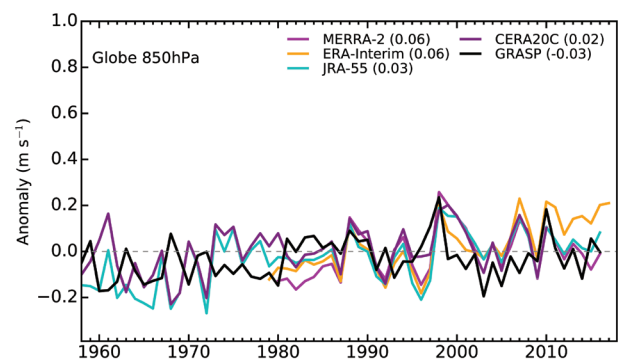


**FIG. 2.41. Annual anomalies of global mean wind speed ( $\text{m s}^{-1}$ ; base period 1981–2010) at 850 hPa from four reanalyses and one observational dataset (GRASP; Ramella Pralungo et al. 2014). The numbers in brackets are linear trends in  $\text{m s}^{-1} \text{ decade}^{-1}$ ; valid for 1979–2017.**

To date, there is no independent satellite-derived product for upper air winds. Atmospheric motion vectors from AVHRR have been reprocessed recently at EUMETSAT and are ready to be assimilated (Schulz et al. 2017); however no gridded product has been generated.

The 2017 Atlantic hurricane season (see Section 4f2) deserves special attention since it was exceptionally intense, particularly at peak time (mid-August–September). From an upper air circulation perspective, one cause that may have favored the observed large number of strong hurricanes is anomalously large upper-level divergence, a parameter whose importance has been stressed in previous *State of the Climate* reports. A second factor may be the abundance of strong tropical easterly wave disturbances that can amplify under favorable conditions (Dieng et al. 2017; Russell et al. 2017). Figure 2.42 shows that upper level divergence averaged over August and September was anomalously positive throughout the western Atlantic. Together with negative (positive) values over the eastern (western) tropical Pacific, this is consistent with weak La Niña conditions establishing at that time (Mayer et al. 2013). However, it is difficult to separate cause and effect for the anomaly in the upper air circulation over the western Atlantic, because the strong hurricanes themselves potentially contributed to the anomalies in that region.

Tropical wave activity was also high, as shown in the Hovmöller diagram [similar, for example, to Seo et al. (2008)] in Fig. 2.43 for the period 15 August–1 October, during which four major hurricanes were observed. In particular the standard deviation of meridional wind speed in the west central Atlantic was high compared with 2015, 2016, and the 1979–2017 climatology, which shows slowly decaying wave activity from the maximum near the West African coast toward the west. The strong waves in 2017 together with the anomalously high oceanic heat content (see Section 3c) likely fostered the quick formation of Irma, Jose, and Maria, which developed into major hurricanes already over the west central Atlantic. Hurricanes are visible in Fig. 2.43 as regions of extreme east–west wind gradients.

The quasi-biennial oscillation (QBO; see also Section 2b5) exhibited an unprecedented anomaly at the beginning of 2016. It was characterized by highly unusual and strong upward propagation of equatorial wind regimes, particularly between 10-hPa and 40-hPa (Newman et al 2016; Dunkerton 2016). The

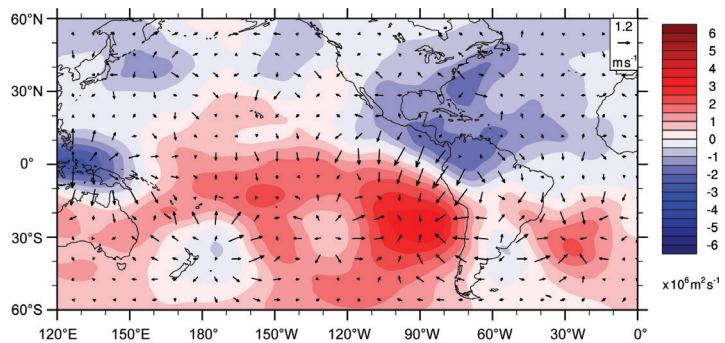


**FIG. 2.42. Aug–Sep 2017 average of velocity potential anomaly ( $\times 10^6 \text{ m}^2 \text{ s}^{-1}$ ) and divergent wind at 200 hPa (vector arrows) compared to the 1979–2016 Aug–Sep climatology. Velocity potential anomaly minima indicate positive divergence anomalies. (Source: ERA-Interim.)**

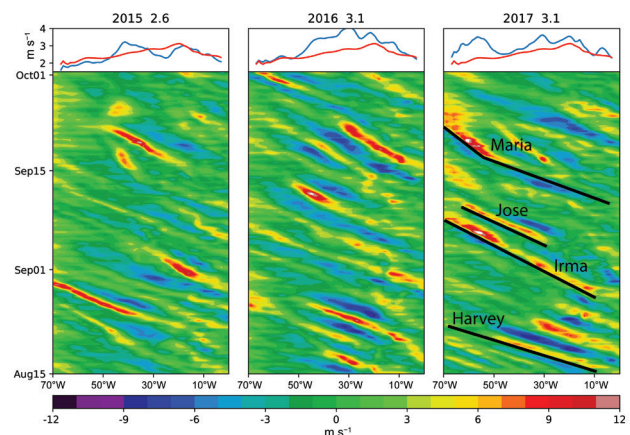


**FIG. 2.43. Hovmöller diagrams of 850-hPa meridional wind ( $\text{m s}^{-1}$ ) averaged over  $8^{\circ}$ – $18^{\circ}\text{N}$  (the region with strongest wave disturbances according to Dieng et al. 2017) for the peak hurricane season 15 Aug–1 Oct between  $70^{\circ}\text{W}$  and  $0^{\circ}$ . 6-hourly ERA-Interim wind fields at  $1^{\circ}$  resolution without any filter have been used. Upper panels show standard deviation of meridional wind ( $\text{m s}^{-1}$ ) as a function of longitude in individual years (blue) and for the 1979–2017 average (red). Selected waves that developed into hurricanes in 2017 are marked with lines and named.**

anomaly decayed in 2017 and the usual oscillation resumed with a relatively large, but not exceptional, amplitude (Online Fig. S2.16). However, the westerly wind regime at 20-hPa lasted for 24 months, compared to the average duration of 13 months and the mean QBO period of 28 months (e.g., Schenzinger et al. 2017). A new analysis by Watanabe et al. (2018) points to interaction of extratropical Rossby waves with the mean equatorial flow as main reason for the anomaly. Comparison of this episode with results from historical CMIP climate model runs shows only one similar event in the model data (Osprey et al. 2016; see also Schenzinger 2016).



## f. Earth radiation budget

### 1) EARTH RADIATION BUDGET AT TOP-OF-ATMOSPHERE—

T. Wong, D. P. Kratz, P. W. Stackhouse, Jr., P. Sawaengphokhai, A. C. Wilber, S. K. Gupta, and N. G. Loeb

The energetic state of the Earth–atmosphere system is defined by the balance of the incoming total solar irradiance (TSI) from the Sun with the reflected shortwave (RSW) and the outgoing longwave radiation (OLR) from Earth. This balance characterizes Earth’s radiation budget (ERB) at the top of the atmosphere (TOA) and drives weather processes and climate forcings as well as climate feedbacks.

An analysis of all CERES ERB measurements (Table 2.5) shows that the 2017 global annual mean OLR remained approximately unchanged while the RSW decreased by  $\sim 0.05 \text{ W m}^{-2}$  relative to their corresponding values in 2016. Over the same timeframe, the global annual mean TSI declined by  $\sim 0.10 \text{ W m}^{-2}$ . The sum of these components amounts to a small reduction of  $\sim 0.05 \text{ W m}^{-2}$  in the global annual mean total net radiation into the Earth climate system for 2017 as compared with 2016. Relative to the multiyear data average from 2001 to 2016, the 2017 global annual mean flux anomalies (Table 2.5) are  $+0.50$ ,  $-0.10$ ,  $-0.80$ , and  $+0.20 \text{ W m}^{-2}$  for OLR, TSI, RSW, and total net flux, respectively. These changes are at or within the corresponding 2-sigma interannual variability (Table 2.5) for this period.

The global monthly mean anomaly time series of TOA fluxes (Fig. 2.44) reveals that the global monthly mean OLR anomaly stayed mostly positive throughout 2017. The OLR anomaly began 2017 with a value of  $+0.9 \text{ W m}^{-2}$ , reached its maximum value of  $+1.2 \text{ W m}^{-2}$  in April, dropped to its minimum value of  $-0.2 \text{ W m}^{-2}$  in August, then oscillated around  $+0.4 \text{ W m}^{-2}$  for the rest of the year. The global monthly mean absorbed shortwave (TSI–RSW) anomaly also remained

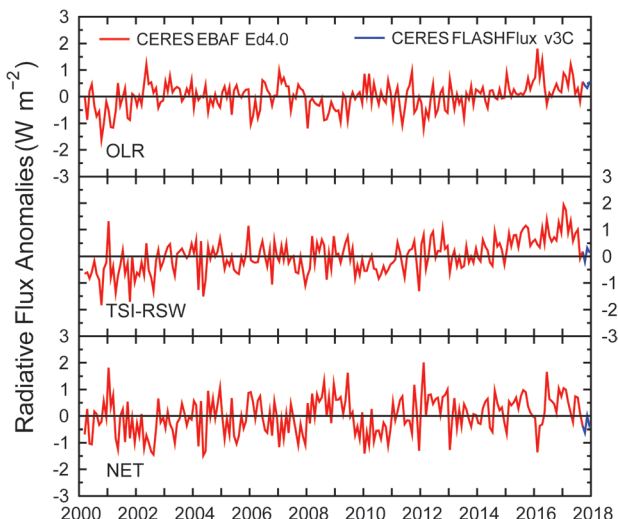


**FIG. 2.44. Time series of global monthly mean de-seasonalized anomalies ( $\text{W m}^{-2}$ ) of TOA Earth radiation budget for OLR (upper), absorbed shortwave (TSI–RSW; middle), and total net (TSI–RSW–OLR; lower) from Mar 2000 to Dec 2017. Anomalies are relative to their calendar month climatology (2001–16). Time series shows the CERES EBAF Ed4.0 1Deg data (Mar 2000–Sep 2017) in red and the CERES FLASHFlux version 3C data (Oct–Dec 2017) in blue; see text for merging procedure**

mostly positive during 2017, and the magnitudes of this anomaly were larger than the corresponding OLR anomaly. The absorbed shortwave anomaly started the year with a maximum value of  $+1.9 \text{ W m}^{-2}$ , decreased to a minimum value of  $-0.2 \text{ W m}^{-2}$  in October, then climbed back to a positive value at year end. For the year as a whole, the 2017 global annual mean absorbed shortwave anomaly is  $+0.7 \text{ W m}^{-2}$ . The global monthly mean total net anomaly, which is calculated from absorbed shortwave anomaly minus OLR anomaly, began 2017 with a maximum

**TABLE 2.5. Global annual mean TOA radiative flux changes between 2016 and 2017, the global annual mean radiative flux anomalies relative to their corresponding 2001–16 mean climatological values, and the 2-sigma interannual variabilities of the 2001–16 global annual mean fluxes (all units in  $\text{W m}^{-2}$ ) for the outgoing longwave radiation (OLR), total solar irradiance (TSI), reflected shortwave (RSW) and total net fluxes. All flux values have been rounded to the nearest  $0.05 \text{ W m}^{-2}$ .**

	One Year Change (2017 minus 2016)	2017 Anomaly (Relative to Climatology)	Interannual Variability (2001 to 2016)
<b>OLR</b>	0.00	+0.50	$\pm 0.60$
<b>TSI</b>	-0.10	-0.10	$\pm 0.15$
<b>RSW</b>	-0.05	-0.80	$\pm 0.80$
<b>Net</b>	-0.05	+0.20	$\pm 0.75$

value of  $+1.0 \text{ W m}^{-2}$ , remained mostly positive for eight months, declined to mostly negative in the last four months of the year, and ended the year with a value of  $-0.4 \text{ W m}^{-2}$ . The positive absorbed shortwave anomaly in 2017 dominated the negative effect of OLR anomaly and resulted in a slightly positive 2017 global annual mean total net anomaly of  $+0.2 \text{ W m}^{-2}$ . Long-term trend analyses that include the last three months of the merged dataset are discouraged because of the natural fluctuation in ERB components, uncertainty from the data merging process, and potential for drift in the FLASHFlux product.

The TSI data used in this study are provided by the Total Irradiance Monitor aboard the Solar Radiation and Climate Experiment (SORCE) mission (Kopp and Lean 2011) and the Royal Meteorological Institute of Belgium composite dataset (Dewitte et al. 2004), both renormalized to the SORCE Version 15. The RSW and OLR data were obtained from the Clouds and the Earth's Radiant Energy System (CERES) mission (Wielicki et al. 1996, 1998) aboard *Terra* and *Aqua*.

The time series (Fig. 2.44) was constructed from the CERES EBAF (Energy Balanced And Filled) Ed4.0 product (Loeb et al. 2009, 2012, 2018) for March 2000 to September 2017 and from the CERES Fast Long-wave and Shortwave Radiative Fluxes (FLASHFlux) version 3C product (Kratz et al. 2014), for October to December 2017. The normalization of the FLASHFlux data (Stackhouse et al. 2016) results in a 2-sigma monthly uncertainty of  $\pm 0.43$ ,  $\pm 0.08$ ,  $\pm 0.20$  and  $\pm 0.55 \text{ W m}^{-2}$  for the OLR, TSI, RSW, and total net radiation, respectively.

#### g. Atmospheric composition

##### 1) LONG-LIVED GREENHOUSE GASES—E. J. Dlugokencky, B. D. Hall, S. A. Montzka, G. Dutton, J. Mühle, and J. W. Elkins

The three long-lived greenhouse gases (LLGHGs) with the largest contributions to climate forcing are, in decreasing order: carbon dioxide ( $\text{CO}_2$ ), methane ( $\text{CH}_4$ ), and nitrous oxide ( $\text{N}_2\text{O}$ ). Systematic measurements of  $\text{CO}_2$  began at Mauna Loa, Hawaii (MLO) in 1958, when the atmospheric  $\text{CO}_2$  abundance was  $\sim 315$  ppm (parts per million in dry air). In 2017, MLO annually averaged  $\text{CO}_2$  reached  $406.5 \pm 0.1$  ppm ([www.esrl.noaa.gov/gmd/ccgg/trends/](http://www.esrl.noaa.gov/gmd/ccgg/trends/); all uncertainties are 68% confidence intervals, unless noted otherwise), while preliminary globally averaged  $\text{CO}_2$  at Earth's surface was  $405.0 \pm 0.1$  ppm (Fig. 2.45a, see [www.esrl.noaa.gov/gmd/ccgg/trends/global.html](http://www.esrl.noaa.gov/gmd/ccgg/trends/global.html)).

The atmospheric history of  $\text{CO}_2$  prior to 1958 is determined from air extracted from ice in Greenland and Antarctica. From those measurements, it is known that the abundance of atmospheric  $\text{CO}_2$  was

$\sim 278$  ppm in 1750 (Etheridge et al. 1996). Since then,  $\sim 430 \text{ Pg C}$  ( $1 \text{ Pg C} = 10^{15} \text{ g C}$ ) were emitted as  $\text{CO}_2$  to the atmosphere from fossil fuel burning and cement production (Boden et al. 2017). Based on observations of atmospheric  $\text{CO}_2$  and  $\text{N}_2/\text{O}_2$  (Manning and Keeling 2006) and increased carbon in the oceans (Sabine et al. 2004), most of the anthropogenic  $\text{CO}_2$  not remaining in the atmosphere was taken up by the oceans (Tans 2009). While the terrestrial biosphere is currently also a net sink for fossil fuel  $\text{CO}_2$ , net emissions of  $\text{CO}_2$  to the atmosphere from land use change prior to  $\sim 1940$  offset recent terrestrial uptake (Tans 2009). These mass balance considerations overwhelmingly suggest that the observed increase in atmospheric  $\text{CO}_2$  since 1750 is caused by combustion of fossil fuels. This conclusion is further supported by measured decreases in  $^{13}\text{C}/^{12}\text{C}$  and  $^{14}\text{C}/^{12}\text{C}$  of atmospheric  $\text{CO}_2$ , and an increase in the north-south gradient of atmospheric  $\text{CO}_2$  abundance (Tans 2009).

The global growth rate of  $\text{CO}_2$  has risen from  $0.6 \pm 0.1 \text{ ppm yr}^{-1}$  in the early 1960s to an average of  $2.3 \text{ ppm yr}^{-1}$  during the past ten years, with interannual variability of  $\pm 0.5 \text{ ppm yr}^{-1}$  (1-sigma) (Fig. 2.45). The increase in global annual mean  $\text{CO}_2$  from 2016 to 2017 was  $2.2 \pm 0.1 \text{ ppm}$ . In the two years prior to this (2015 and 2016), atmospheric  $\text{CO}_2$  increased by  $3.0 \text{ ppm yr}^{-1}$ . The strong El Niño that peaked in late-2015 contributed to this strong  $\text{CO}_2$  increase (Betts et al. 2016).

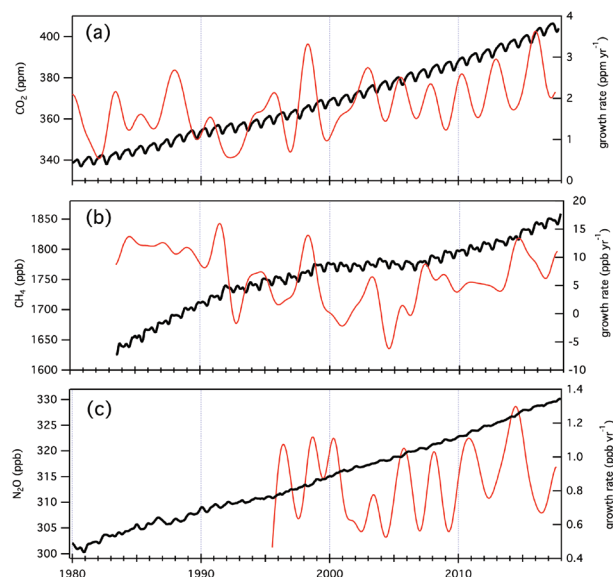


**FIG. 2.45.** Global mean surface mole fractions (in dry air) of (a)  $\text{CO}_2$  (ppm), (b)  $\text{CH}_4$  (ppb), and (c)  $\text{N}_2\text{O}$  (ppb) derived from the NOAA sampling network. Growth rates are shown on the right axis. (Measurements were not sufficient to calculate instantaneous growth rates for  $\text{N}_2\text{O}$  with reasonable certainty prior to 1995).

The 2017 globally averaged methane mole fraction at Earth's surface was  $1849.7 \pm 0.8$  ppb (Dlugokencky 2018). The increase in annual mean  $\text{CH}_4$  from 2016 to 2017 was  $6.9 \pm 0.9$  ppb, comparable to the average growth rate over the past 10 years ( $+7.1 \pm 2.6$  ppb  $\text{yr}^{-1}$ ; the uncertainty is the standard deviation of annual increases). Since 1750,  $\text{CH}_4$  has increased by  $\sim 1128$  ppb from  $722 \pm 15$  ppb.

Atmospheric  $\text{CH}_4$  is influenced by a complex mix of sources and sinks, with emissions from both anthropogenic ( $\sim 60\%$ ) and natural ( $\sim 40\%$ ) sources (Fung et al. 1991). Its main loss process, atmospheric oxidation initiated by reaction with hydroxyl radical ( $\text{OH}$ ), is the largest term in the atmospheric  $\text{CH}_4$  budget of sources and sinks. Total global emissions of  $\text{CH}_4$  are well-constrained by the atmospheric measurements and an estimate of its lifetime (Dlugokencky et al. 2011), but the magnitude and trend in emissions from individual sources and trends in  $\text{CH}_4$  atmospheric lifetime are still highly uncertain. In the past three decades, the  $\text{CH}_4$  growth rate has undergone long- and short-term changes (red line in Fig. 2.45b). Analysis of these changes can be used to improve understanding of processes that emit and remove  $\text{CH}_4$ , but so far, causes behind even large changes have not been unambiguously identified. Numerous publications address the increase in growth rate that started in 2007; measurements of  $\text{CH}_4$  abundance and its isotopic composition strongly suggest increased emissions from biogenic sources, both natural and anthropogenic (Nisbet et al. 2016; Schaefer et al. 2016; Schwietzke et al. 2016), rather than changes in fossil fuel-related emissions. Changes in other  $\text{CH}_4$  sources (e.g., Worden et al. 2017) and  $\text{CH}_4$  loss rate (Prather and Holmes 2017) have also been implicated, but because the problem is underconstrained by observations, all explanations are uncertain.

Nitrous oxide ( $\text{N}_2\text{O}$ ) is both a greenhouse gas and an ozone-depleting substance (Ravishankara et al. 2009). Sources include natural and agricultural soils as well as oceans. Anthropogenic activity is thought to contribute about one-third to total global emissions of  $\sim 18$  Tg  $\text{yr}^{-1}$  (Ciais et al. 2013). Except for a brief period in the 1940s, atmospheric  $\text{N}_2\text{O}$  has been increasing steadily throughout the industrial era (MacFarling Meure et al. 2006). The mean global atmospheric  $\text{N}_2\text{O}$  mole fraction in 2017 was  $329.8 \pm 0.1$  ppb, an increase of 0.9 ppb from 2016 (Fig. 2.45c). This 0.9 ppb annual change is similar to the average annual change over the last two decades ( $0.85 \pm 0.17$  ppb).

The NOAA Annual Greenhouse Gas Index (AGGI) (Fig. 2.46) summarizes trends in the combined direct radiative forcing by five major LLGHGs

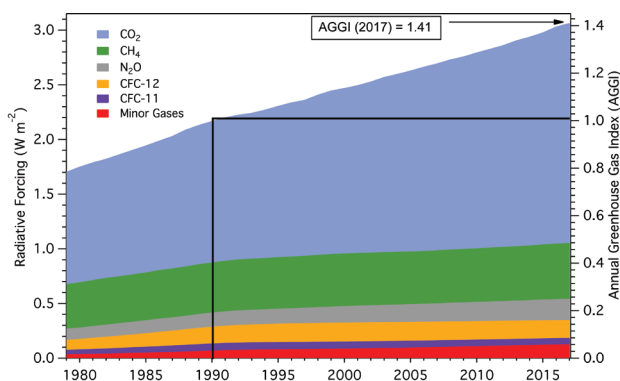


**FIG. 2.46. Direct radiative forcing ( $\text{W m}^{-2}$ ) due to 5 major LLGHG and 15 minor gases (left axis) and the associated values of the AGGI (right axis).**

( $\text{CO}_2$ ,  $\text{CH}_4$ ,  $\text{N}_2\text{O}$ , CFC-11, and CFC-12) and 15 minor gases (Hofmann et al. 2006; Table 2.6; Fig. 2.47; [www.esrl.noaa.gov/gmd/aggi/](http://www.esrl.noaa.gov/gmd/aggi/)). The AGGI represents the annual cumulative radiative forcing of these gases relative to the Kyoto Protocol baseline year of 1990 ( $2.16 \text{ W m}^{-2}$ ). It does not include indirect radiative forcing (e.g., influences on ozone and water vapor). In 2017,  $\text{CO}_2$  contributed  $2.01 \text{ W m}^{-2}$  direct radiative forcing, or about 66% of the combined forcing of  $3.06 \text{ W m}^{-2}$  from LLGHGs.  $\text{CH}_4$  and  $\text{N}_2\text{O}$  contributed  $0.5 \text{ W m}^{-2}$  (16%) and  $0.2 \text{ W m}^{-2}$  (6.5%) respectively, while the sum of halogenated gases, including CFCs, HCFCs, and HFCs, among others (Table 2.6), con-

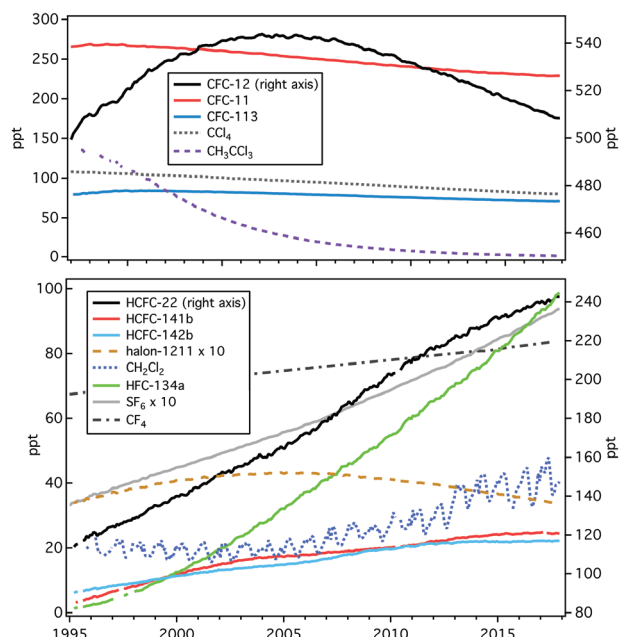


**FIG. 2.47. Global mean mole fractions at Earth's surface (ppt, dry air) for several LLGHG, many of which also deplete stratospheric ozone. See Table 2.6 for the 2017 global mean mole fractions of these gases.**



**TABLE 2.6. Summary table of long-lived greenhouse gases for 2017 (CO<sub>2</sub> mixing ratios are in ppm, N<sub>2</sub>O and CH<sub>4</sub> in ppb, and all others in ppt).**

Industrial Designation or Common Name	Chemical Formula	AGGI	ODGI	Radiative Efficiency (W m <sup>-2</sup> ppb <sup>-1</sup> ) <sup>a</sup>	Mean Surface Mole 2017 Fraction (change from prior year) <sup>b</sup>	Lifetime (years)
Carbon Dioxide	CO <sub>2</sub>	Y	N	1.37 × 10 <sup>-5</sup>	405.0 (2.2) <sup>c</sup>	
Methane	CH <sub>4</sub>	Y	N	3.63 × 10 <sup>-4</sup>	1849.7 (6.9) <sup>c</sup>	9.1
Nitrous Oxide	N <sub>2</sub> O	Y	N	3.00 × 10 <sup>-3</sup>	329.8 (0.9) <sup>c,d</sup>	123
<b>Chlorofluorocarbons</b>						
CFC-11	CCl <sub>3</sub> F	Y	Y	0.26	228.9 (−0.8) <sup>c,d</sup>	52
CFC-12	CCl <sub>2</sub> F <sub>2</sub>	Y	Y	0.32	509.3 (−2.9) <sup>c,d</sup>	102
CFC-113	CCl <sub>2</sub> FCFClF <sub>2</sub>	Y	Y	0.30	70.9 (−0.5) <sup>c</sup>	93
<b>Hydrochlorofluorocarbons</b>						
HCFC-22	CHClF <sub>2</sub>	Y	Y	0.21	240.8 (3.3)	11.9
HCFC-141b	CH <sub>3</sub> CCl <sub>2</sub> F	Y	Y	0.16	24.5 (−0.4)	9.4
HCFC-142b	CH <sub>3</sub> CCIF <sub>2</sub>	Y	Y	0.19	22.1 (0.2)	18
<b>Hydrofluorocarbons</b>						
HFC-134a	CH <sub>2</sub> FCF <sub>3</sub>	Y	N	0.16	95.7 (6.1)	14
HFC-152a	CH <sub>3</sub> CHF <sub>2</sub>	Y	N	0.10	6.8 (0.2)	1.6
HFC-143a	CH <sub>3</sub> CF <sub>3</sub>	Y	N	0.16	20.6 (1.6)	51
HFC-125	CHF <sub>2</sub> CF <sub>3</sub>	Y	N	0.23	22.8 (2.7)	31
HFC-32	CH <sub>2</sub> F <sub>2</sub>	N	N	0.11	13.0 (1.8)	5.4
HFC-23	CHF <sub>3</sub>	Y	N	0.18	29.9 (1.0)	228
HFC-365mfc	CH <sub>3</sub> CF <sub>2</sub> CH <sub>2</sub> CF <sub>3</sub>	N	N	0.22	0.93 (0.05)	8.7
HFC-227ea	CF <sub>3</sub> CHFCF <sub>3</sub>	N	N	0.26	1.29 (0.12)	36
<b>Chlorocarbons</b>						
Methyl Chloroform	CH <sub>3</sub> CCl <sub>3</sub>	Y	Y	0.07	2.2 (−0.4)	5.0
Carbon Tetrachloride	CCl <sub>4</sub>	Y	Y	0.17	80.2 (−0.9) <sup>c,d</sup>	33
Methyl Chloride	CH <sub>3</sub> Cl	N	Y	0.01	547.3 (−12.1)	0.9
<b>Bromocarbons</b>						
Methyl Bromide	CH <sub>3</sub> Br	N	Y	0.004	6.6 (−0.2)	0.8
Halon 1211	CBrClF <sub>2</sub>	Y	Y	0.29	3.43 (−0.09)	16
Halon 1301	CBrF <sub>3</sub>	Y	Y	0.30	3.26 (0.00)	72
Halon 2402	CBrF <sub>2</sub> CBrF <sub>2</sub>	Y	Y	0.31	0.4 (−0.01)	28
<b>Fully fluorinated species</b>						
Sulfur Hexafluoride	SF <sub>6</sub>	Y	N	0.57	9.26 (0.34)	>600
PFC-14	CF <sub>4</sub>	N	N	0.09	83.6 (0.9) <sup>c</sup>	~50 000
PFC-116	C <sub>2</sub> F <sub>6</sub>	N	N	0.25	4.66 (0.10) <sup>c</sup>	~10 000

<sup>a</sup> Radiative efficiencies were taken from IPCC AR5 (Myhre et al. 2013). Steady-state lifetimes were taken from Myhre et al. (2013) (CH<sub>4</sub>), Ray et al. (2017) (SF<sub>6</sub>), Ko et al. (2013), Liang et al. (2016) (CCl<sub>4</sub>), and Carpenter et al. (2014). For CO<sub>2</sub>, numerous removal processes complicate the derivation of a global lifetime.

<sup>b</sup> Mole fractions are global, annual surface means for the indicated calendar year determined from the NOAA cooperative global air sampling network (Hofmann et al. 2006), except for PFC-14, PFC-116, and HFC-23, which were measured by AGAGE (Mühle et al., 2010; Miller et al., 2010). Changes indicated in brackets are the differences between the 2017 and 2016 means.

<sup>c</sup> Preliminary estimate.

<sup>d</sup> Global mean estimates derived from multiple NOAA measurement programs (“Combined Dataset”).

tributed  $0.34 \text{ W m}^{-2}$  (11%).  $\text{CH}_4$ -related production of tropospheric  $\text{O}_3$  and stratospheric  $\text{H}_2\text{O}$  contributed  $\sim 0.3 \text{ W m}^{-2}$  indirect radiative forcing (Myhre et al. 2013). The combined direct forcing in 2017 represents a 41% increase since 1990 (2017 AGGI = 1.41).

## 2) OZONE-DEPLETING GASES—B. D. Hall, S. A. Montzka, G. Dutton, B. R. Miller, and J. W. Elkins

Chlorine and bromine from CFCs, HCFCs, halons, and other ozone-depleting substances (ODS) are released in the stratosphere, causing ozone destruction. The emissions and atmospheric abundances of most ODS are declining as expected due to controls implemented in the Montreal Protocol and its Amendments (Carpenter et al. 2014). An exception is carbon tetrachloride, which has not decreased as expected for a number of years (Carpenter et al. 2014). Furthermore, it has recently been reported that the atmospheric abundance of CFC-11 has not declined as rapidly as expected, leading to concern that sustained increased emissions of CFC-11 would substantially delay the recovery of stratospheric ozone (Montzka et al. 2018). CFC-11 declined at a rate of  $2.1 \pm 0.3 \text{ ppt yr}^{-1}$  from 2002 through 2011, but that rate slowed to  $1.0 \pm 0.2 \text{ ppt yr}^{-1}$  from mid-2015 to mid-2017 (Montzka et al. 2018). The observed changes in CFC-11 are due to an increase in emissions, although some changes in atmospheric transport also contributed in some years. In addition, emissions and abundances of some short-lived chlorine-containing gases, which are not controlled by the Protocol, have increased recently and could delay ozone recovery if they were to continue to increase at similar rates in the future. For example, the atmospheric abundance of  $\text{CH}_2\text{Cl}_2$  has approximately doubled over the past fifteen years (Fig. 2.47; Hossaini et al. 2017).

Equivalent effective stratospheric chlorine (EESC) is a measure of the ozone-depleting potential of the stratospheric halogen loading at a given time and place. As EESC declines, stratospheric ozone is showing signs of recovery (Kuttippurath and Nair 2017; Strahan and Douglass 2018; see Sections 2g4 and 6h). EESC is calculated from global average surface mole fractions of long-lived ozone-depleting gases and weighting factors that include surface-to-stratosphere transport times, mixing during transit, photolytic reactivity, and ozone-destruction efficiency (Montzka et al. 1996; Newman et al. 2007). Short-lived gases such as  $\text{CH}_2\text{Cl}_2$  are not included in EESC. NOAA tracks changes in EESC with an Ozone-Depleting Gas Index (ODGI; Hofmann and Montzka 2009; [www.esrl.noaa.gov/gmd/odgi/](http://www.esrl.noaa.gov/gmd/odgi/)).

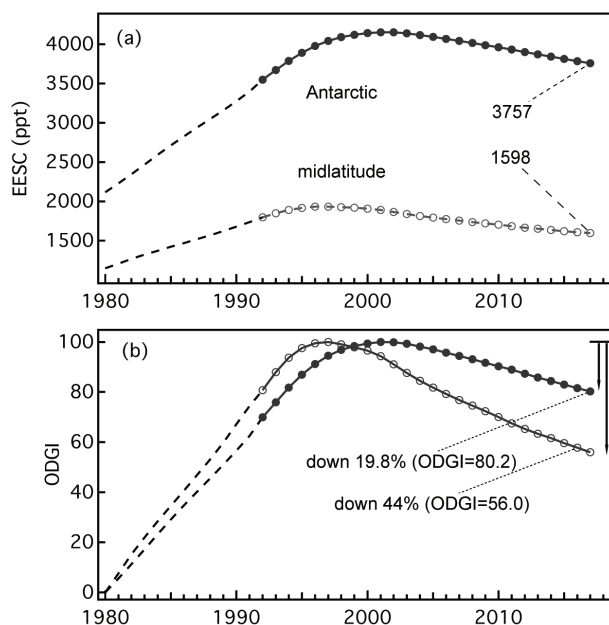


**FIG. 2.48. (a) EESC (ppt) and (b) NOAA ODGI.** The ODGI represents the relative mole fractions of reactive halogen in the midlatitude (open circles) and Antarctic stratosphere (closed circles) scaled such that  $\text{ODGI} = 100$  at maximum EESC and zero in 1980. Both EESC and ODGI are derived from NOAA surface measurements of long-lived ODS (circles) or, for earlier years, WMO scenarios (dashed lines; N. Harris et al. 2014). The EESC and ODGI values from 1992 forward correspond to Jan of each year.

EESC and ODGI have been calculated since 1992 for two representative stratospheric regions—Antarctica and the midlatitudes—that differ in total available reactive halogen (Fig. 2.48). EESC is larger in the Antarctic stratosphere than in the midlatitudes because more ozone-reactive halogen is released during the longer transit time to the Antarctic from midlatitude surface-based source regions. ODGI values at the beginning of 2017 were approximately 80 and 56 for the Antarctic and midlatitudes, respectively. These represent 20% ( $100 \text{ minus } 80$ ) and 44% ( $100 \text{ minus } 56$ ) reductions from the peak values in EESC over Antarctica and the midlatitudes, respectively, toward the 1980 benchmark values.

## 3) AEROSOLS—S. Rémy, N. Bellouin, A. Benedetti, and O. Boucher

Atmospheric aerosols are a key component of air quality and are now recognized as a serious public health issue (WHO 2013). They also play an important role in the climate system, by scattering and absorbing short- and long-wave radiation, and by indirectly affecting the life cycle, optical properties, and precipitation activity of clouds.

The Copernicus Atmosphere Monitoring Service (CAMS; <http://atmosphere.copernicus.eu>) runs a near real time (NRT) global analysis of aerosols and trace gases. The CAMS project also produced a reanalysis of global aerosols and trace gases that spanned 2003 to 2015 (Flemming et al. 2017) named the CAMS interim reanalysis (CAMSiRA). This reanalysis was extended to 2017.

Retrievals of aerosol optical depth (AOD) at 550 nm (Remer et al. 2005) from the MODIS instrument onboard NASA's *Aqua* and *Terra* (Collection 5) were used as observational constraints from 2003 to 2016. In 2017, MODIS Collection 6 (Sayer et al. 2014) was assimilated, which can lead to significant differences between 2017 and the previous years in CAMSiRA.

Aerosols are produced both by mechanical up-lifting over ocean (marine aerosols) and dry areas (mineral dust) and by human activities (industries, traffic, domestic heating, agricultural burning, etc.). Generally, the variability of natural aerosols such as dust is large and has high seasonality. Anthropogenic aerosols are more localized but can have significant temporal variability as well. In CAMSiRA, the anthropogenic emissions of black carbon, organic matter, and sulfur dioxide were taken from the MACCity inventory (Granier et al. 2011). Open fire emissions were provided by the Global Fire Assimilation System (GFAS) inventory (Kaiser et al. 2012) that estimates fire emissions from MODIS observations of fire radiative power. These emissions are similar between the NRT analysis and the CAMSiRA. Dust and sea salt aerosol emissions are computed dynamically as a function of wind speed.

Time series of globally averaged total AOD during 2003–17 (Fig. 2.49) show strong seasonality, with yearly maxima in March–April and August–September driven mainly by dust episodes primarily in spring and summer in the Sahara, Middle East,

and Taklimakan/Gobi deserts and seasonal biomass burning in Africa, South America, and Indonesia.

Overall, the 2017 anomalies of biomass burning aerosols are consistent with those of tropospheric ozone (Section 2g6), carbon monoxide (Section 2g7), and fires (Section 2h3). Seasonal burning was, in general, less severe than usual in 2017 in the main regions that are subject to large seasonal fires: Indonesia, the Amazon Basin, and parts of south equatorial Africa. Negative anomalies in 2016 and 2017 over Indonesia may be explained by meteorological conditions as well as the government policies regarding land use following the El Niño event of 2015 which contributed to severe drought and extreme fires in this region in 2015. Large but isolated biomass burning events in 2017 are associated with positive anomalies in Chile (January 2017), Siberia (June 2017), and western Canada—where British Columbia experienced the worst fires in its recent history during July–August 2017 (Plate 2.1ab, Section 7b).

Global maps of the 2003–17 average total AOD and statistically significant (95% confidence) linear trends over the period are shown in Fig. 2.50. The highly polluted areas of eastern Asia and India remain prominent features in the total AOD map, as are the dust-producing regions of the Sahara, Arabia, the Middle East, and the Taklamakan and Gobi deserts (Fig. 2.50a). Large AOD values over equatorial Africa are caused by seasonal biomass burning. The linear trend highlights the long-term decrease in anthropogenic aerosols over the eastern U.S., Europe, Japan, and parts of southern China, while a significant increase occurred over most of the Indian subcontinent, possibly linked to increased industrial activity and, hence, increased emissions in the area. The area of decreasing trends in the southern Amazon Basin is associated with reduced deforestation there (Chen et al. 2013). The decreasing trends over the northern Sahara and western Mediterranean indicate lower frequencies or intensities of dust episodes in these regions or less transport; these were already present in 2016 so are not attributable to model changes. The positive trends over the Southern Ocean may be an artifact of the CAMS interim reanalysis in 2017 and 2016.

Radiative forcing resulting from aerosol–radiation (RF<sub>ari</sub>) and aerosol–cloud interactions (RF<sub>aci</sub>) for the period 2008–17 is shown in Fig. 2.51, as estimated using the methods described in Bellouin et al. (2013) using CAMSiRA data. Negative radiative forcings imply a cooling effect of the aerosols on the climate. Due to a relatively large contribution of anthropogenic aerosols to total aerosol optical depth, 2017 has been a

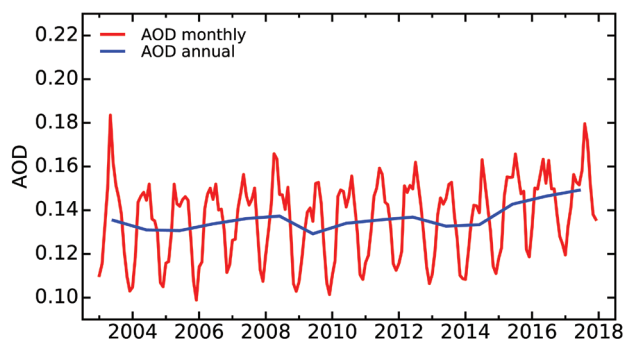


**FIG. 2.49.** Global average of total AOD at 550 nm averaged over monthly (red) and annual (blue) periods for 2003–17.



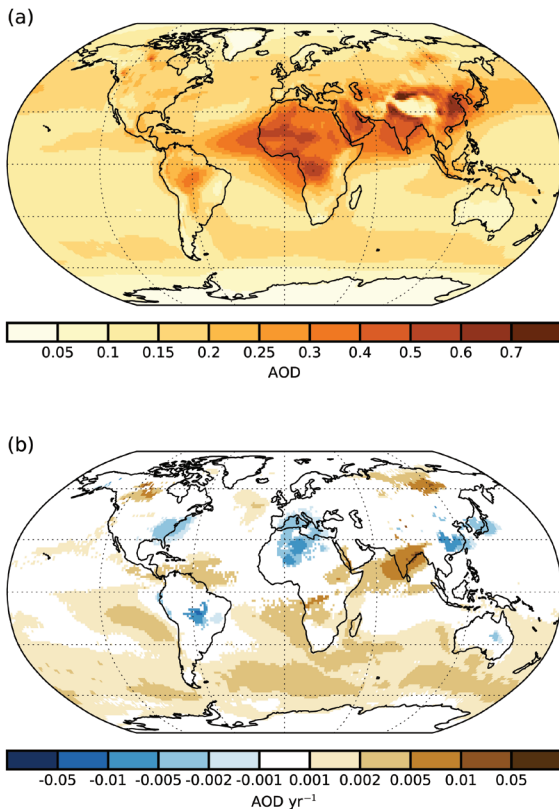


**FIG. 2.50. (a) Total 550-nm AOD averages for 2003–17. Note the regional differences, with much greater total AOD values over parts of northern Africa, the Arabian Peninsula, southern Asia, and eastern China. (b) Linear trends of total AOD (AOD yr<sup>-1</sup>) for 2003–17. Only trends that are statistically significant (95% confidence) are shown.**

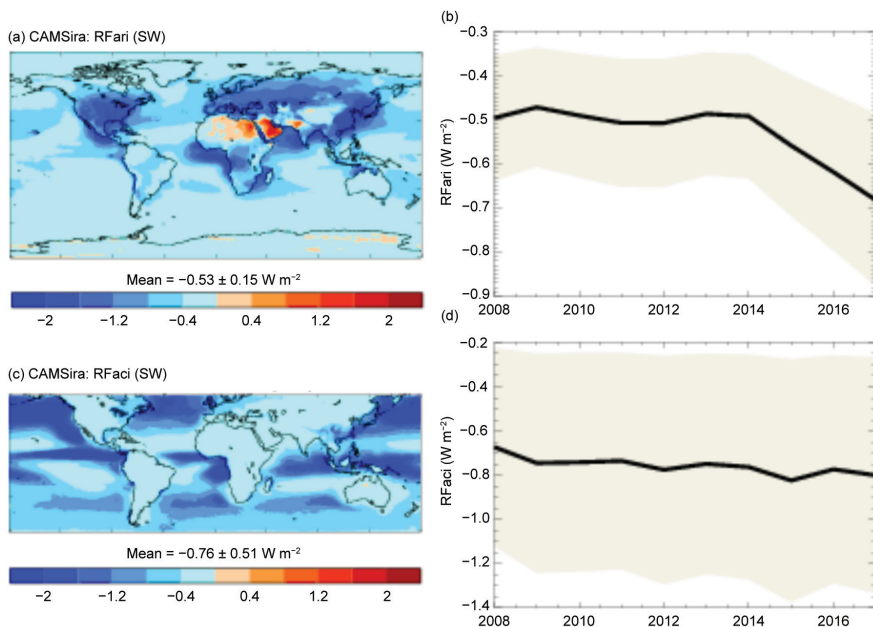


**FIG. 2.51. Radiative forcing (W m<sup>-2</sup>) in the SW spectrum resulting from (a) RFari and (c) RFaci from 2008–17. (b,d) The uncertainties of these estimates are shown in gray.**

strong year in terms of aerosol radiative forcing, with the third consecutive increase in RFari, estimated to be  $-0.68 \text{ W m}^{-2}$  in 2017, stronger than the  $-0.55 \text{ W m}^{-2}$  estimated for 2015. The increase may be linked to increased biomass-burning aerosols in the tropics. Trends remain statistically fragile, however, because of large uncertainties in the estimates. Absorbing anthropogenic aerosols exert positive RFari over bright surfaces, like the African and Arabian deserts, as shown in the upper panel of Fig. 2.51. RFaci, estimated at  $-0.8 \text{ W m}^{-2}$  in 2017, was comparable to 2015 ( $-0.82 \text{ W m}^{-2}$ ) and 2016 ( $-0.77 \text{ W m}^{-2}$ ).

- 4) STRATOSPHERIC OZONE—M. Weber, W. Steinbrecht, R. van der A, S. M. Frith, J. Anderson, M. Coldewey-Egbers, S. Davis, D. Degenstein, V. E. Fioletov, L. Froidevaux, D. Hubert, J. de Laat, C. S. Long, D. Loyola, V. Sofieva, K. Tourpali, C. Roth, R. Wang, and J. D. Wild

Throughout nearly the entire Southern Hemisphere annual mean total column ozone levels in 2017 were above the mean from the 1998–2008 reference period (Plate 2.1y). In particular, the Antarctic region showed values that were more than 10 DU (Dobson units) above the long-term mean (see also October mean in Fig. 2.52e). The main cause was the weak polar vortex (stratospheric cyclone) observed in southern winter/spring resulting in below-average polar ozone losses and a rather small ozone hole in size and depth (see Section 6h). In the second half of 2017 the quasi-biennial oscillation (QBO) was in the east phase (easterly flow in the tropical lower stratosphere), which had a global impact on the stratospheric circulation. During the QBO east phase planetary waves are deflected toward the pole (SH winter in 2017) and weaken the polar vortex (Baldwin et al. 2011). Associated with these planetary waves is an enhanced meridional or Brewer–Dobson circulation transporting more ozone into middle to high latitudes which, in addition to reduced polar losses, contributed to the overall SH increase (e.g., Salby 2008; Weber et al. 2011). In the Northern Hemisphere total ozone was generally near

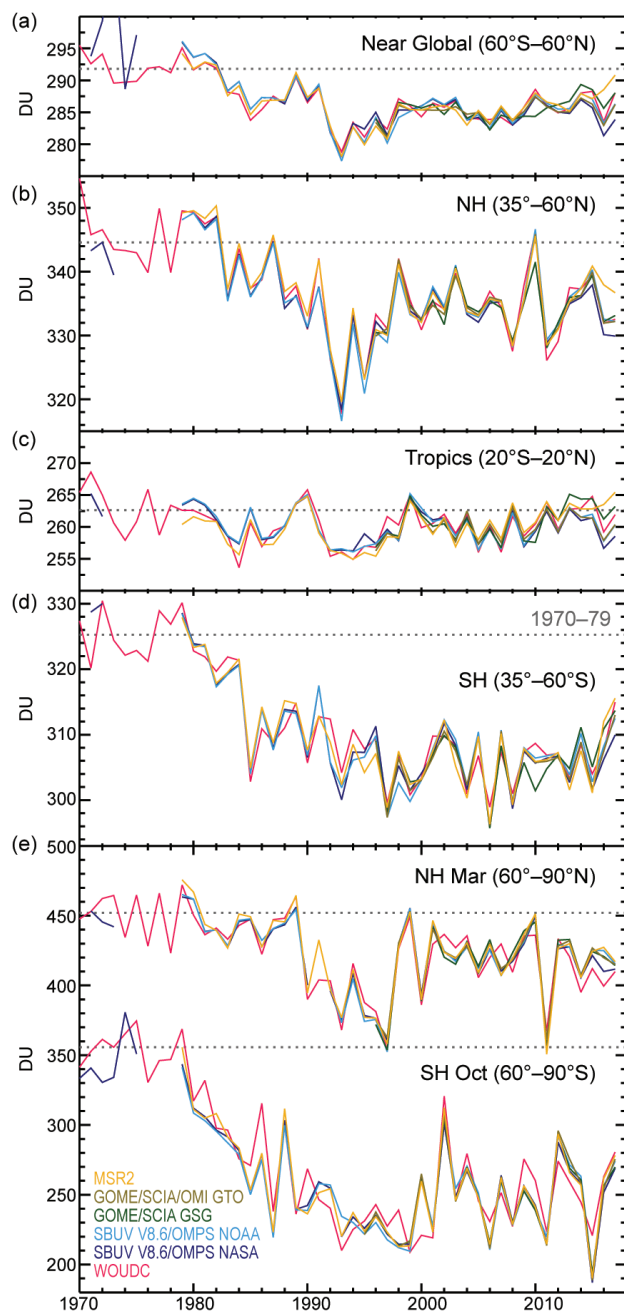


**FIG. 2.52.** Time series of annual mean total ozone (DU) in (a)–(d) four zonal bands, and (e) polar ( $60^{\circ}$ – $90^{\circ}$ ) total ozone in Mar (NH; see also Section 5j) and Oct (SH), the months when polar ozone losses usually are largest. Data are from WOUDC (World Ozone and Ultraviolet Radiation Data Centre) ground-based measurements combining Brewer, Dobson, SAOZ, and filter spectrometer data (Fioletov et al. 2002, 2008); the BUV/SBUV/SBUV2 V8.6/OMPS merged products from NASA (MOD V8.6, Frith et al. 2014, 2017) and NOAA (Wild and Long 2018, manuscript in preparation); the GOME/SCIAMACHY/GOME-2 products from University of Bremen (Weber et al. 2011; Weatherhead et al. 2017) and GTO from ESA/DLR (Coldewey-Egbers et al. 2015; Garane et al. 2018). MSR-2 assimilates nearly all ozone datasets after corrections with respect to the ground data (van der A et al. 2015). All six datasets have been bias corrected by subtracting averages from the reference period 1998–2008 and adding the multiple data mean from the same period. The horizontal dotted gray lines in each panel show the average ozone level for 1970–79 calculated from the WOUDC data. All data from 2017 are preliminary.

average in 2017 with some regions with slightly lower ozone (Plate 2.1y).

Figure 2.52 shows the annual mean total ozone time series from various merged datasets in the tropics, extratropics, and selected months in the polar regions as well as the near-global ( $60^{\circ}\text{N}$ – $60^{\circ}\text{S}$ ) average. For all time series, the average ozone levels from the 1970s, a time when ozone losses due to ozone-depleting substances were still very small, are also shown. Except for the tropics, total ozone levels have not yet recovered to the values from the 1970s. A recent study indicates that total ozone trends since the late 1990s are positive ( $<1\%$  decade $^{-1}$ ) but only reach statistical significance at a few latitudes (Weber et al. 2018). The small increase in global total ozone following the significant decline before the 1990s is regarded as proof that the Montreal Protocol and its Amendments, signed thirty years ago and responsible for phasing out ozone-depleting substances (ODS), works.

ODS currently decrease at about one-third of the absolute increasing rate before the 1990s, but the recent increase in total column ozone is in comparison smaller than expected from the ODS change. Model studies show that the predicted ozone evolution is consistent in most regions outside the tropics with ODS changes and observed stratospheric ozone and total column observations (Shepherd et al. 2014; Chipperfield et al. 2017). The lack of observed ODS-related changes in tropical total ozone (but observed in climate models with stratospheric chemistry) may be due to a compensation by increases in tropospheric ozone that contribute to the total column (Shepherd et al. 2014). However, observed global tropospheric ozone trends from various studies are highly variable and often insignificant (Gaudel et al. 2018 and Figure 26 therein).

Ball et al. (2018) suggest, based on an analysis of satellite measurements, that a near-continuous, near-global ( $< 60^{\circ}$  in both hemispheres) decline in lower stratospheric ozone since 1998 was compensated by observed upper stratospheric increases and tropospheric increases, resulting in rather small total ozone trends. A recent chemistry-transport model study by Chipperfield et al. (2018) shows that the observed

lower stratospheric and total column ozone changes are mostly explained by variability in atmospheric dynamics and is not contradicting our current understanding of stratospheric ozone chemistry related to ODS changes as otherwise suggested by Ball et al. (2018). In the tropics a continuous decline in total ozone in the future is predicted by chemistry-climate models as climate change will enhance tropical upwelling and potentially thin ozone in the lowermost tropical stratosphere, thus increasing UV radiation in the equatorial region (WMO 2014; Chipperfield et al. 2017).

While the expected slow recovery of stratospheric ozone has not yet resulted in substantial increases of total column ozone, ozone in the upper stratosphere has been showing clearer signs of increase and recovery over the last 10 to 15 years (WMO 2014;

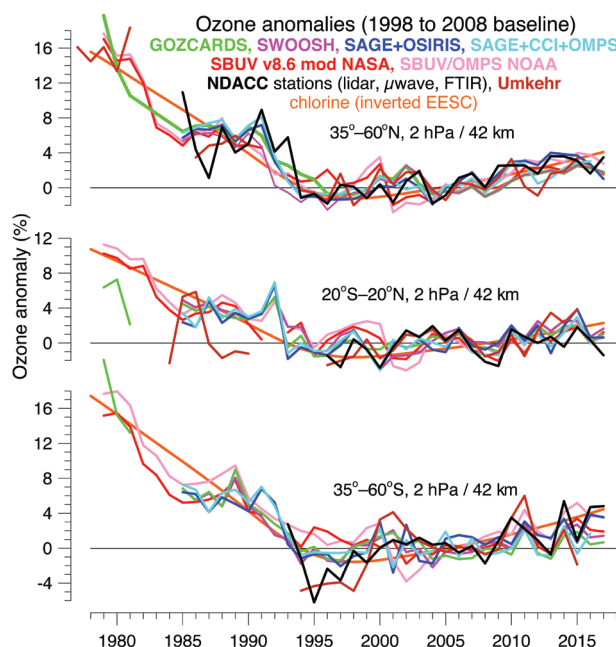


**FIG. 2.53. Annual mean anomalies of ozone (%) (1998–2008 baseline) in the upper stratosphere, near 42-km altitude or 2-hPa pressure for three zonal bands: 35°–60°N (NH), 20°N–20°S (tropics), and 35°–60°S (SH). Colored lines are for long-term records obtained by merging different limb (GOZCARDs, SWOOSH, SAGE+OSIRIS, SAGE+CCI+OMPS-LP) or nadir viewing (SBUV, OMPS-NP) satellite instruments. Black line is from merging ground-based ozone records at NDACC stations employing differential absorption lidars, microwave radiometers, and/or Fourier Transform InfraRed spectrometers (FTIRs). Gray line is for ground-based Umkehr measurements. See Steinbrecht et al. (2017) for details on the various datasets. Orange line gives inverted EESC as a proxy for man-made ozone depletion. Ozone data for 2017 are not yet complete for all instruments and are still preliminary.**

Steinbrecht et al. 2017). Figure 2.53 shows that since about 2000, ozone has generally been increasing in the upper stratosphere, ending the previous period of ozone decline. In 2017, ozone values in the upper stratosphere were below the EESC curve both in the tropical belt and at northern midlatitudes. This is somewhat surprising for the easterly phase of the QBO and may in part arise from the decadal

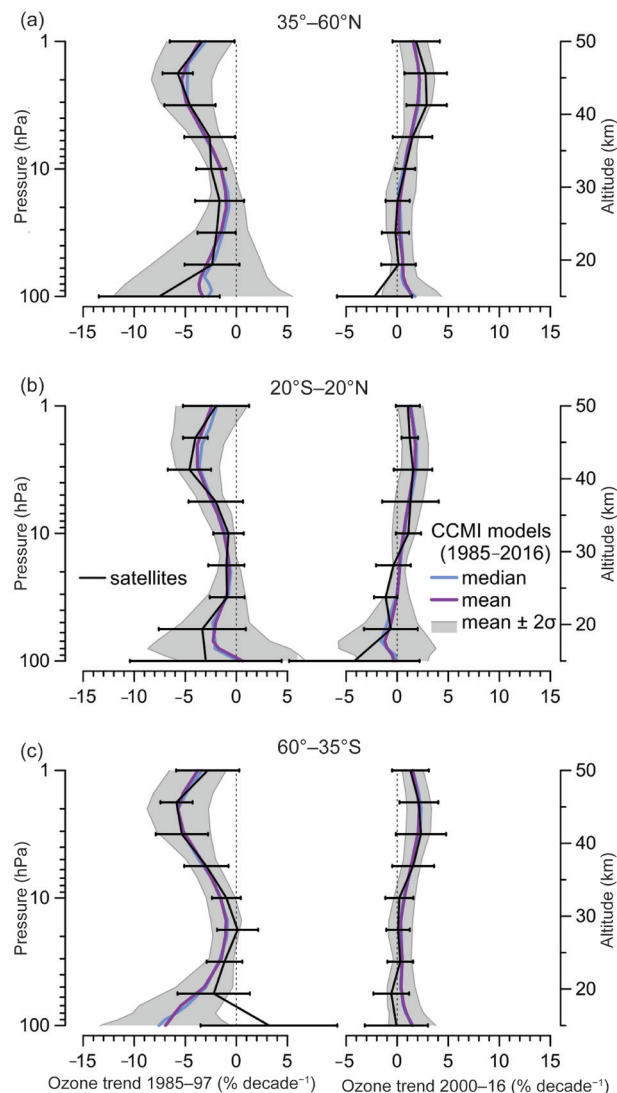


**FIG. 2.54. Mean ozone trends in the upper atmosphere (% decade<sup>-1</sup>) prior to 1997 and after 2000 as derived from the CCMI REF-C2 models' simulation (median in blue and mean in purple) and satellite data (black line) in three zonal bands: (a) 35°–60°N (NH), (b) 20°N–20°S (tropics), and (c) 35°–60°S (SH). Mean trends were averaged from trends of individual model runs and various merged datasets shown in Fig. 2.53. The shading shows the 2σ of the models' mean trend. Same type of multilinear regression analysis was used to determine the trends in models and observations. Adapted from LOTUS (2018, SPARC report under review).**



minimum of solar activity (e.g., Randel and Wu 1996; Newchurch et al. 2003; WMO 2014).

It is a challenge to accurately attribute observed stratospheric ozone changes, because changes due to recovery are expected to be small and thus potentially masked by long-term natural variability and measurement uncertainty. Substantial efforts, therefore, have gone into improving the available observational ozone profile records and into better ways to estimate ozone profile trends and their uncertainties (LOTUS 2018, *SPARC report* under review). Figure 2.54 shows the resulting updated trend profiles from observations and chemistry-climate models, both during the phase of ODS-driven ozone decline from the late 1970s to the late 1990s, and during the beginning recovery phase from 2000 to 2016. Observations are in generally good agreement with chemistry-climate model simulations.

As a result of the Montreal Protocol and its Amendments, ODS have been declining in the stratosphere since the late 1990s. The model simulations predict that ozone in the upper stratosphere should now increase by 2%–3% decade<sup>-1</sup>, due to both declining ODS and stratospheric cooling, the latter caused by increasing greenhouse gases (WMO 2014). The right panels of Fig. 2.54 demonstrate that ozone increases are observed in the upper atmosphere after 2000, although they are not statistically significant at all latitudes and altitudes. Nevertheless, the good agreement between model simulations and observations gives confidence that ozone trends in the upper stratosphere are well understood and that ozone in that region is on its continuing (slow) path towards recovery.

#### 5) STRATOSPHERIC WATER VAPOR—S. M. Davis, K. H. Rosenlof, D. F. Hurst, H. B. Selkirk, and H. Vömel

Stratospheric water vapor (SWV) is a radiatively important gas that can also impact stratospheric ozone chemistry. The second consecutive year of dramatic changes in lower SWV occurred in 2017. Following 2016, during which the tropical mean (15°N–15°S) water vapor anomaly in the lowermost stratosphere (at 82 hPa) dropped from a near record high in January (+0.5 ppm, parts per million mole fraction, equivalent to  $\mu\text{mol mol}^{-1}$ ) to a record low by December (–1 ppm), 2017 anomalies increased to near record high values by midyear.

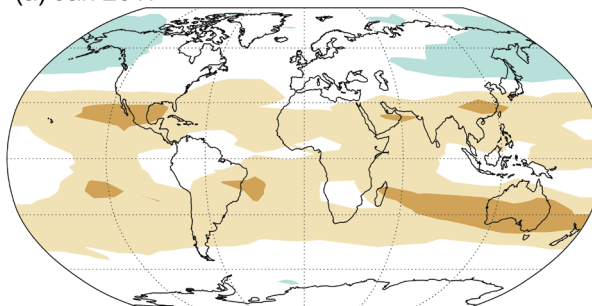
In January 2017 negative (dry) anomalies were observed in the tropics and subtropics, in stark contrast to the strong positive (wet) anomalies of June 2017. From January to June 2017, the tropical SWV anomaly in the lower stratosphere increased by 0.9 ppm (Figs.

2.55, 2.56c,d), about 40% of the average seasonal cycle amplitude at 82 hPa in the tropics and 140% of the climatological average difference between these two months. This steep increase in tropical lowermost SWV during the first half of 2017 and subsequent return to near-normal values by the end of the year were observed by both the *Aura* Microwave Limb Sounder (MLS) satellite instrument (Fig. 2.55) and balloon-borne frost point hygrometer soundings at tropical sites Hilo, Hawaii (20°N), and San José, Costa Rica (10°N) (Figs. 2.56c,d).

Variations in cold-point temperatures (CPTs) in the tropical tropopause layer (TTL) on annual and interannual timescales provide the dominant control on water vapor entering into the lowermost stratosphere in the tropics by freeze-drying tropospheric air during its slow ascent through the TTL. Thus, seasonal to interannual variability in tropical SWV around 82 hPa is highly correlated with CPT variations. The dramatic swing in tropical lower SWV during 2017 is consistent with the substantial 2.5°C increase from November 2016 to May 2017 and subsequent 1.5°C decrease in tropical CPT anomalies over the remainder of 2017 (Fig. 2.56d).

Interannual variations in CPTs are partially related to interannual variability in the phases of ENSO

(a) Jan 2017



(b) Jun 2017

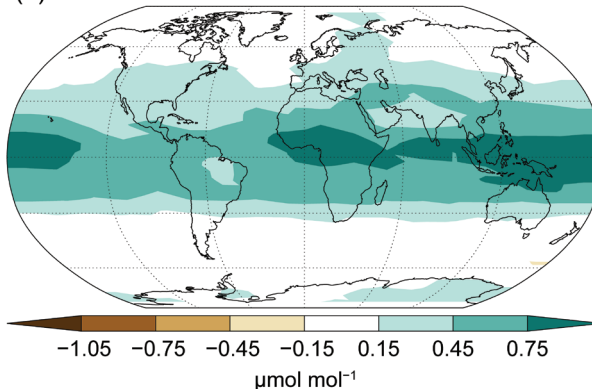


**FIG. 2.55. Global stratospheric water vapor anomalies ( $\mu\text{mol mol}^{-1}$ ; 2004–17 base period) centered on 82 hPa in (a) Jan and (b) Jun 2017 from the *Aura* MLS.**

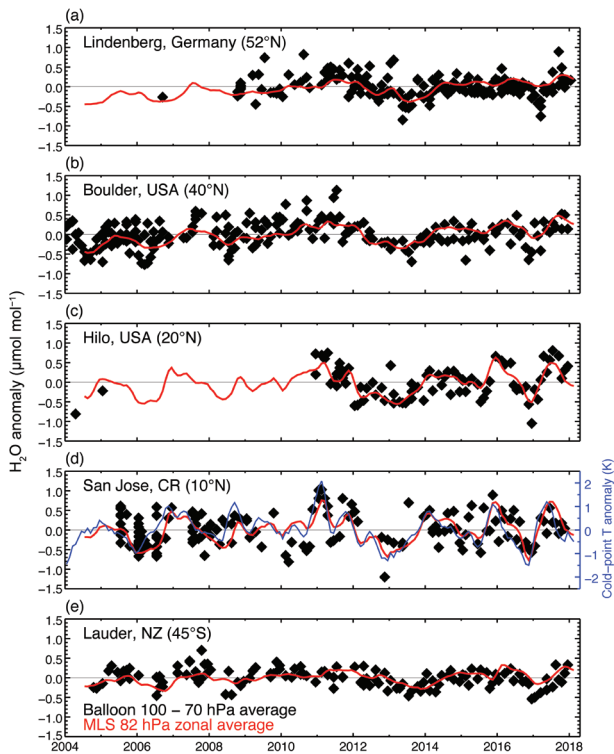


**FIG. 2.56. Lower stratospheric water vapor anomalies ( $\mu\text{mol mol}^{-1}$ ) over five balloon-borne frost point (FP) hygrometer stations. Each panel shows the lower stratospheric anomalies of individual FP soundings (black squares) and of monthly zonal averages of MLS retrievals at 82 hPa in the  $5^\circ$  latitude band containing the FP station (red lines). High-resolution FP vertical profile data were averaged between 70 and 100 hPa to emulate the MLS averaging kernel for 82 hPa. Each MLS monthly zonal mean was determined from 2000–3000 profiles. Anomalies for MLS and FP data are calculated relative to the 2004–17 period for sites except for Lindenberg (2009–17) and Hilo (2011–17). Tropical CPT anomalies (K) based on the MERRA-2 reanalysis (d, blue curve), which were generally well correlated with the tropical lower SWV anomalies, are the driving force behind the variations in tropical SWV during 2017.**

and the quasi-biennial oscillation (QBO) in tropical stratospheric winds (Dessler et al. 2014). During 2017, the QBO was in a westerly (warm) phase at 70 hPa, and ENSO was in a neutral state. It is possible that suppressed tropical upwelling due to the QBO westerly phase led to the warm CPT anomalies and positive (wet) SWV anomalies in the tropical lower stratosphere in the first half of 2017.

Water vapor entering the tropical lowermost stratosphere is transported vertically in a quasi-coherent fashion, forming the well-known “tropical tape recorder” phenomenon (Fig. 2.57a; Mote et al. 1996). In the tropical middle stratosphere, the water vapor abundance is indicative of how much

entered the stratosphere in the previous year and was subsequently transported upward. During late 2017, the tropical SWV anomalies at 30 hPa were negative (dry), due to the anomalously cold CPTs and correspondingly dry water vapor anomalies that entered the stratosphere in the latter half of 2016 and beginning of 2017.

In general, lowermost SWV anomalies propagate quasi-isentropically from the tropics to the middle latitudes of both hemispheres, as is demonstrated by the “C”-shaped contours in Fig. 2.57b. The early 2017 dry anomaly and the mid-2017 wet anomaly in tropical lower SWV can be seen a few months later in the middle latitudes of each hemisphere. These midlatitude anomalies are also observed by balloon measurements at Lindenberg, Germany ( $52^\circ\text{N}$ ); Boulder, Colorado ( $40^\circ\text{N}$ ); and Lauder, New Zealand ( $45^\circ\text{S}$ ) (Fig. 2.56a,b,e).

SWV anomalies over Lauder, New Zealand (Fig. 2.56e) increased during most of 2017, consistent with the poleward transport of the strong wet anomalies in SWV present in the tropics during mid-2017. SWV in the Southern Hemisphere midlatitudes can also

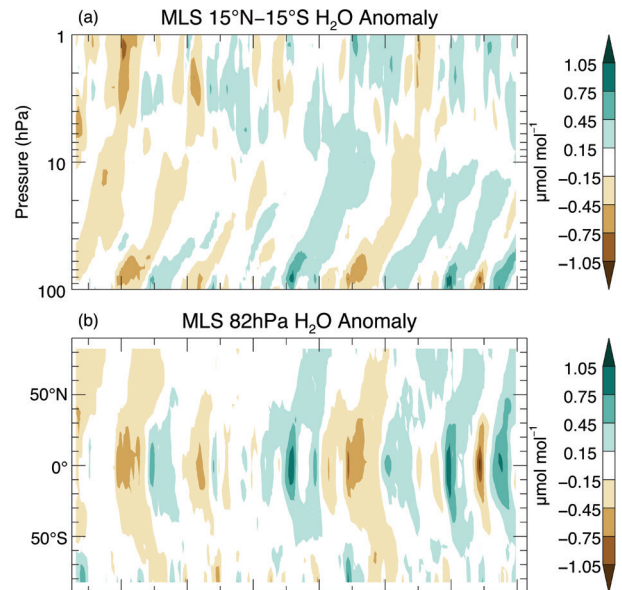


**FIG. 2.57. (a) Time series of vertical profiles of tropical ( $15^\circ\text{S}$ – $15^\circ\text{N}$ ) stratospheric water vapor anomalies ( $\mu\text{mol mol}^{-1}$ ) and (b) latitudinal distributions of SWV anomalies ( $\mu\text{mol mol}^{-1}$ ) at 82 hPa. Both are based on Aura MLS data. Anomalies are differences from the mean 2004–17 water vapor mixing ratios for each month. In panel (b) propagation of tropical lower SWV anomalies to higher latitudes in both hemispheres as well as the influences of dehydrated air masses from the Antarctic polar vortex as they are transported towards the SH midlatitudes at the end of each year are clearly seen.**

be influenced by the springtime (October–November) northward transport of air masses that were dehydrated within the Antarctic vortex. The weak anomalies at high southern latitudes in late 2017 (Fig. 2.56b) indicate that the Antarctic dehydration in 2017 was not unusual. Therefore, the positive anomalies observed at Lauder in late 2017 are primarily attributed to the southward transport of the strong tropical wet anomalies.

#### 6) TROPOSPHERIC OZONE—J. R. Ziemke and O. R. Cooper

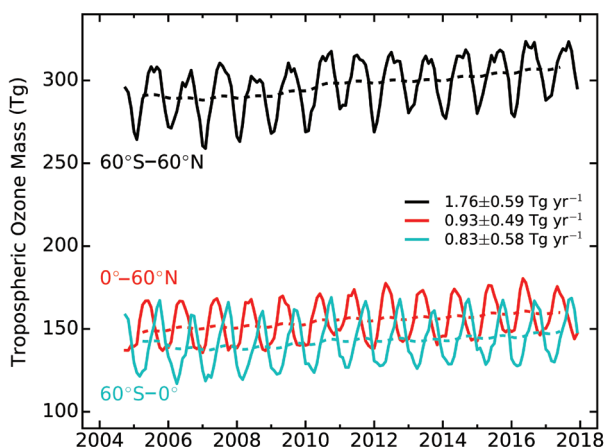
Tropospheric ozone is a surface pollutant, a greenhouse gas, and the dominant source of the hydroxyl radical (OH), which is the troposphere’s primary oxidizing agent. Sources include transport from the stratosphere along with photochemical production from a number of precursor gases such as lightning-generated  $\text{NO}_x$ , methane, biogenic hydrocarbons, and emissions generated from combustion of fossil fuels and biomass burning (e.g., Sauvage et al. 2007; Leung et al. 2007; Martin et al. 2007; Murray et al. 2013; Young et al. 2013; Monks et al. 2015; Zhang et al. 2016; Lin et al. 2017). Tropospheric ozone is highly variable from small (urban) to large (hemispheric) scales due to variations in dynamical transport and photochemical production (i.e., heterogeneity of precursor gas emissions and sunlight) and sinks including loss mechanisms such as through  $\text{HO}_x$  photochemistry and through surface deposition (IPCC 2014). Transport phenomena that drive large-scale variability include the El Niño–Southern Oscillation (e.g., Chandra et al. 1998, 2009; Sudo and Takahashi 2001; Doherty et al. 2006; Koumoutsaris et al. 2008) and the Madden–Julian Oscillation (e.g., Sun et al. 2014; Ziemke et al. 2015). Relatively short lifetimes for ozone and ozone precursors and short-term variability of transport including convection drives much of the variability of tropospheric ozone on short timescales including day-to-day changes. Variability from daily to interannual timescales adds challenges to quantifying decadal trends at hemispheric and global scales (e.g., Neu et al. 2014; M. Lin et al. 2014; Barnes et al. 2016).

The tropospheric ozone summary in the *State of the Climate in 2012* was based on measurements by ground- and satellite-based instruments (Cooper and Ziemke 2013). Since then the reports have primarily relied on the *Aura* Ozone Monitoring Instrument/Microwave Limb Sounder (OMI/MLS) satellite measurements (Ziemke et al. 2006, 2015) because of insufficient updates of global ground-based observations (Cooper and Ziemke 2014, 2015; Ziemke and Cooper 2016, 2017). The Tropospheric Ozone Assessment

Report (TOAR) further discusses the global ground network including update issues (Schultz et al. 2017; see Sidebar 2.2). The present update again relies mostly on OMI/MLS satellite data.

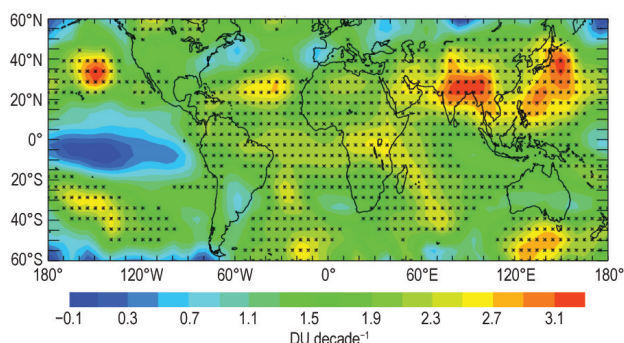
Plate 2.1x shows broad regions of positive anomalies (relative to the 2005–16 average) of up to 1.2 DU (4%) in tropospheric ozone columns for 2017 in the Northern Hemisphere lower midlatitudes and smaller anomalies of  $\sim 1$  DU or less elsewhere. Hemispheric and global average tropospheric ozone burdens and their 95% confidence level precision uncertainties for 2017 were  $159 \pm 6$  Tg for  $0^\circ$ – $60^\circ\text{N}$ ,  $147 \pm 8$  Tg for  $0^\circ$ – $60^\circ\text{S}$ , and  $306 \pm 7$  Tg for  $60^\circ\text{N}$ – $60^\circ\text{S}$  (Fig. 2.58). Each of these 2017 averages represents an increase from previous years, continuing the long-term positive trend. Linear trends in hemispheric and global burdens from October 2004 through December 2017 in Fig. 2.58 all depict increases of  $\sim 0.6\%$  to  $0.7\%$   $\text{yr}^{-1}$ .

Figure 2.59 shows the spatial distribution of tropospheric ozone trends on a  $5^\circ \times 5^\circ$  grid for October 2004 to December 2017. All trends with statistical significance depict increases, the strongest of which



**FIG. 2.58. Monthly averages of OMI/MLS tropospheric ozone burdens (Tg) from Oct 2004 through Dec 2017.** Top curve (solid black line) shows  $60^\circ\text{S}$ – $60^\circ\text{N}$  monthly averages with 12-mo running means (dashed black line). Bottom two curves show monthly averages and running means for the NH (red) and SH (blue). Slopes of linear fits to the data are presented with their 2-sigma uncertainties. All three trends are statistically significant at the 95% confidence level. Prior to our analyses, the data were evaluated for potential offset and drift by comparison with globally distributed ozonesonde profiles and OMI convective cloud differential (CCD) measurements (Ziemke et al. 1997). A small drift of about  $+0.5$  DU  $\text{decade}^{-1}$  was found and an appropriate correction was applied to the OMI/MLS data. OMI/MLS tropospheric ozone was also adjusted everywhere by  $+2$  DU to correct for mean offset relative to the ozonesondes.





**FIG. 2.59. Linear trends in OMI/MLS tropospheric column ozone (DU decade<sup>-1</sup>) on a 5° × 5° grid for Oct 2004–Dec 2017. Asterisks denote statistically significant trends at the 95% confidence level. Note that trends were calculated using a multivariate linear regression model (Ziemke et al. 1998, and references therein) that included a seasonal cycle fit and the Niño-3.4 index as an ENSO proxy; trend uncertainties included autoregressive adjustment via Weatherhead et al. (1998).**

[~+3.3 DU decade<sup>-1</sup> (+1.05% yr<sup>-1</sup>)] are located above India, Southeast Asia, and extend eastward across the North Pacific Ocean. These upward trends are consistent with model estimates based on strengthening emissions of ozone precursors from Southeast, East, and South Asia, primarily due to fossil fuel combustion (Zhang et al. 2016; Lin et al. 2017). The model simulations indicate that ozone produced in these densely populated areas is transported eastward in the free troposphere over the North Pacific Ocean as suggested in Fig. 2.59. Positive trends are also found

above the North Atlantic Ocean, the equatorial Africa and Atlantic/Indian Oceans regions, and the Southern Hemisphere extratropics.

As noted above, updating global surface ozone measurements annually is difficult because most ground stations do not provide quality-assured final data soon enough for the timing of this report. However, there are three remote monitoring sites with rapidly updated data: 1) the high-elevation Mauna Loa Observatory (MLO), Hawaii (19.5°N, 155.6°W, 3397 m asl); 2) South Pole Observatory (SPO), Antarctica (90°S, 59°E; 2840 m asl); and 3) Utqiagvik (Barrow), Alaska (71.3°N, 156.6°W; 11 m asl). Continuous UV-based measurements of ozone began at MLO in September 1973, at SPO in January 1975, and at Barrow in March 1973. Reliable ozone observations based on the Regener automatic wet-chemical method are also available at SPO for 1961–63 (Oltmans and Komhyr 1976), and at MLO for 1957–59 (Price and Pales 1963). These time series, the world's longest at remote locations, are reported in Fig. 2.60 as monthly medians, based on all 24 hours of the day at SPO and Barrow, but the MLO data are restricted to nighttime values when local winds are downslope, ensuring that the observations are representative of the lower free troposphere. The limited data at MLO and SPO from the 1950s and 1960s indicate that ozone levels at these remote high-elevation sites were similar during the mid-20th century despite being located in different hemispheres. Ozone at SPO has changed little since the 1960s with no significant trend. In contrast,

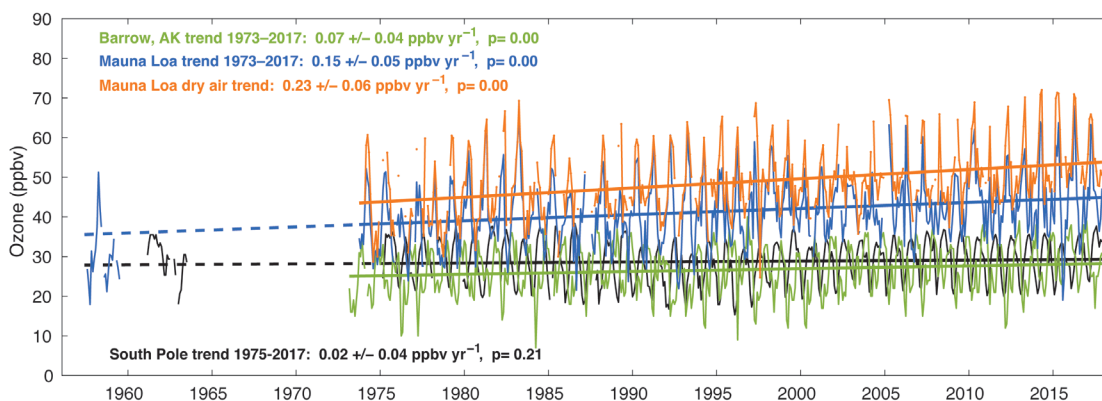


**FIG. 2.60. Monthly median surface ozone at Utqiagvik (Barrow), Alaska (Mar 1973–Dec 2017; green) and South Pole (Jan 1975–Dec 2017; black) using data from all hours of the day. Additional data from South Pole are shown for the early 1960s. Also shown are nighttime monthly median ozone values at the Mauna Loa Observatory (MLO) calculated with all available data for months with at least 50% data availability, Sep 1973–Dec 2017 (blue), with early observations from the late 1950s. Monthly median values associated with dry air masses (orange) at MLO are also included (dew point less than the climatological monthly 40th percentile, and a sample size of at least 24 individual hourly nighttime observations). Trends (solid straight lines) are based on least-squares linear regression fit through the monthly values (1970s–2017), and reported with 95% confidence intervals and *p*-values. MLO and South Pole trend lines are extrapolated back in time to the late 1950s (dashed lines).**

## SIDEBAR 2.2: THE TROPOSPHERIC OZONE ASSESSMENT REPORT (TOAR)—O. R. COOPER

Recognizing the need for a comprehensive tropospheric ozone survey and the challenges associated with gathering and processing ozone observations from thousands of sites worldwide, the International Global Atmospheric Chemistry (IGAC) Project developed the Tropospheric Ozone Assessment Report (TOAR): Global metrics for climate change, human health, and crop/ecosystem research, released in October 2017. Initiated in 2014, TOAR's mission is to provide the research community with an up-to-date scientific assessment of tropospheric ozone's global distribution and trends from the surface to the tropopause. TOAR's primary goals are: (1) produce the first tropospheric ozone assessment report based on all available surface observations, the peer-reviewed literature, and new analyses; and (2) generate easily accessible and documented ozone exposure metrics at thousands of measurement sites around the world. TOAR is an international collaborative effort with participation from over 230 scientists and air quality experts from 36 nations representing research on all seven continents.

Monitoring global trends of long-lived greenhouse gases such as carbon dioxide and methane is relatively straightforward as their spatial and temporal variability is limited and relatively few measurement sites are required to demonstrate global-scale changes. Quantification of global ozone trends is much more difficult due to ozone's short lifetime (days to weeks) and multiple sources and sinks that have heterogeneous spatial distributions and seasonal cycles. While over 5000 surface ozone monitoring sites are presently established worldwide, their distribution is uneven with high densities in North America, Europe, and East Asia, and few or no sites in South Asia, the Middle East, Central Asia, Africa, and South and Central America. Monitoring is also limited across the oceans and the polar regions. Another barrier to producing a global survey of surface ozone trends is the logistical problem of gathering the data from dozens of air quality agencies and research groups across many nations, all with different data formats.

To produce a wide range of ozone metrics at thousands of surface sites worldwide, TOAR built the world's largest database of surface hourly ozone observations (Schultz et al. 2017). Through

the TOAR database these ozone metrics are freely accessible for research on the global-scale impact of ozone on human health, crop/ecosystem productivity, and climate. All ozone data submitted to the database have undergone quality control procedures by the agencies or research groups that made the observations. The site locations are then cross-referenced with global gridded datasets of human population, satellite-detected tropospheric nitrogen dioxide ( $\text{NO}_2$ ), a bottom-up  $\text{NO}_x$  emissions inventory, satellite-detected night-time lights of the world, and land cover so that all sites can be objectively queried to determine if they meet predetermined criteria for urban or rural classifications. The database is publicly available and the ozone metrics can be downloaded from: <https://doi.pangaea.de/10.1594/PANGAEA.876108>.

The particular ozone metrics available from the database were chosen for their relevance to research (Lefohn et al. 2018) related to human health (Fleming and Doherty et al. 2018), vegetation (Mills et al. 2018, manuscript submitted to *Elementa*), and climate (Gaudel et al. 2018). The metrics are also being used to evaluate global atmospheric chemistry models (Young et al. 2018), to assess long-term global ozone trends from the early 20th century to the present (Tarasick et al. 2018, manuscript submitted to *Elementa*), and to develop new statistical methods for quantifying regional ozone trends (Chang et al. 2017).

An illustration of the database's capabilities is provided in Fig. SB2.3 which shows the warm season (April–September in the Northern Hemisphere and October–March in the

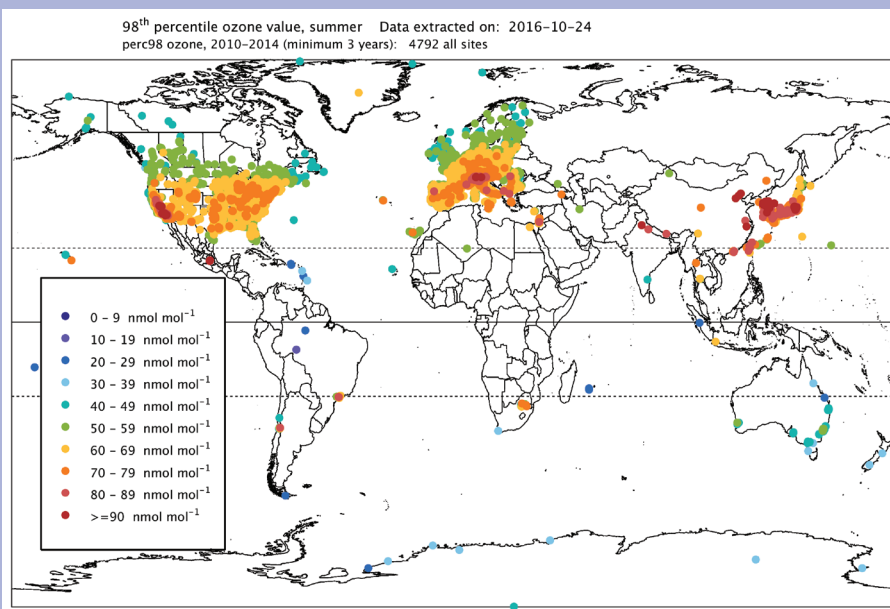


**FIG. SB2.3.** 98th percentile ozone ( $\text{nmol mol}^{-1}$  equivalent to ppb) at all available (4792) surface sites for the 2010–14 warm season (Apr–Sep in the NH, and Oct–Mar in the SH).

Southern Hemisphere) surface ozone 98th percentile value at all available stations, averaged across the period 2010–14. The data quickly reveal that the most extreme ozone events are found in Southern California, Mexico City, northern Italy, northern India, eastern China, South Korea, and Japan. Ozone monitoring is sparse in the Southern Hemisphere, but in general concentrations are much lower. Figure SB2.4 depicts the trends of the 98th percentile surface ozone at all available stations showing widespread decreases across North America and much of Europe in response to emission controls of ozone precursor gases (oxides of nitrogen, carbon monoxide, volatile organic compounds). In contrast, high ozone events increased in Hong Kong, South Korea, and parts of western Japan due to broad, regional scale ozone precursor emission increases.

Further information on TOAR can be found on the IGAC webpage: [www.igacproject.org/activities/TOAR/](http://www.igacproject.org/activities/TOAR/)

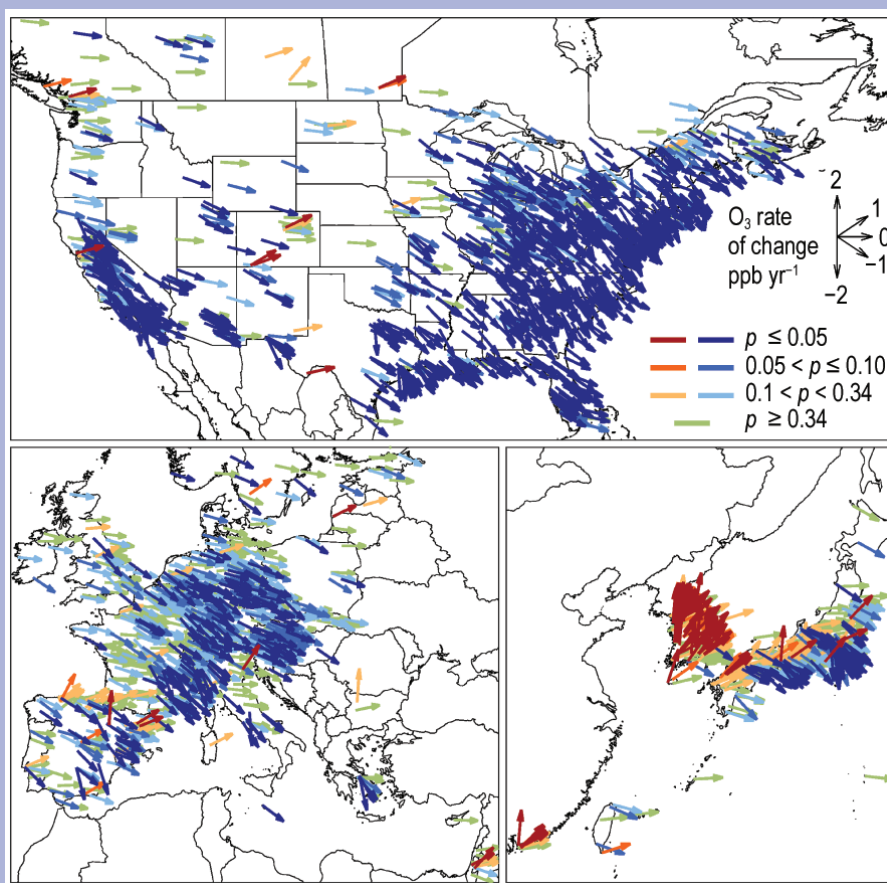


**FIG. SB2.4.** Trends of the O<sub>3</sub> 98th percentile at the sites shown in Fig.SB 2.3, during 2000–14. Vector colors indicate the *p*-values on the linear trend for each site: blues indicate negative trends, oranges indicate positive trends, and green indicates weak or no trend; lower *p*-values have greater color saturation.

ozone at MLO has increased significantly at the rate of  $0.15 \pm 0.05 \text{ nmol mol}^{-1} \text{ yr}^{-1}$ , resulting in an overall increase of  $6.5 \text{ nmol mol}^{-1}$  since 1973, or 17%. MLO experiences high interannual ozone variability due to its location in the transition region between tropical and extratropical air masses. The ozone trend in the dry air masses, which tend to originate at higher altitudes and latitudes to the west and northwest of MLO, while moist air masses tend to come from the east at lower latitudes and altitudes (Harris and Kahl 1990; Oltmans et al. 2006; M. Lin et al. 2014). Ozone observations at MLO were divided into dry (<40th percentile) and moist (>60th percentile) air masses using observed dew point temperatures and a long-term climatology. The trend in the dry air masses is 50% greater compared to the trend using all air masses (9.9 ppbv total increase since 1974, or 23%), which implies

that the site is influenced by ozone increases in up-wind regions to the west and northwest, most likely Asia where limited in situ observations have shown general ozone increases over the past two decades at the surface (Cooper et al. 2014; Ma et al. 2016; Sun et al. 2016; Xu et al. 2016; T. Wang et al. 2017) and in the free troposphere (Zhang et al. 2016).

#### 7) CARBON MONOXIDE—J. Flemming and A. Inness

Carbon monoxide (CO) plays a significant role as a chemical precursor in determining the abundance of climate forcing gases like methane (CH<sub>4</sub>), through hydroxyl radical (OH) chemistry and tropospheric ozone (Hartmann et al. 2013). CO is therefore regarded as an indirect climate forcing agent. Sources of CO include incomplete fossil fuel and biomass combustion and in situ production via the oxidation



of CH<sub>4</sub> and other organic trace gases. Combustion and chemical in situ sources typically produce similar amounts of CO each year.

The Copernicus Atmosphere Monitoring Service (CAMS) produced a retrospective analysis of CO, aerosols, and ozone for the period 2003–15 by assimilating satellite retrievals of atmospheric composition with the ECMWF model (Flemming et al. 2017). This dataset has been extended to the end of 2017 and is used here. Version 5 total column retrievals of CO from the MOPITT instrument (Deeter et al. 2013) were assimilated from January 2003 until the end of February 2017. From March 2017 onwards MOPITT version 7 data were used because the older version was discontinued. The anthropogenic emissions were taken from the MACCity inventory (Granier et al. 2011) that accounts for projected emission trends according to the representative concentration pathways (RCP) 8.5 scenario (Riahi et al. 2011). Biomass burning emissions were taken from the Global Fire Assimilation System (v1.2, Kaiser et al. 2012, also Section 2h3).

The global tropospheric CO concentrations have decreased by about 1% yr<sup>-1</sup> in the last decade according to studies based on MOPITT and other observations (Worden et al. 2013; Yin et al. 2015; Flemming et al. 2017; Gaubert et al. 2017). Model simulations (Flemming et al. 2017; Gaubert et al. 2017) result in weaker negative trends than the observation based estimates. This could point to an underestimation of anthropogenic emissions trends or to unaccounted chemical feedback in the CO-OH-O<sub>3</sub>-CH<sub>4</sub> system of the models (Gaubert et al. 2017).

The time series of the global CO burden obtained from the CAMS interim reanalysis (Fig. 2.61) shows an average reduction from 410 Tg in 2003 to 358 Tg in 2017. This is equivalent to a linear trend of -3.3 Tg yr<sup>-1</sup> (-0.8% yr<sup>-1</sup>) over the whole period. However, the global burden decreased more rapidly during 2008

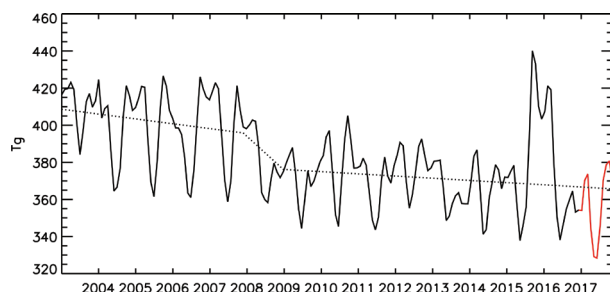


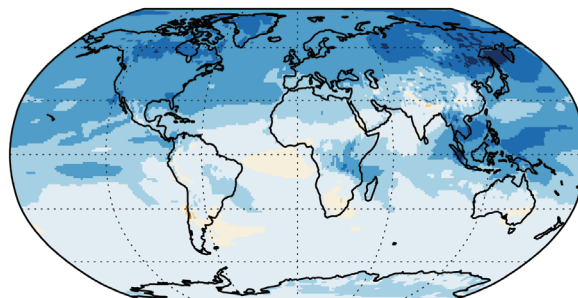
**FIG. 2.61.** Time series (black solid line for 2003–16, red for 2017) of monthly global CO burdens (Tg) from the CAMS interim reanalysis and a piecewise linear trend (dotted line) for the periods 2003–07, 2008, and 2009–17.

than in the periods before and after this year, and further investigation is necessary to determine the cause. The large increase in the global CO burden in the second half of 2015 and the first half of 2016 was caused by intensive biomass burning in Indonesia in October 2015 (Huijnen et al. 2016). A piecewise calculation of linear trends for the periods 2003–07, 2008, and 2009–17 revealed trends of -3.0 Tg yr<sup>-1</sup> (-0.7% yr<sup>-1</sup>), -20.0 Tg yr<sup>-1</sup> (-5.0% yr<sup>-1</sup>), and -1.1 Tg yr<sup>-1</sup> (-0.3% yr<sup>-1</sup>), respectively. This means that a much stronger reduction of the global CO burden occurred in 2008 and in the period 2003–07 than after 2009.

2017 was the year with the lowest CO burden in the CAMS interim reanalysis. The annual mean of 2017 was below the median of the annual means for the 2003–17 period almost everywhere, mostly in the range from 0 to -10% (Fig. 2.62). This indicates that no regional biomass burning event in 2017 had a global impact on annual regional burdens.

In general the relative decrease was more pronounced in the mid- and high latitudes of the Northern Hemisphere than in the Southern Hemisphere. The largest annual minima occurred over Indonesia, where the annual CO burden was up to 20% lower than the median values after the extreme fires of

(a) Jan–Jun 2017



(b) Jul–Dec 2017

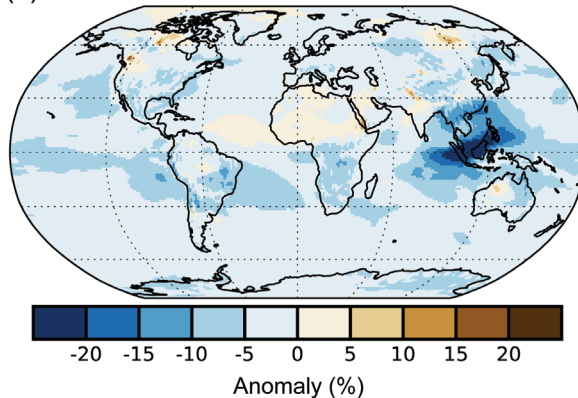


**FIG. 2.62.** Total column CO anomalies (%) for (a) Jan–Jun 2017 and (b) Jul–Dec 2017 with respect to 2003–17 median from the CAMS interim reanalysis.

2015. Also, fire activity in Central Africa was overall lower than in previous years. The lower CO in the first half of 2017 (Fig. 2.62a) was the primary reason for the negative annual anomalies. Intensive fires in Chile in January had only a localized effect on the CO burden in the first quarter of 2017.

The more active fires occurred predominantly in the second half of 2017 (Fig. 2.62b; Section 2h3). Large boreal fires in Canada (British Columbia, The Northwest Territories) and Central Siberia increased the CO burden in the high northern latitudes in the third quarter of 2017 by over 10% and locally up to 20% with respect to the decadal median (not shown). In September and the final quarter of 2017, increased activity during the fire seasons in Brazil and in eastern and central Africa caused the CO burden to rise up to 10% over the long-term seasonal mean in the affected regions and in the adjacent outflow regions over the central Atlantic.

#### *h. Land surface properties*

##### **1) LAND SURFACE ALBEDO DYNAMICS—B. Pinty and N. Gobron**

The land surface albedo represents the fraction of solar radiation scattered backward by land surfaces. In the presence of vegetation, surface albedo results from complex nonlinear radiation transfer processes determining the amount of radiation that is scattered by the vegetation and its background, transmitted through the vegetation layer, or absorbed by the vegetation layer and its background (Pinty 2012).

The geographical distributions of normalized anomalies in visible and near-infrared surface albedo for 2017 calculated for a 2003–17 base period [for which two MODIS sensors are available (Schaaf et al. 2002)] are shown in Plate 2.1ac, ad, respectively. Note that MODIS collection 6 albedo products are used here. Mid- and high latitude regions of the Northern Hemisphere are characterized by both positive (blue) and negative (brown) anomalies mainly as a consequence of interannual variations in snow cover (see Section 2c1), amount, and duration in winter and spring seasons.

The positive anomalies especially in the visible range over the U.S. Northwest and High Plains, southwest and eastern Canada, Scandinavia, and northern Russia are probably associated with above-average snow cover and extent in spring with the occurrence of snow storms in some of these regions. Below-average snow cover extent across most of Europe, Turkey, Iran, southern Russia, and in parts of the U.S. Northern Plains and Rockies extending into the southern Canadian Prairies may be responsible

for the negative anomalies reaching (or locally exceeding) –30 % in the visible and about –10 % in the near-infrared domain. The fast decline of the snow cover extent and duration as early as February (Section 2c2) may be due to unusually warm and relatively dry conditions over western Europe from early spring to June (<https://climate.copernicus.eu/resources/data-analysis/average-surface-air-temperature-analysis/monthly-maps/>)

A few snow-free regions show positive anomalies, especially in the visible domain, in northeast Brazil, from southeast Somalia and Kenya to northern Tanzania, Anatolia, and Nigeria, and in some localized spots around the Caspian Sea. These are generally associated with less favorable vegetation growing conditions compared to previous years (Section 2h2), although contamination of the albedo retrievals by clouds and aerosol load (especially in intertropical regions) may also induce some artifacts. Many snow-free regions exhibit noticeable and spatially consistent negative anomalies, in particular in the visible domain, and especially pronounced (up to 30%) across eastern China, Southeast Asia, parts of India, much of southern and central Africa, parts of Australia, and much of Argentina. Consistent warmer-than-usual conditions persisted over most of these regions, sometimes associated with below-normal precipitation. A significant fraction of these variations is attributable to vegetation dynamics (Pinty et al. 2011a,b) over these regions where vegetation is sensitive to stress from ambient conditions and, in particular, water availability. Although weaker in the near-infrared domain, these negative anomalies are, in some instances, spectrally correlated, for example, over India and northeast Brazil. The amplitude of these positive and negative anomalies often changes with seasons. The situation is thus globally analogous to 2016, with above-average temperatures and a few extreme precipitation and drought events (e.g., across southern Europe) occurring across the world.

Analysis of the zonally averaged albedo anomalies in the visible (Fig. 2.63a) and near-infrared (Fig. 2.63b) broadband spectral domains indicates large interannual variations related to the occurrence of snow events in winter and spring at mid- and high northern latitudes as well as to vegetation conditions during the spring and summer periods. Negative anomalies are noticeable between 20° and 45°S in 2017, featuring a deviation from average conditions mainly over Latin America, southern Africa, and Australia. Consistent negative anomalies in the visible domain are discernible across midlatitude regions in the Northern Hemisphere in 2017.

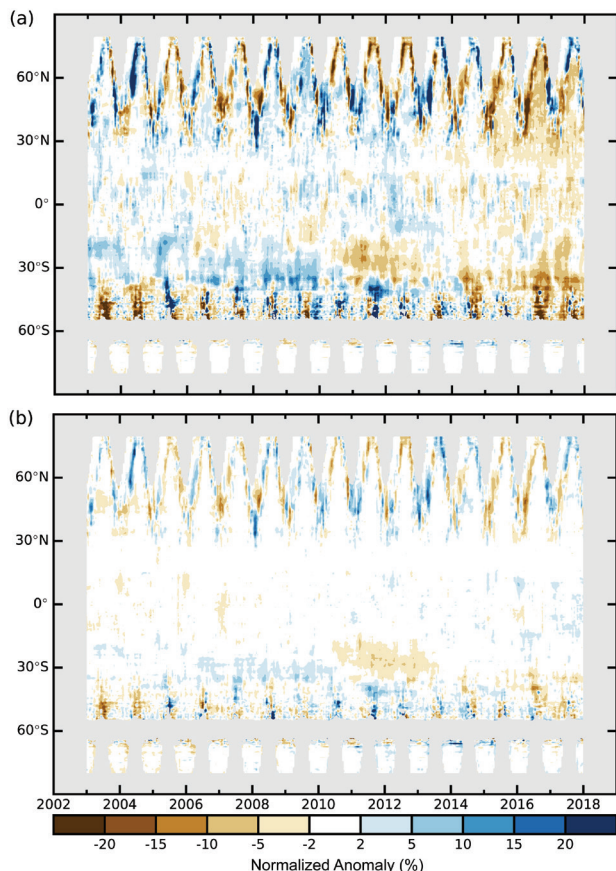


**FIG. 2.63. Zonally averaged albedo anomalies (%; 2003–17 base period) in the (a) visible and (b) near-infrared broadband.**

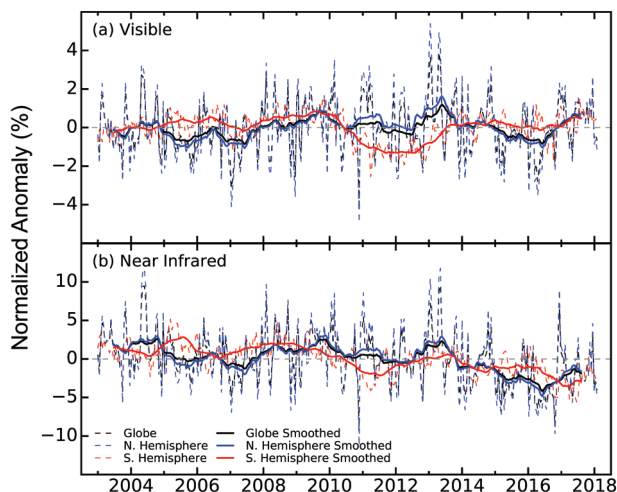


**FIG. 2.64. Global albedo anomalies (%; 2003–17 base period) in the (a) visible and (b) near-infrared broadband.**

The amplitude of the globally and hemispherically averaged normalized anomalies resulting from a 12-month running mean (Fig. 2.64) is within  $\pm 5\%$  (3%) in the visible (near-infrared) domain. The anomalies are not estimated over Antarctica owing

to missing data. The year 2017 is characterized by a trend of the negative anomalies toward average conditions in the visible domain that is driven by the dominant contributions from the Northern Hemisphere regions. These figures also indicate spectrally correlated multiannual variations during 2003–17 with positively biased values in the visible at the beginning of this period.

## 2) TERRESTRIAL VEGETATION ACTIVITY—N. Gobron

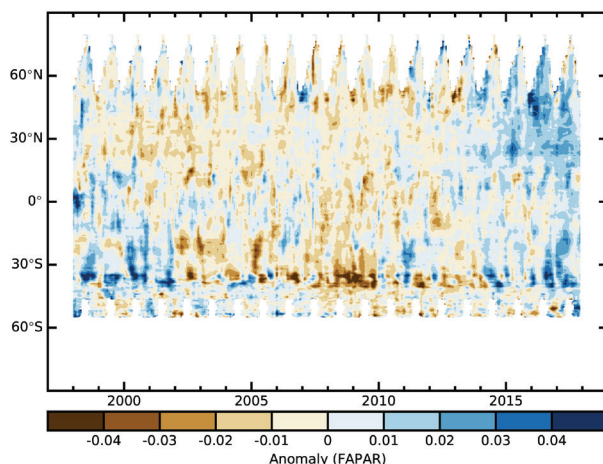
Terrestrial photosynthesis activity is inferred from space on the basis of one land essential climate variable (ECV) as defined by GCOS (2016): the fraction of absorbed photosynthetically active radiation (FAPAR). The 2017 analysis has merged 20 years of global FAPAR products retrieved from three passive optical sensors at medium spatial scale from 1998 to 2017 (Gobron et. al. 2010; Pinty et al. 2011a,b; Gobron and Robustelli 2013). Note that Collection 6 MODIS albedo (Section 2h1) was used in this year's report.

Plate 2.1ae displays the annual FAPAR anomalies at global scale for which brown (blue) color indicates negative (positive) values. Large geographical variations in vegetated surface conditions were present at the global scale. Negative and positive anomalies indicate less and more photosynthetic activities in green live vegetation.

The most negative anomaly events (not favorable for vegetation) took place over eastern Brazil, Somalia, and Kenya followed by the weakest negative ones in the western part of Russia. The major positive events occurred in the eastern part of China and Botswana and the weakest appeared over Coahuila (northern state of Mexico), India, and the Rio Negro region in Argentina.

The strong negative FAPAR anomalies over eastern Brazil were mainly due to severe droughts occurring at the start of the year that impacted the annual results. Over Somalia the persistent precipitation deficit extended both the geographical area and its negative level in terrestrial activities, meaning that vegetation photosynthesis declined rapidly at the beginning of the year. The vegetation activities in northwestern Russia declined during spring, possibly due to heavy snow events. Terrestrial photosynthesis activities continued to proliferate over the eastern part of China as stronger positive FAPAR anomaly events were observed as both higher temperatures and heavy precipitation were favorable to vegetation growth in 2017. FAPAR anomalies were also positive in 2017 over Botswana as in 2014, meaning that after droughts in 2015–16, sufficient precipitation helped vegetation recover.





**FIG. 2.65. Zonally averaged FAPAR anomalies from 1998–2017.**

Positive anomalies occurred also over smaller regions such as over Coahuila (Mexico) and the Rio Negro region in Argentina; these have occurred each year since 2015 and may correspond to high spring temperatures. Australia was found to have positive FAPAR anomalies over several local regions.

Figure 2.65 displays the longitudinal average anomalies from 1998 to 2017. Strong seasonal interhemispheric variations are depicted with mainly positive anomalies after 2014 over 20°N and negative anomalies from 2002–10 in the south latitudes.

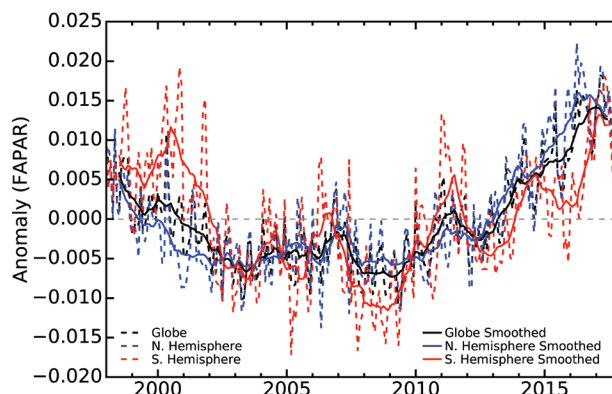


**FIG. 2.66. Global, NH, and SH FAPAR anomalies from 1998–2017, plotted in black, blue, and red, respectively. Dotted lines denote each monthly period; solid lines indicate the 6-mo running averaged mean. (Sources: SeaWiFS, MERIS, and MODIS sensors.)**

Spring 2017 revealed negative anomalies at higher latitudes (~ 60°N), as was the case in summer around 20°N and 20°S. Around 30°S recurrent and strong positive anomalies have occurred since 2014, contradicting the strong negative anomalies from 2005–10.

As shown in Fig. 2.66, there was a strong reversal between anomalies over the Northern and Southern Hemispheres during the past 20 years. The FAPAR anomaly over the Southern Hemisphere in 2017 returned to a positive level (last evident in 2000) while it has continued to increase over the Northern Hemisphere since the 2008–10 minimum.

## SIDEBAR 2.3: PHENOLOGY OF TERRESTRIAL AND FRESHWATER PRIMARY PRODUCERS—D. L. HEMMING, R. ABERNETHY, C. ARMITAGE, K. BOLMGREN, R. MYNENI, T. PARK, A. D. RICHARDSON, T. RUTISHÄUSER, T. H. SPARKS, AND S. J. THACKERAY.

Phenology is the study of recurring events in nature and their relationships with climate. The word derives from the Greek *phainō* “appear” and *logos* “reason”, emphasizing the focus on observing events and understanding why they occur (Demarée and Rutishauser 2009). Phenological recording has a history that dates back many centuries (Linnaeus 1753; Aono and Kazui 2008). More recently, advances in monitoring technologies have enabled automated and remotely sensed observations, complemented by increasing citizen science participation in monitoring efforts. Phenological information can also be derived from widespread environmental monitoring stations around the globe.

Phenological records clearly demonstrate the biological effects of year-to-year variability in climate, as well as longer-term trends associated with environmental change.

Shifts in the growing season, for example, are more tangible and more readily conveyed to the general public than seemingly small increases in mean annual temperature. Phenological monitoring thus plays an important role in understanding how our planet is changing.

Here, we describe just a fraction of the phenological information currently available, highlighting northern hemisphere records of phenology of primary producers across a range of spatial and temporal scales.

### Ground-based observations

**Long-term phenology monitoring network, Germany:** Deutscher Wetterdienst (DWD) maintains a dense national phenological observation network and database ([www.dwd.de/phaenologie/](http://www.dwd.de/phaenologie/)). Plant phenological

CONT. SIDEBAR 2.3: **PHENOLOGY OF TERRESTRIAL AND FRESHWATER PRIMARY PRODUCERS**—D. L. HEMMING, R. ABERNETHY, C. ARMITAGE, K. BOLMGREN, R. MYNENI, T. PARK, A. D. RICHARDSON, T. RUTISHÄUSER, T. H. SPARKS, AND S. J. THACKERAY.

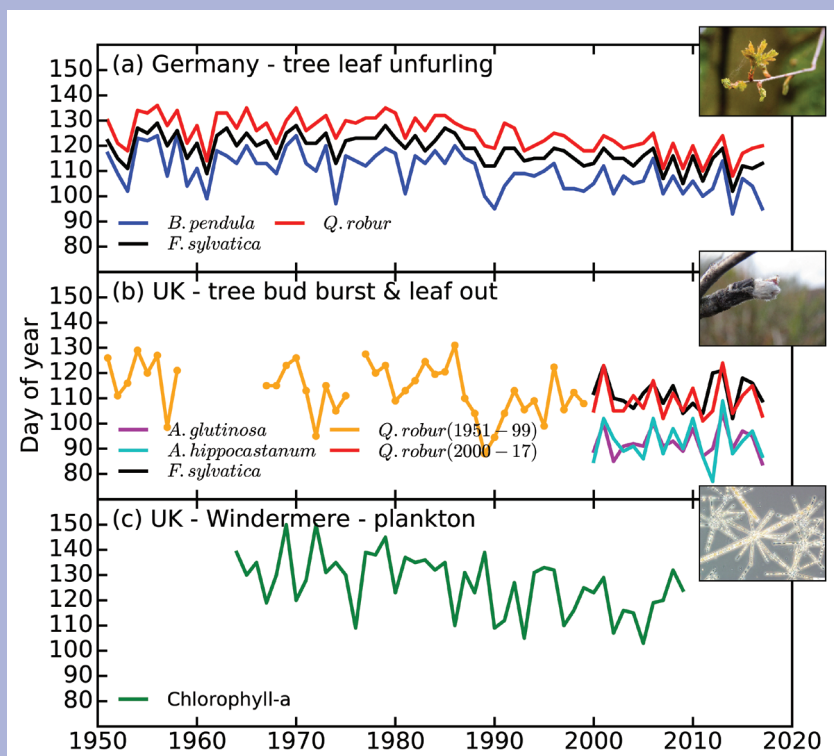


**FIG.SB2.5.** Time series of phenological changes in primary producers from records in Germany and UK, showing timing (by ordinal date) of (a) leaf unfolding of tree species in Germany from DWD national network: Pedunculate oak – *Quercus robur* L., (b) budburst of 4 common tree species in U.K. from Nature’s Calendar: Alder – *Alnus glutinosa* L. Gaertn; horse chestnut – *Aesculus hippocastanum* L.; pedunculate oak; and beech – *Fagus sylvatica* L., and (c) long-term phenological changes in spring phytoplankton growth, indicated by the seasonal timing of maximum spring chlorophyll-*a* concentrations. Original chlorophyll data collected from the north basin of Windermere by the Centre for Ecology & Hydrology and the Freshwater Biological Association, U.K.

records dating to 1951, some available since 1925, are openly accessible via the online archive (Kaspar et al. 2014). Currently, about 1100 observers contribute to the database, recording phenological events in cover crops, wild plants, and fruit trees. The data have many applications, including advice on current growing season for agricultural activities, pollen forecasts, and environmental change research. Figure SB2.5a highlights the record of leaf unfolding of pedunculate oak (*Quercus robur* L.), which has advanced by about 10 days over the last 50 years. This species is referred to as an “indicator species”, and, due to its strong dependence on spring temperature, leaf unfolding is used to mark the beginning of “full spring”.

**Nature’s Calendar, UK:** Nature’s Calendar is a coordinated national “citizen science” network of phe-

nological observations, supported by the Woodland Trust ([www.woodlandtrust.org.uk/visiting-woods/natures-calendar/](http://www.woodlandtrust.org.uk/visiting-woods/natures-calendar/)). Currently, over 4000 members of the public contribute regular observations, and the database includes over 2.7 million records, dating from 1695. Early observations of “Indicators of Spring” were made from 1736 to 1797 by Robert Marsham in Norfolk and continued by his descendants until 1958 (Sparks and Lines 2008). In 1875, a national network was launched by the (Royal) Meteorological Society, which ran until 1948, recording flowering, appearance of bird and insect species, and publishing unusual events and their climate relationships (Clark 1936). In 1998, the Centre for Ecology and Hydrology resurrected this network, and in 2000, was joined by the Woodland Trust to promote phenology to a wider audience (Sparks et al. 1998; Sparks and Smithers 2002). Figure SB2.3b highlights the timing of budburst for four tree species in this record. As with other plant species, budburst is significantly related to spring average temperature (Online Fig. S2.21), with a 1°C rise in March or

April temperature associated with earlier budburst of 3.5 to 4.8 days, depending on species and region (Abernethy et al. 2017).

**Windermere, UK:** Seasonal activity of primary producers is monitored in marine and freshwater environments. For example, at Windermere—England’s largest lake—fortnightly measurements of chlorophyll-*a* concentrations, a proxy for primary producer biomass, have been recorded since the 1960s. These data show a long-term shift toward earlier spring algal blooms (Fig. 2.3c), which is correlated with both increasing spring water temperatures and changes in nutrient availability (Thackeray et al. 2013). Hence, large-scale climatic drivers act alongside more localized lake-specific influences to bring about phenological changes in this system.

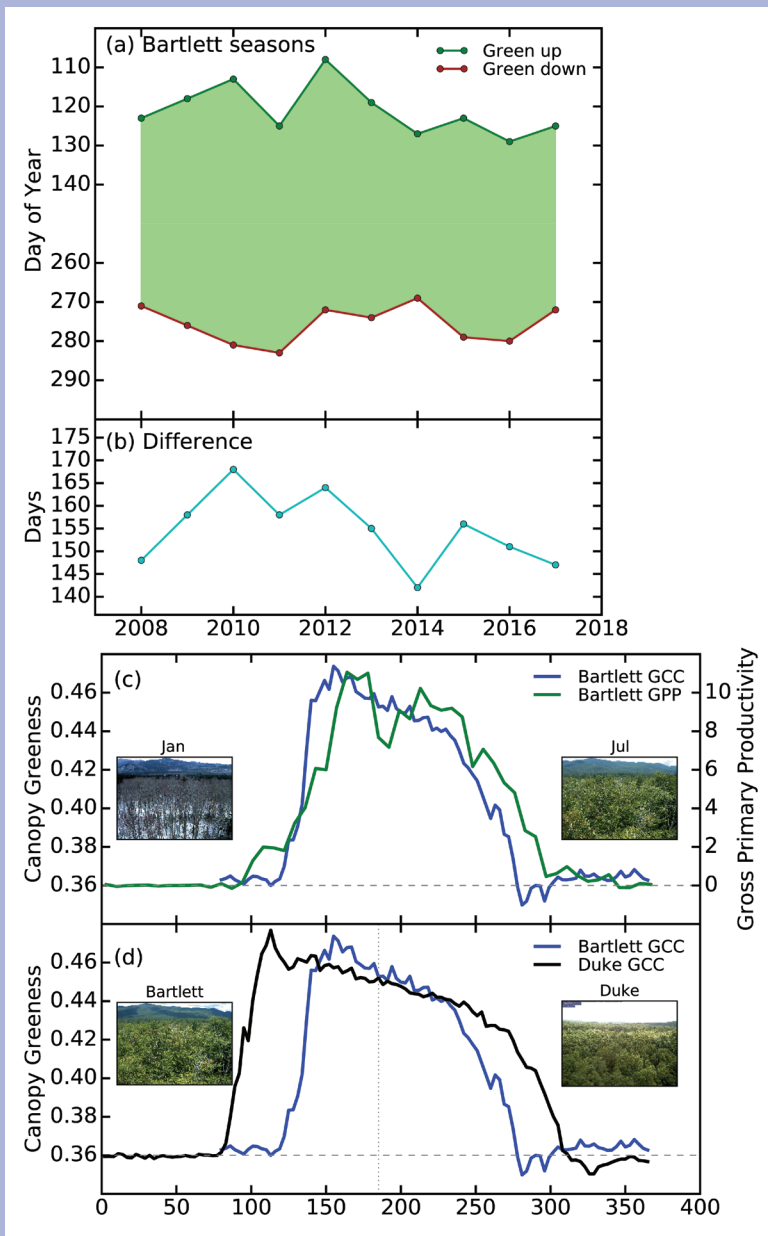


**FIG. SB2.6.** Phenocam records of canopy greenness (green chromatic coordinate, GCC) and GPP from two deciduous forest sites in the U.S.: Bartlett Experimental Forest, NH, and Duke Forest, NC, showing: (a) Time series of day of year of “Greenup”, “Greendown” and (b) number of days of “Green canopy duration” at Bartlett, (c) comparison of seasonality of GCC and GPP (estimated from flux measurements) at Bartlett during 2017, and (d) seasonality in GCC between Bartlett (mean annual temperature = 6.6°C) and a warmer site, Duke (mean annual temperature = 15°C) during 2017. Photos show both sites in Jul 2017.

## Pan European Phenology (PEP)

**project:** The PEP project promotes and facilitates phenological research, education and environmental monitoring across Europe. It maintains the Pan European Phenology (PEP) database ([www.pep725.eu](http://www.pep725.eu)), which provides unrestricted data access for science and education. This currently includes 12 million records, with contributions since 1868 from 32 European partners for 46 growing stages and 265 plant species and cultivars (Templ et al. 2018).

## Remote sensing

Remote sensing provides some of the clearest records of regional, hemispheric, and global phenological changes by linking radiance measurements to photosynthetic indicators of terrestrial and marine primary producers (Park et al. 2016; Sapiano et al. 2012).

**Near-surface remote sensing:** Digital camera networks observe “the rhythm of the seasons”, from the tropics to the tundra. PhenoCam (<http://phenocam.sr.unh.edu>) is a collaborative network of over 400 cameras, most at research sites in the United States. Measures of canopy greenness (Richardson et al. 2018a) derived from camera imagery can be used to track vegetation activity and identify the start and end of season. At one temperate deciduous forest (Richardson et al. 2007), the 2017 growing season was markedly shorter than the decadal average because of late onset and early senescence (Fig. SB2.6a). At the same site, the seasonal cycle of canopy greenness follows that of gross primary productivity (GPP) estimated from eddy covariance measurements of CO<sub>2</sub> fluxes, confirming the role of phenology in regulating ecosystem carbon fixation (Richardson et al. 2010; Fig. SB2.6c). The difference between this cooler forest and a warmer forest (Fig. SB2.6d) illustrates the role of climate in controlling phenology. These data can therefore help improve understanding of relationships between phenology, ecosystem processes, and environmental driv-



CONT. SIDEBAR 2.3: **PHENOLOGY OF TERRESTRIAL AND FRESHWATER PRIMARY PRODUCERS**—D. L. HEMMING, R. ABERNETHY, C. ARMITAGE, K. BOLMGREN, R. MYNENI, T. PARK, A. D. RICHARDSON, T. RUTISHÄUSER, T. H. SPARKS, AND S. J. THACKERAY.

ers. Furthermore, phenocam data are valuable for ground truthing satellite observations, as they are continuous in time and require minimal correction or screening for atmospheric effects Richardson et al. 2018b).

**Satellite remote sensing:** Satellite-derived phenology indices provide useful regional to global-scale monitoring for phenology studies (Zhang et al. 2003). Figure SB2.7 highlights Northern Hemisphere land surface phenology indices during 2000–17, derived from radiance observations from the MODIS sensor. It shows a widespread and continued earlier start-of-season (−1.5 days) and later end-of-season (+1.3 days) over this period (Park et al. 2016). In 2017, the start-of-season reveals a dramatic spatial contrast between North America and Eurasia. Northeastern Europe and western Russia showed a striking

delay (+6.0 days) associated with an anomalous spring cold spell (−2.4°C), whereas North America showed a widespread earlier start-of-season (−5.1 days), due to warmer than average spring temperatures (+0.5°C). The end-of-season across Eurasia was generally later than average (+2.3 days), but earlier (−3.6 days) over southern European temperate zones.

Many phenological events provide clear indicators of the influence of climate on our environment and natural resources. Current observations apply diverse techniques

to monitor phenological changes across wide spatial scales—from global biomes to microscopic organisms. Furthermore, phenology records exist that span multiple decades, even centuries, and these provide valuable archives of long-term environmental change. There is now a fundamental need for integrated analyses of multiple phenology and climate observations to help understand, and prepare for, the future impacts of climate variability and change on environmental systems, and routine monitoring to capture important changes as they occur.

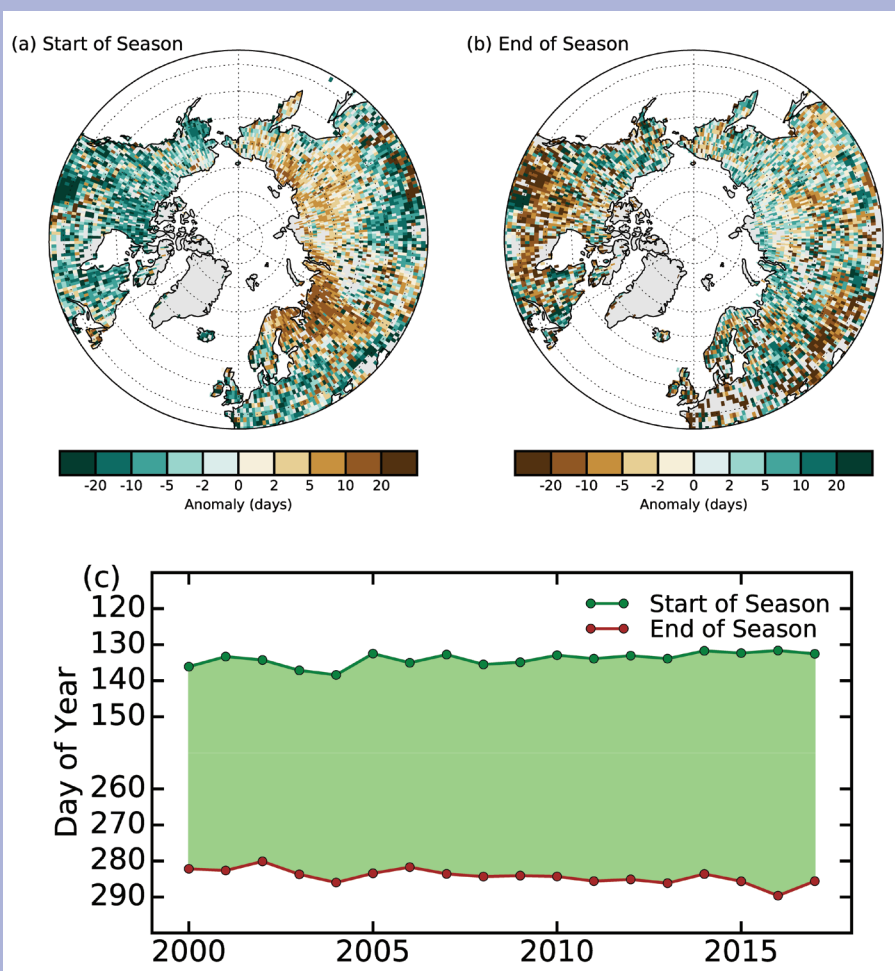


**FIG. SB2.7. MODIS-derived NH (>45°N) land surface phenology, showing 2017 anomaly (days), relative to 2000–17 average, for (a) start-of-season, (b) end-of-season, and (c) hemispheric average day of year of the start and end of season for 2000–17.**

### 3) BIOMASS BURNING—J. W. Kaiser and G. R. van der Werf

The first vegetation fires, a.k.a. biomass burning, occurred shortly after the first land plants evolved. They have since become an integral part of many natural and cultivated ecosystems and are largely modulated by climate. Conversely, fires are a major source of climate-forcing atmospheric aerosols and trace gases. Today, human activity also exerts a strong influence on fire occurrence through land cover change by providing a large number of ignitions and by active fire suppression. Fires have substantial interannual variability, which mostly originates from the boreal region and the tropical deforestation zone. The extent of vegetation fires is traditionally quantified in terms of burned area, which is around 500 million hectares worldwide each year (Giglio et al. 2013; Randerson et al. 2012).

Burned area and the thermal radiation released by active fires have been quantified on a global scale with satellites since the late 1990s. The Global Fire Emissions Database (GFED) estimates emissions since 1997 based on burned area and fuel consumption (van der Werf et al. 2017). Satellite-observed fire radiative power is used by the Global Fire Assimilation System (GFAS) to estimate emissions since 2003 and in near-real time (Kaiser et al. 2012). GFAS is calibrated to partly match GFED. Here, an updated GFAS version (Kaiser et al. 2017) is used; it resolves the subdaily variability and uses MODIS Collection 6 products (Giglio et al. 2016) for the entire time period. The absolute values have been homogenized with earlier GFAS and GFED versions by removing a global average bias of  $-14\%$ . The combined use of GFAS (2003–17) and GFED (1997–2016) indicates that fire emissions were around  $2 \text{ Pg C yr}^{-1}$  (Fig. 2.67).

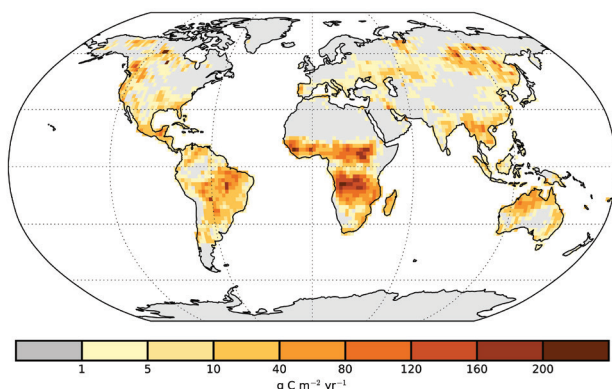


**FIG. 2.67. Global map of fire activity in 2017 in terms of carbon consumption ( $\text{g C m}^{-2} \text{ yr}^{-1}$ ). (GFASv1.4)**

In 2017, low fire activity led to the lowest global pyrogenic emissions since at least 2003 and probably since the start of GFED in 1997. Emissions were 15% below the 2003–16 average (Table 2.7; Plate 2.1af). The year with lowest emissions prior to 2017 was 2013; those two years were relatively close in magnitude, especially when considering the substantial uncertainty associated with these estimates. The negative regional anomalies were particularly pronounced in tropical Asia, where high rainfall rates, among other things, led to emissions that were only about 5% of those reached during the El Niño episode in 2015. Strong negative anomalies also occurred in Indochina and in southern Siberia.

Stronger-than-usual fire activity occurred in North America and Europe, with anomalies of  $+36\%$  and  $+22\%$ , respectively. The time series for North America (Fig. 2.68) shows that four out of the last five fire seasons were exceptionally intense. European fire emissions were dominated by an unusually long burning season in Portugal and in Galicia in northwestern Spain.

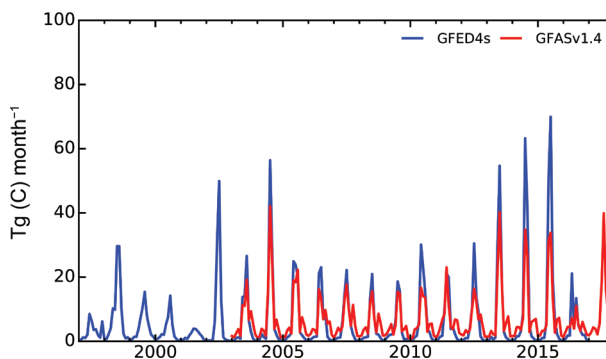


**FIG. 2.68. Time series of fire activity during 1997–2017 in terms of carbon consumption ( $\text{Tg C month}^{-1}$ ) for North America.**

Table 2.7. Annual continental-scale biomass burning budgets in terms of carbon emission (Tg C yr <sup>-1</sup> ) from GFASv1.4.				
		2003–16	2017	
Quantity in Tg C yr <sup>-1</sup>		Mean Value (Range)	Value	Anomaly (%)
Global		1973 (1690–2272)	1683	–290 (–15%)
North America	30°–75°N 170°–30°W	84 (56–112)	113	+30 (+36%)
Central America	0°–30°N 170°–30°W	85 (65–122)	72	–12 (–14%)
SH America	0°–60°S 170°–30°W	320 (190–473)	285	–35 (–11%)
Europe and Mediterranean	30°–75°N 30°W–60°E	33 (19–62)	41	+7 (+22%)
NH Africa	0°–30°N 30°W–60°E	404 (353–453)	357	–47 (–12%)
SH Africa	0°–35°S 30°W–60°E	485 (444–528)	457	–28 (–6%)
Northern Asia	30°–75°N 60°E–170°W	186 (99–418)	139	–48 (–26%)
Southeast Asia	10°–30°N 60°E–190°E	122 (101–150)	81	–41 (–34%)
Tropical Asia	10°N–10°S 60°–170°E	143 (38–425)	23	–120 (–84%)
Australia	10°–50°S 60°E–170°W	112 (47–219)	115	+3 (+3%)